# Semitauonic $b$-hadron decays: A lepton flavor universality laboratory

Florian U. Bernlochner[*]

*Physikalisches Institut der Rheinischen Friedrich-Wilhelms-Universität Bonn, 53115 Bonn, Germany*

Manuel Franco Sevilla[†]

*University of Maryland, College Park, Maryland 20742, USA*

Dean J. Robinson[‡]

*Ernest Orlando Lawrence Berkeley National Laboratory, University of California, Berkeley, California 94720, USA*

Guy Wormser[§]

*Laboratoire Irène Joliot-Curie, Université Paris–Saclay, CNRS/IN2P3, Orsay 91405, France*

(published 4 February 2022)

The study of lepton flavor universality violation (LFUV) in semitauonic $b$-hadron decays has become increasingly important in light of long-standing anomalies in their measured branching fractions, and the large datasets anticipated from the LHC experiments and Belle II. In this review, a comprehensive survey of the experimental environments and methodologies for semitauonic LFUV measurements at the $B$ factories and LHCb is undertaken, along with an overview of the theoretical foundations and predictions for a wide range of semileptonic decay observables. The future prospects of controlling systematic uncertainties down to the percent level, matching the precision of standard model (SM) predictions, are examined. Furthermore, new perspectives and caveats on combinations of the LFUV data are discussed and the world averages for the $\mathcal{R}(D^{(*)})$ ratios are revisited. Here it is demonstrated that different treatments for the correlations of uncertainties from $D^{**}$ excited states can vary the current $3\sigma$ tension with the SM within a $1\sigma$ range. Prior experimental overestimates of $D^{**}\tau\nu$ contributions may further exacerbate this. The precision of future measurements is also estimated; their power to exploit full differential information, and solutions to the inherent difficulties in self-consistent new physics interpretations of LFUV observables, are explored.

DOI: 10.1103/RevModPhys.94.015003

## CONTENTS



[*]florian.bernlochner@uni-bonn.de
[†]manuelf@umd.edu
[‡]drobinson@lbl.gov
[§]wormser@lal.in2p3.fr

 

## I. INTRODUCTION

Over the past decade, collider experiments have provided ever-more precise measurements of standard model (SM) parameters, while direct collider searches for new interactions or particles have yielded ever-more stringent bounds on new physics (NP) beyond the SM. This in turn has brought renewed attention to the NP discovery potential of indirect searches: measurements that compare the interactions of different species of elementary SM particles to SM expectations.

A key feature of the standard model is the universality of the electroweak gauge coupling to the three known fermion generations or families. In the lepton sector, this universality results in an accidental lepton flavor symmetry that is broken in the SM (without neutrino mass terms) only by Higgs Yukawa interactions responsible for generating the charged lepton masses. A key prediction, then, of the standard model is that physical processes involving charged leptons should feature a *lepton flavor universality*: an approximate lepton flavor symmetry among physical observables, such as decay rates or scattering cross sections, that is broken in the SM only by charged lepton mass terms in the amplitude and phase space. (Effects of additional Dirac or Majorana neutrino mass terms in extensions of the SM are negligible in all contexts that we consider.) In the common parlance of the literature, testing for lepton flavor universality violation (LFUV) in any particular process thus refers to measuring deviations in the size of lepton flavor symmetry breaking versus SM predictions.

An observation of LFUV would clearly establish the presence of physics beyond the standard model, and could thus provide an indirect window into resolutions of the nature of dark matter, the origins of the matter-antimatter asymmetry, or the dynamics of the electroweak scale itself. Decades of LFUV measurements have yielded results predominantly in agreement with SM predictions. Various strong constraints have been obtained from (semi)leptonic decays of light hadrons, gauge bosons, or leptonic $\tau$ decays [see Zyla *et al.* (2020)], among many other measurements. A notable recent addition is the measurement of $\mathcal{B}(W \to \tau\nu)/(W \to \mu\nu)$ (Aad *et al.*, 2020), which resolved a long-standing LFUV anomaly from LEP that deviated from the SM prediction at $2.7\sigma$. Moreover, sources of LFUV that implicate NP interactions with the first two quark generations are typically strongly constrained by, e.g., precision $K$-$\bar{K}$ and $D$-$\bar{D}$ mixing measurements. Such LFUV bounds involving third generation quarks, however, are typically much weaker (Cerri *et al.*, 2019).

This review focuses on the rich experimental landscape for testing LFUV in semileptonic *b*-hadron decays. Not only do these decays provide a high statistics laboratory to measure LFUV that is relatively theoretically clean, but results from the last decade of measurements have indicated anomalously high rates for various semitauonic $b \to c\tau\nu$ decays compared to precision SM predictions. In particular, the ratios

$$\mathcal{R}(D^{(*)}) = \frac{\mathcal{B}(B \to D^{(*)}\tau\nu)}{\mathcal{B}(B \to D^{(*)}\ell\nu)}, \qquad \ell = e, \mu, \tag{1}$$

where $D^{(*)}$ refers to both $D$ and $D^*$ mesons, deviate from SM predictions at the $3\sigma$ level when taken together (Amhis *et al.*, 2019). (We later revisit the construction of these world averages and their degree of tension with the SM.) Apart from these results, there are additional measurements for various other $b \to c\tau\nu$ decays and other observables, including $\mathcal{R}(J/\psi)$, the $\tau$ polarization, and $D^*$ longitudinal fractions; see Sec. IV. Some of these measurements presently agree with SM predictions only at the $1.6\sigma - 1.8\sigma$ level, and when combined with $\mathcal{R}(D^{(*)})$ can mildly increase the degree of tension with the SM. Some tensions also currently exist in several $b \to see$ vs $b \to s\mu\mu$ transitions, each at the $2.5\sigma$ level (Aaij *et al.*, 2017c, 2019c). See Ciezarek *et al.* (2017) and Bifani *et al.* (2019) for prior experimental reviews that consider aspects of LFUV in semileptonic decays.

Upcoming runs of the LHC, the High-Luminosity (HL) LHC, and Belle II will yield large new datasets for a wide range of $b \to c\tau\nu$ and $b \to u\tau\nu$ processes. Given this expected deluge of data, it is important to review and synthesize our understanding of the various strategies and channels through which LFUV might be discovered. To this end, we undertake this review along two different threads. First, in Sec. II we provide a compact yet comprehensive overview of the current theoretical state of the art for the SM (and NP) description of semitauonic decays. This includes not only a survey of SM

predictions in the literature but also several novel results first calculated for this review.

Second, we provide a substantial review of the various experimental methods and strategies used to measure LFUV. This includes an assessment of the various experimental methods in Sec. III, and a summary of the LFUV measurements published to date in Sec. IV. An effort has been made to synthesize all of the available information from current measurements and, when possible, to make direct comparisons across experiments that provide further context. For instance, we present the various approaches toward reconstructing the momentum of the parent $b$ hadron in Sec. III.C and provide a comparison between the two hadronic $B$ tag measurements of $\mathcal{R}(D^{(*)})$ by *BABAR* and Belle in Sec. IV.A.1.

These two threads of the review are woven in Secs. V and VI into discussions of the main challenges arising from systematic uncertainties, and into discussions of current interpretations and combinations of the data, respectively. In particular, in Sec. V we provide an extended analysis of the main sources of systematic uncertainty in the LFUV measurements, and the prospects to control them in the future down to the percent level. This will be essential for establishing a conclusive tension with the standard model. We examine key challenges in computation, the modeling of $b$-hadron semileptonic decays in signal and background modes, and estimations of other important backgrounds. We also point out the potential sensitivity of $\mathcal{R}(D^{(*)})$ analyses to the assumptions used for the $B \to D^{**}\tau\nu$ branching fractions (Sec. V.C.2), which are presently overestimated compared to SM predictions.

Section VI begins by examining the $\mathcal{R}(D^{(*)})$ results and other SM tensions for different light-lepton normalization modes or isospin channels before turning to entirely revisit the world-average combinations of the $\mathcal{R}(D^{(*)})$ ratios. We specifically analyze the sensitivity of these combinations to the treatment of the correlation structure assigned to the uncertainties from $B \to D^{**}\ell\nu$ decays across different measurements and show that they may vary the degree of their current $\sim 3\sigma$ tension with the SM over approximately a $1\sigma$ range. As an illustration, incorporating such correlations as a free fit parameter in the combination, we show that the resulting $\mathcal{R}(D^{(*)})$ world averages would feature a tension of 3.6 standard deviations with respect to the SM. This is $0.5\sigma$ higher than the current world average (Amhis *et al.*, 2019). We further explore a comparison of inclusive versus exclusive measurements, caveats and challenges in establishing NP interpretations of the current $\mathcal{R}(D^{(*)})$ anomalies, and possible connections to anomalies in neutral-current rare $B$ decays.

Beyond the current state of the art, in Sec. VII we proceed to explore the power of future LFUV ratio measurements for a variety of hadronic states, taking into account the discussed prospects for the evolution of the systematic uncertainties and the data samples that LHCb and Belle II are expected to collect over the next two decades (Sec. VII.A). The power of future analyses to exploit full differential information is briefly explored (Sec. VII.B), as is the role of proposed future colliders (Sec. VII.C).

## II. THEORY OF SEMILEPTONIC DECAYS

In this section we introduce the foundational theoretical concepts required to describe $b \to c l\nu$ semileptonic decays. Throughout this review, we adopt the notation

$$l = \tau, \mu, e, \qquad \ell = \mu, e. \tag{2}$$

While our focus is the SM description of $b \to c l\nu$, in some contexts we present a model-independent discussion in order to accommodate discussion of beyond the standard model (BSM) physics. We first discuss $B \to D^{(*)} l\nu$ decays since they are of predominant experimental importance in current measurements, before turning to processes involving excited states, charm-strange mesons, charmonia, and baryons, as well as $b \to u l\nu$ and inclusive processes. The LFUV observables (anticipating their definitions in later parts of the review) for which predictions are discussed, and their respective sections, comprise

| | | | |
|---|---|---|---|
| $\mathcal{R}(D^{(*)})$: | Sec.II.D.1, | $F_L(D^*), P_\tau(D^{(*)})$: | Sec.II.D.2, |
| $\mathcal{R}(D^{**})$: | Sec.II.E, | $\mathcal{R}(D_s^{(*)})$: | Sec.II.E, |
| $\mathcal{R}(J/\psi)$: | Sec.II.E, | $\mathcal{R}(\Lambda_c^{(*)})$: | Sec.II.E, |
| $\mathcal{R}(\pi)$: | Sec.II.F, | $\mathcal{R}(\rho), \mathcal{R}(\omega)$: | Sec.II.F, |
| $\mathcal{R}(X_c)$: | Sec.II.G. | | |

### A. SM operator and amplitudes

In the SM, $b \to c l\nu$ processes are mediated by the weak charged current, generating the usual $V-A$ four-Fermi operator

$$\mathcal{O}_{\rm SM} = 2\sqrt{2} G_F V_{cb} (\bar{c}\gamma^\mu P_L b)(\bar{l}\gamma_\mu P_L \nu_l), \tag{3}$$

at leading electroweak order. Here we use the projectors $P_{L,R} = (1 \mp \gamma^5)/2$ and $G_F^{-1} = 8m_W^2/(\sqrt{2}g_2^2) = \sqrt{2}v^2$, with $v \simeq 246.22$ GeV (Zyla *et al.*, 2020). Further, $g_2$ denotes the SU(2) weak coupling constant, and $V_{cb}$ is the quark-mixing Cabibbo-Kobayashi-Masakawa (CKM) matrix element. The corresponding amplitude for this charged-current process has the diagrammatic form

$\mathcal{A}_{\rm SM}$ =

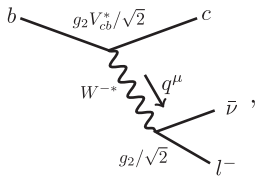


, (4)

in which the quarks may be "dressed" into various hadrons. It is conventional to define the momentum $q = p - p' = p_l + p_\nu$, where $p$ ($p'$) is the beauty (charm) hadron momentum.

The leptonic amplitude $W \to l\nu$ always takes the form of a Wigner-$D$ function $D^j_{m1,m2}(\theta_l, \phi_l)$, with $j = 0$ or 1, and $|m_{1,2}| \le j$. The helicity angles $\theta_l$ and $\phi_l$ are defined herein as in Fig. 1. We show also in Fig. 1 the definition of helicity

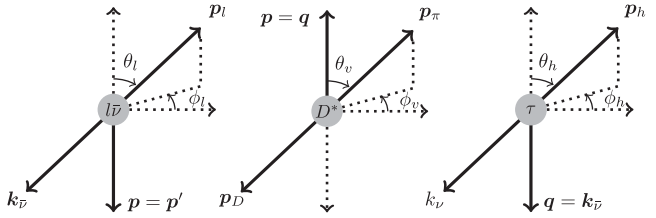


FIG. 1. Left: definition of the $\theta_l$ and $\phi_l$ helicity angles in the lepton pair rest frame. Center: definition of the $\theta_v$ and $\phi_v$ helicity angles in the $D^*$ rest frame. Right: definition of the $\theta_h$ and $\phi_h$ helicity angles in the $\tau$ rest frame for $B \to D^{(*)}(\tau \to h\nu)\bar{\nu}$ decay.

angles for subsequent $D^* \to D\pi$ or $\tau \to h\nu$ decays, for example, where $h$ is any hadronic system or $\ell\nu$. The helicity angle definition also applies to the case of $D^* \to D\gamma$, although with a different fully differential rate. Some literature uses the definition $\theta_l \to \pi - \theta_l$, such that caution must be used in adapting fits to fully differential measurements from one convention to the other. The phase $\phi_l$ is unphysical unless defined with reference to spin polarizers of the charm or beauty hadronic system or the lepton, such as the subsequent decay kinematics of the $\tau$ or charm hadron or the spin of the initial $b$ hadron. For example, in $B \to (D^* \to D\pi)\ell\nu$ the only physical phase is $\chi \equiv \phi_l - \phi_v$.

### B. Hadronic matrix elements and form factors

The predominant theory uncertainty in $B \to D^{(*)}l\nu$ arises in the description of the hadronic matrix elements $\langle D^{(*)}|\bar{c}\Gamma b|\bar{B}\rangle$,[1] where (anticipating the subsequent discussion of NP) $\Gamma$ is any Dirac operator. More generally, one seeks a theoretical framework to describe the matrix elements $\langle {}^{2s_c+1}(L^c)_{J_c}|\bar{c}\Gamma b|{}^{2s_b+1}(L^b)_{J_b}\rangle$, using here the spectroscopic notation to describe the hadron in terms of its quark constituents' total spin $s$, their orbital angular momentum $L = S, P, D, \ldots$, and the total angular momentum of the hadron $J$. We first focus on the description for $B \to D^{(*)}$, i.e., ${}^1S_0 \to {}^1S_0$ or ${}^3S_1$: the ground-state charmed mesons.

Hadronic matrix elements incorporate nonperturbative QCD and cannot be computed from first principles. However, the transition matrix element between hadrons of definite spin and parity mediated by any particular operator can be described by a finite set of amplitudes involving partial waves of definite orbital angular momentum. Each such amplitude can be represented by a tensor product of the external momenta, polarizations, and spins multiplied by an unknown hadronic function: a form factor. One may represent the matrix element by different linear combinations of these tensor products, thereby defining a basis for the form factors.

[1]All definitions and sign conventions hereafter apply to $b \to c$ transitions; they may be extended to $\bar{b} \to \bar{c}$ with the appropriate sign changes. To emphasize this, while we do not typically distinguish between $\bar{B} \to D^{(*)}$ and $B \to \bar{D}^{(*)}$ in this discussion, we do retain such notation in the explicit definition of matrix elements or where charge assignments of other particles have been made explicit. Throughout the review, inclusion of charge-conjugate decay modes is implied unless otherwise stated.

For $B \to D^{(*)}$ SM transitions, the matrix elements are represented by two (four) independent form factors. In terms of two (three) common form factor bases,

$$\begin{aligned}\langle D|\bar{c}\gamma^\mu b|\bar{B}\rangle &= f_+(p+p')^\mu \\ &\quad + (f_0 - f_+)q^\mu(m_B^2 - m_D^2)/q^2 \\ &= \sqrt{m_B m_D}[h_+(v+v')^\mu + h_-(v-v')^\mu], \end{aligned} \tag{5a}$$

$$\begin{aligned}\langle D^*|\bar{c}\gamma^\mu b|\bar{B}\rangle &= 2i\tilde{g}\varepsilon^{\mu\nu\alpha\beta}\epsilon_\nu^* p'_\alpha p_\beta \\ &= i\sqrt{m_B m_{D^*}}h_V\varepsilon^{\mu\nu\alpha\beta}\epsilon_\nu^* v'_\alpha v_\beta \\ &= 2iV(m_B + m_{D^*})^{-1}\varepsilon^{\mu\nu\alpha\beta}\epsilon_\nu^* p'_\alpha p_\beta, \end{aligned} \tag{5b}$$

$$\begin{aligned}\langle D^*|\bar{c}\gamma^\mu\gamma^5 b|\bar{B}\rangle &= f\epsilon^{*\mu} + a_+\epsilon^*\cdot p(p+p')^\mu + a_-(\epsilon^*\cdot p)q^\mu \\ &= \sqrt{m_B m_{D^*}}[h_{A_1}(w+1)\epsilon^{*\mu} \\ &\quad - h_{A_2}(\epsilon^*\cdot v)v^\mu - h_{A_3}(\epsilon^*\cdot v)v'^\mu], \\ &= A_1(m_B + m_{D^*})\epsilon^{*\mu} - A_2\frac{\epsilon^*\cdot p(p+p')^\mu}{m_B + m_{D^*}} \\ &\quad + 2m_{D^*}q^\mu(A_0 - A_3)(\epsilon^*\cdot p)/q^2, \end{aligned} \tag{5c}$$

noting that $\langle D|\bar{c}\gamma^\mu\gamma^5 b|\bar{B}\rangle = 0$ because of angular momentum and parity conservation. Here we have used the spectroscopic basis $\{f_+, f_0, f, \tilde{g}, a_\pm\}$ [cf. Isgur *et al.* (1989a)];[2] the heavy-quark symmetry (HQS) basis $\{h_\pm, h_V, h_{A_{1,2,3}}\}$ (Neubert, 1994); and the basis $\{V, A_{0,1,2,3}\}$ (Wirbel, Stech, and Bauer, 1985), in which $2m_{D^*}A_3 = A_1(m_B + m_{D^*}) - A_2(m_B - m_{D^*})$. Furthermore, the velocities $v = p/m_B$ and $v' = p'/m_{D^{(*)}}$, $\epsilon^*$ is the $D^*$ polarization vector, and the recoil parameter

$$w = v\cdot v' = \frac{m_B^2 + m_{D^{(*)}}^2 - q^2}{2m_B m_{D^{(*)}}}. \tag{6}$$

The form factors are functions of $q^2$ or, equivalently, $w$. Their explicit forms may also involve the scheme-dependent parameters $m_b/m_c$ and $\alpha_s$, although any such scheme dependency must vanish in physical quantities. In the HQS basis, $h_{A_1}$ and the three form factor ratios

$$\begin{aligned} R_1(w) &= \frac{h_V}{h_{A_1}}, \qquad R_2(w) = \frac{h_{A_3} + r^* h_{A_2}}{h_{A_1}}, \\ R_0(w) &= \frac{(w+1)h_{A_1} - (w - r^*)h_{A_3} - (1 - wr^*)h_{A_2}}{(1+r^*)h_{A_1}}, \end{aligned} \tag{7}$$

where $r^{(*)} = m_{D^{(*)}}/m_B$, fully describe the $B \to D^*$ transition. Note that $R_0$ enters only into terms proportional to $m_l$.

Particular care must be taken with sign conventions in Eqs. (5): For $B \to D^{(*)}$, the conventional choice in the literature, and here, is such that $\mathrm{Tr}[\gamma^\mu\gamma^\nu\gamma^\rho\gamma^\sigma\gamma^5] = +4i\varepsilon^{\mu\nu\rho\sigma}$, which is equivalent to fixing the identity $\sigma^{\mu\nu}\gamma^5 \equiv -(i/2)\varepsilon^{\mu\nu\rho\sigma}\sigma_{\rho\sigma}$, with $\sigma_{\mu\nu} = (i/2)[\gamma^\mu, \gamma^\nu]$. One may further choose either $\varepsilon^{0123} = +1$ or $-1$. In $B \to D^{**}$ literature, as

[2]The form factor $\tilde{g}$ is often written as $g$ but should not be confused with $g = 2\tilde{g}$ in the helicity basis defined in Eq. (8).

well as $\Lambda_b \to \Lambda_c$, the choice is instead typically $\mathrm{Tr}[\gamma^\mu\gamma^\nu\gamma^\rho\gamma^\sigma\gamma^5] = -4i\varepsilon^{\mu\nu\rho\sigma}$, which is equivalent to $\sigma^{\mu\nu}\gamma^5 \equiv +(i/2)\varepsilon^{\mu\nu\rho\sigma}\sigma_{\rho\sigma}$. These sign choices affect the sign of $R_1$ but leave physical quantities unchanged provided they are used consistently both in the form factor definitions and in the calculation of the amplitudes. Care must be taken in adapting form factor fit results obtained in one convention to expressions defined in the other. In our sign conventions, the form factor ratio $R_1 > 0$.

An additional common choice for $B \to D^*$ decays is the helicity basis [cf. Boyd, Grinstein, and Lebed (1996, 1997)] with form factors $\{g, f, F_1, P_1\}$ that are particularly convenient for expressing the $B \to D^*$ helicity amplitudes. Explicit relations between the HQS and helicity bases are

$$h_{A_1} = \frac{f}{m_B\sqrt{r^*}(w+1)}, \qquad h_V = g m_B\sqrt{r^*}, \tag{8a}$$

$$h_{A_1}[w - r^* - (w-1)R_2] = \frac{F_1}{m_B^2\sqrt{r^*}(w+1)}, \tag{8b}$$

$$h_{A_1}R_0 = P_1. \tag{8c}$$

The SM differential rate can then be written compactly in terms of Legendre polynomials of $\cos\theta_l$,

$$\begin{aligned}\frac{d^2\Gamma}{dw\,d\cos\theta_\ell} = {}& 2\Gamma_0\sqrt{w^2-1}\,r^{*3}\left[\frac{\bar{q}^2 - r_l^2}{\bar{q}^2}\right]^2 \\ & \times\left\{\left(1+\frac{r_l^2}{2\bar{q}^2}\right)(\mathcal{H}_+ + 2\bar{q}^2\mathcal{H}_1) + \frac{3r_l^2}{2\bar{q}^2}\mathcal{H}_0 \right. \\ & \left. + \cos\theta_l\mathcal{H}_{+0} + \frac{3\cos^2\theta_l - 1}{2}\left[\frac{\bar{q}^2 - r_l^2}{\bar{q}^2}\right](\bar{q}^2\mathcal{H}_1 - \mathcal{H}_+)\right\},\end{aligned} \tag{9}$$

in which $\Gamma_0 \equiv G_F^2\eta_{\mathrm{EW}}^2|V_{cb}|^2/(192\pi^3)$, $r_l = m_l/m_B$, $\bar{q}^2 = q^2/m_B^2 = 1 - 2r^*w + r^{*2}$, $\eta_{\mathrm{EW}} \simeq 1 + \alpha/\pi\log(m_Z/m_B) \simeq 1.0066$ is an electroweak correction (Sirlin, 1982), and

$$\mathcal{H}_1 = \frac{f^2}{r^* m_B^2} + g^2 r^* m_B^2(w^2-1), \tag{10a}$$

$$\mathcal{H}_+ = \frac{F_1^2}{r^* m_B^4}, \tag{10b}$$

$$\mathcal{H}_0 = P_1^2(r^*+1)^2(w^2-1), \tag{10c}$$

$$\mathcal{H}_{+0} = 6\bar{q}^2 fg\sqrt{w^2-1} - \frac{3r_l^2}{\bar{q}^2}\sqrt{\mathcal{H}_+\mathcal{H}_0}. \tag{10d}$$

The $\theta_l$-independent term in Eq. (9) is simply $(1/2)d\Gamma/dw$. The overall sign of the $\cos\theta_l$ term and the relative sign of the $fg$ term in $\mathcal{H}_{+0}$ are sensitive to sign conventions. In the massless lepton limit, it is common to express the differential rate $d\Gamma/dw$ in terms of the single form factor combination

$$\mathcal{F}^2(w) = \frac{\mathcal{H}_+ + 2\bar{q}^2\mathcal{H}_1}{(1-r^*)^2(w+1)^2 + 4w(w+1)\bar{q}^2}, \tag{11}$$

which is normalized such that $\mathcal{F}(1) = h_{A_1}(1)$.

The $B \to D$ rate may be expressed similarly. In the form factor basis $\{\mathcal{G} \equiv V_1, S_1\}$,[3] defined via

$$\mathcal{G} \equiv V_1 = h_+ - \frac{1-r}{1+r}h_-, \tag{12a}$$

$$S_1 = h_+ - \frac{1+r}{1-r}\frac{w-1}{w+1}h_-, \tag{12b}$$

the SM differential rate has the same form as Eqs. (9) and (10), but with $r^* \to r$,

$$\mathcal{H}_+ = V_1^2(1+r)^2(w-1)^2, \tag{13a}$$

$$\mathcal{H}_0 = S_1^2(1-r)^2(w+1)^2, \tag{13b}$$

and by definition no $f$ or $g$ terms, i.e., $\mathcal{H}_1 = 0$ and $\mathcal{H}_{+0} = -3r_l^2/\bar{q}^2\sqrt{\mathcal{H}_+\mathcal{H}_0}$.

Note that the expressions of this section apply similarly to any other ${}^1S_0 \to {}^1S_0$ or ${}^3S_0$ transition, including $B \to \pi l\nu$ and $B \to \rho l\nu$ (with the additional replacement of $V_{cb} \to V_{ub}$).

### C. Theoretical frameworks

Various theoretical approaches exist to parametrize the $B \to D^{(*)}$ or other exclusive decay form factors. Broadly speaking, these fall into the following four overlapping categories:

(1) Use of the functional properties of the hadronic matrix elements (analyticity, unitarity, and dispersion relations) to constrain the form factor structure.
(2) Use of heavy-quark effective theory (HQET) to generate order-by-order relations in $1/m_{c,b}$ and $\alpha_s$ between form factors.
(3) Various quark models, including those that may approximately compute the form factors (in various regimes), such as QCD sum rule (QCDSR) and light cone sum rule (LCSR) approaches.
(4) Lattice QCD (LQCD) calculations, presently available only for a limited subset of form factors and kinematic regimes.

The details of the various approaches to the form factor parametrization are particularly important for measurements that are sensitive to the differential shape of exclusive semileptonic decays, such as the extraction of the CKM matrix element $|V_{cb}|$. Hadronic uncertainties, however, mostly factor out of observables that consider ratios of $|V_{cb}|$-dependent quantities, including measurements that probe lepton universality relations between the $B \to D^{(*)}\ell\nu$ and $B \to D^{(*)}\tau\nu$ decays and other exclusive processes. Instead, in the latter context the main role and importance of form factor parametrizations lies in their ability to generate predictions for lepton universality relations, and the precision thereof.

[3]Some literature uses the notation $V_1$, while others $\mathcal{G}$.

### 1. Dispersive bounds

A dispersion relations-based approach does not alone generate lepton universality relations between the $B \to D^{(*)} l\nu$ rates or other exclusive processes, but does provide crucial underlying theoretical inputs to approaches that do. The dispersive approach (Boyd, Grinstein, and Lebed, 1996, 1997) begins with the observation that the matrix element $\langle H_c|J|H_b\rangle$ for a hadronic transition $H_b \to H_c$, mediated by current $J = \bar{c}\Gamma b$, may be analytically continued beyond the physical regime $q^2 < (m_{H_b} - m_{H_c})^2 \equiv q_-^2$ into the complex $q^2$ plane. For $q^2 > (m_{H_b^0} + m_{H_c^0})^2 \equiv q_+^2$, where $H_{c,b}^0$ denote the lightest pair of hadrons that couple to $J$, the matrix element features a branch cut from the crossed process $H_b^0 H_c^{0\dagger}$ pair production. For $B \to D^*$ processes, it is typical to take $q_+^2 \equiv (m_B + m_{D^*})^2$ for both vector and axial vector currents. For $B_c \to J/\psi$, the branch points are taken as $(m_B + m_D)^2$ and $(m_{B^*} + m_D)^2$ for vector and axial vector currents, respectively. A $bc$ bound state that is created by $J$ but with mass $m^2 < q_+^2$ is a "subthreshold" resonance.

The conformal transformation

$$z(q^2, q_0^2) = \frac{\sqrt{q_+^2 - q^2} - \sqrt{q_+^2 - q_0^2}}{\sqrt{q_+^2 - q^2} + \sqrt{q_+^2 - q_0^2}} \tag{14}$$

maps $q^2 > q_+^2$ to the boundary of the unit circle $|z| = 1$ that is centered at $q^2 = q_0^2$. Two common choices of $q_0^2$ are $q_0^2 = q_-^2$, in which case $z(w = 1) = 0$, and $q_0^2 = q_+^2(1 - [1 - q_-^2/q_+^2]^{1/2}) \equiv q_{\rm opt}^2$, which minimizes $|z(q^2 = 0)|$. This allows the matrix element to be written as an analytic function of $z$ on the unit disk $|z| \le 1$, up to simple poles that are expected at each subthreshold resonance. These poles must fall on the interval $q_-^2 \le q^2 \le q_+^2 \Leftrightarrow (0 \ge) z_- \ge z \ge -1$.

The second ingredient is the vacuum polarization $\Pi_J = i \int d^4x e^{iqx} \langle 0|TJ^\dagger(x)J(0)|0\rangle$, which obeys a once-subtracted dispersion relation

$$\chi_J(q^2) \equiv \frac{\partial \Pi_J}{\partial q^2} = \frac{1}{\pi} \int \frac{dt}{(t - q^2)^2} \mathrm{Im}\Pi_J. \tag{15}$$

The QCD correlator $\chi_J$ can be computed at one loop in perturbative QCD for $q^2 > q_+^2$ and then analytically continued to $q^2 < q_-^2$. $\mathrm{Im}\Pi_J$ may be reexpressed as a phase-space-integrated sum over a complete set of $b$- and $c$-hadronic states $\sim \sum_{X = H_b H_c^\dagger, \ldots} |\langle 0|J|X\rangle|^2$ with appropriate parity and spin. For $J = \bar{c}\gamma^\mu b$, one may have $H_b H_c^\dagger = BD^\dagger$, $BD^{*\dagger}$, etc. The positivity of each summand allows the dispersion relation to provide an upper bound, a so-called weak unitarity bound, for any given hadron pair $H_b H_c^\dagger$. (A "strong" unitarity bound would, by contrast, impose the upper bound on a finite sum of hadron pairs coupling to $J$.) Crossing symmetry permits these bounds to be applied to the transition matrix elements $\langle H_c|J|H_b\rangle$ of interest here.

Making use of the conformal transformation, the unitarity bound can be expressed in the form

$$\int_{|z|=1} \frac{dz}{2\pi i z} \sum_i |P_i^J(z) \phi_i^J(z) F_i^J(z)|^2 \le 1, \tag{16}$$

in which $F_i^J$ is a basis of form factors and the "outer" functions $\phi_i^J$ are analytic weight functions that encode both their $q^2$-dependent prefactors arising in $\langle H_c|J|H_b\rangle$, as well as incorporating the $1/\sqrt{\pi\chi_J}$ prefactor. The additional Blaschke factors $P_i^J$ satisfy $|P_i^J(|z| = 1)| = 1$ by construction and do not affect the integrand on the $|z| = 1$ contour. However, the choice $P_i^J = \prod_\alpha (z - z_{\alpha,i})/(1 - z z_{\alpha,i})$ explicitly cancels the known poles at $z = z_{\alpha,i}$ on the negative real axis. Each term in the sum must then be analytic, i.e., $P_i^J(z)\phi_i^J(z)F_i^J(z) = \sum_{n=0}^\infty a_n^{Ji} z^n$, so that Eq. (16) requires the $a_n^{Ji}$ coefficients to satisfy a unitarity bound $\sum_{i,n} |a_n^{Ji}|^2 \le 1$.

The Boyd-Grinstein-Lebed (BGL) parametrization (Boyd, Grinstein, and Lebed, 1996; Boyd, Grinstein, and Lebed, 1997) uses this approach to express the $f$, $g$, $F_1$, and $P_1$ form factors in terms of an analytic expansion in $z = z(q^2, q_-^2)$. In particular, for the light-lepton modes, with $F_A = f, F_1$,

$$g(z) = \frac{1}{P_V(z)\phi_g(z)} \sum_n a_n^g z^n, \qquad \sum_n |a_n^g|^2 \le 1,$$

$$F_A(z) = \frac{1}{P_A(z)\phi_{F_A}(z)} \sum_n a_n^{F_A} z^n, \qquad \sum_{F_A, n} |a_n^{F_A}|^2 \le 1,$$

further noting that $F_1(q_-^2)/\phi_{F_1}(q_-^2) = f(q_-^2) m_B (1 - r^*)/\phi_f(q_-^2)$ from Eq. (8b). This relatively unconstrained parametrization provides a hadronic model-independent approach to measuring $|V_{cb}|$ from light leptonic $B \to D^* \ell\nu$ modes but does not relate $B \to D^*\tau\nu$ to $B \to D^*\ell\nu$. For example, a fit to light-lepton data, taking $m_\ell \to 0$, to determine $f$, $g$, and $F_1$ provides no prediction for $P_1$, and hence no prediction for the $B \to D^*\tau\nu$ rate. (The general SM expectation remains, however, that the unitarity bound for $P_1$ should not be violated in a direct fit to the $B \to D^*\tau\nu$ data.) Instead, additional theoretical inputs are required.

### 2. Heavy-quark effective theory

HQET inputs may be combined with the BGL approach in order to generate SM (or NP) predictions for lepton universality observables. A "heavy" hadron is defined as containing one heavy valence quark [i.e., the heavy-quark mass $m_Q \gg \mathcal{O}(\Lambda_{\rm QCD})$, the QCD scale] dressed by light-quark and gluon degrees of freedom (so-called brown muck) in a particular spin and parity state. An HQET (Isgur and Wise, 1989, 1990; Eichten and Hill, 1990; Georgi, 1990) [for a review, see Neubert (1994)] is an effective field theory of the brown muck in which interactions with the heavy quark enter at higher orders in $1/m_Q$. An apt analogy arises in atomic physics in which the electronic states are insensitive to the nuclear spin state up to hyperfine corrections. This provides a hadronic model-independent parametrization not only of the spectroscopy of heavy hadrons but also order by order in $1/m_Q$ relations between their transition matrix elements. The form factors of $B \to D^{(*)}\ell\nu$ are then related to those of $B \to D^{(*)}\tau\nu$ and allow for lepton universality predictions.

In this language, the spectroscopic $^1S_0$ and $^3S_1$ states (e.g., $D$ and $D^*$ or $B$ and $B^*$) may instead be considered to belong to a heavy-quark (HQ) spin symmetry doublet of a pseudoscalar ($P$) and vector ($V$) meson, formed by the tensor product of the light degrees of freedom in a spin-parity $s_\ell^P = 1/2^-$ state, combined with the heavy-quark spin as follows: $(1/2)_{\mathrm{HQ}} \otimes (1/2)_{\mathrm{light}} = \mathbf{0} \oplus \mathbf{1}$. Their masses can be expressed as

$$m_{P,V} = m_Q + \bar{\Lambda} - \frac{\lambda_1}{2m_Q} \mp \frac{(2J_{V,P}+1)\lambda_2}{2m_Q} + \cdots, \tag{17}$$

where $\bar{\Lambda} = \mathcal{O}(\Lambda_{\mathrm{QCD}})$ is the brown muck kinetic energy for $m_Q \to \infty$ and $\lambda_{1,2} = \mathcal{O}(\Lambda_{\mathrm{QCD}}{}^2)$. Furthermore, one expects that in the limit in which $m_Q \to \infty$ (and $\alpha_s \to 0$), the heavy-quark limit, the physics of heavy hadron flavor-changing transitions such as $B \to D^{(*)}$ should be insensitive to, and therefore preserve, the spin of the underlying heavy quarks while being sensitive to the change in heavy-quark velocity.

Following this intuition, the QCD kinetic term $\bar{Q}(i\not{D} - m_Q)Q$ may itself be reorganized into an effective theory of brown muck (i.e., a HQET) parametrized by the heavy-quark velocity $v = p_Q/m_Q$. This effective theory features a $1/m_Q$ expansion in which the leading-order terms conserve heavy-quark spin while higher-order terms in $1/m_Q$ do not. A heavy-quark flavor violating interaction like $J = \bar{c}\Gamma b$ can be similarly reorganized such that, at leading order, the transition is sensitive only to the difference of the incoming and outgoing heavy hadron velocities $v$ and $v'$, respectively. It is then natural to express the matrix elements as in Eq. (5), with the natural form factor basis in the SM being $h_\pm, h_V, h_{A_{1,2,3}}$.

When organized in this way, the key result is that any $B \to D^{(*)}$ matrix element can be written as a spin trace

$$\frac{\langle D^{(*)}|\bar{c}\Gamma b|\bar{B}\rangle}{\sqrt{m_{D^{(*)}} m_B}} = -\xi(w)\mathrm{Tr}[\bar{H}_{v'}^{(c)}\Gamma H_v^{(b)}] + \mathcal{O}(\varepsilon_c, \varepsilon_b, \hat{\alpha}_s), \tag{18}$$

where $H^{(c,b)}$ are HQET representations of the HQ doublet and $\xi(w)$ is a leading *Isgur-Wise function*. Higher-order terms in $\varepsilon_{c,b} = \bar{\Lambda}/(2m_{c,b})$ can be similarly systematically constructed in terms of universal subleading Isgur-Wise functions, while radiative corrections in $\hat{\alpha}_s = \alpha_s/\pi$ can be incorporated at arbitrary fixed order. Heavy-quark flavor symmetry implies that $\xi(1) = 1$, which is preserved at order $\varepsilon_{c,b}$ by Luke's theorem.

The Caprini-Lellouch-Neubert (CLN) parametrization (Caprini, Lellouch, and Neubert, 1998) applies dispersive bounds to the $B \to D$ form factor $V_1$, expanded up to cubic order as

$$\frac{V_1(w)}{V_1(1)} = 1 - \rho_1^2(w-1) + c_1(w-1)^2 + d_1(w-1)^3 + \cdots. \tag{19}$$

It thus extracts approximate relations between the parameters $\rho^2$, $c_1$, and $d_1$ by saturating the dispersive bounds at (the then) $1\sigma$ uncertainty in the QCD correlators $\chi_J$. The parametrization then makes use of heavy-quark symmetry to relate this form factor to all other form factors in the $B \to D^{(*)}$ system, incorporating additional quark model inputs from QCDSRs to constrain the $1/m_{c,b}$ terms. In particular, predictions are obtained for a $z$ expansion of $h_{A_1}$, with coefficients dependent only on $\rho_1^2$, plus predictions for $R_{1,2,0}(w)$ up to a fixed order in $w-1$ as follows: $R_i(w) = R_i(1) + R_i'(1)(w-1) + (1/2)R_i''(1)(w-1)^2 + \cdots$.

The intercepts $R_i(1)$ are theoretically correlated order by order in the HQ expansion with the slope and gradients $R_i^{(\prime,\prime\prime)}(1)$, and therefore must be determined simultaneously when measured. A common experimental fitting practice of floating $R_{1,2}(1)$ while keeping $R_{1,2}^{(\prime,\prime\prime)}(1)$ fixed to their QCDSR predictions is inconsistent with HQET at subleading order, when fits are performed to recent higher-precision unfolded datasets, such as the 2017 Belle tagged analysis (Abdesselam *et al.*, 2017). The Bernlochner-Ligeti-Papucci-Robinson (BLPR) parametrization (Bernlochner *et al.*, 2017) removes this inconsistency and exploits higher-precision data-driven fits to the subleading IW functions to obviate the need for QCDSR inputs. It furthermore consistently incorporates the $1/m_{c,b}$ terms for NP currents, which are important for NP predictions of $B \to D^{(*)}\tau\nu$.

There has been a long-standing debate about the size of the $1/m_c^2$ corrections, partly because quark-model-based calculations predicted them to have coefficients somewhat larger than unity. Recent data-driven fits, however, in the baryonic $\Lambda_b \to \Lambda_c$ system provide good evidence that the $1/m_c^2$ corrections obey power counting expectations (Bernlochner *et al.*, 2018); see also Bordone *et al.* (2020) in regard to $B_{(s)} \to D_{(s)}^*$.

### 3. Quark models

Beyond dispersive bounds and HQET, quark-model-based approaches have historically played an important role in descriptions of the form factors and have provided useful constraints in generating lepton universality predictions. The Isgur-Scora-Grinstein-Wise updated model (ISGW2) parametrization (Isgur *et al.*, 1989b; Scora and Isgur, 1995) implements a nonrelativistic constituent quark model, providing estimates of the form factors by expressing the transition matrix elements for each spectroscopic combination of hadrons in terms of wave-function overlap integrals. In addition, it incorporates leading-order and $\mathcal{O}(1/m_{c,b})$ constraints from heavy-quark symmetry and higher-order hyperfine corrections.

The ISGW2 parametrization of the form factors is treated as fully predictive, being typically implemented without any undetermined parameters. This amounts to fixed choices for, e.g., the heavy- and light-quark masses or the brown muck kinetic energy $\bar{\Lambda}$. It therefore is not considered to provide state-of-the-art form factors compared to data-driven fits. Nonrelativistic quark models may, however, be useful choices for double-heavy hadron transitions such as $B_c \to J/\psi$ or $\eta_c$ [for a recent example see Penalva, Hernández, and Nieves (2020)], where heavy-quark symmetry cannot be applied.

### 4. Sum rules

QCDSRs exploit the analytic properties of three-point correlators constructed by sandwiching an operator of interest

with appropriate interpolating hadronic currents. This allows the expression of an Isgur-Wise function in terms of the Borel transform of the correlator, the latter of which can be computed in perturbation theory via an operator product expansion (OPE). One must further assume quark-hadron duality to estimate the spectral densities of relevant excited states. Renormalization improved results for the $1/m_{c,b}$ Isgur-Wise functions and their gradients at zero recoil are known (Neubert, Ligeti, and Nir, 1993a, 1993b; Ligeti, Nir, and Neubert, 1994; Neubert, 1994). While theoretical uncertainties associated with the perturbative calculations are well understood, there is no systematic approach to assessing uncertainties arising from quark-hadron duality and scale variations. Rough estimates of the uncertainties are large compared to the precision obtained by more recent data-driven methods.

LCSRs operate in a similar spirit to QCDSRs, reorganizing the OPE such that one expands in the "transverse distance" of partons from the light cone. The resulting sum rules are valid for the regime in which the outgoing hadron kinetic energy is large. LCSRs have broad application in exclusive heavy-light quark transitions, such as for $b \to u$ transitions including $B \to \rho$, $\omega$, or $\pi$, in which the valence parton is highly boosted compared to the spectator.

#### 5. Lattice calculations

LQCD results are available for the SM form factors at zero recoil for both $B_{(s)} \to D_{(s)}$ and $B_{(s)} \to D^*_{(s)}$. The most precise $B \to D^{(*)}$ results are (Aoki *et al.*, 2020)

$$\mathcal{G}(1) \equiv V_1(1) = 1.054(4)_{\text{stat}}(8)_{\text{syst}},$$
$$\mathcal{F}(1) = 0.906(4)_{\text{stat}}(12)_{\text{syst}}. \tag{20}$$

LQCD results for the $B_{(s)} \to D_{(s)}$ form factors $f^{(s)}_{+,0}$ are available beyond zero recoil with respect to the optimized expansion in $z = z(q^2, q^2_{\text{opt}})$. Further, preliminary results for the $B_s \to D^*_s$ (Harrison and Davies, 2021) and $B \to D^*$ (Bazavov *et al.*, 2021) SM form factors beyond zero recoil have recently become available.

The $B \to D$ LQCD data allow for lattice predictions for the differential rate of $B \to D\tau\nu$ and, when combined with HQET relations plus QCD sum rule predictions, one may also predict $B \to D^*\tau\nu$, but with slightly poorer precision compared to data-driven approaches (Bernlochner *et al.*, 2017). Beyond zero recoil LQCD results are also available for $B_c \to J/\psi l\nu$ (Harrison, Davies, and Lytle, 2020a) (see Sec. II.E), as well as for the baryonic $\Lambda_b \to \Lambda_c l\nu$ (Detmold, Lehner, and Meinel, 2015) decays including NP matrix elements.

### D. Ground-state observables and predictions

#### 1. Lepton universality ratios

Lepton universality in $b \to c l\nu$ may be probed by comparing the ratios of total rates for $l = e$, $\mu$, and $\tau$, in particular, the ratio of the semitauonic to light semileptonic exclusive decays

$$\mathcal{R}(H_c) = \frac{\Gamma[H_b \to H_c \tau\nu]}{\Gamma[H_b \to H_c \ell\nu]}, \qquad \ell = e, \mu, \tag{21}$$

where $H_{c,b}$ are any allowed pair of $c$ and $b$ hadrons. [The ratios of the electron and muon modes are in agreement with SM predictions, i.e., near unity; see Sec. VI.A. One may also consider ratios $\mathcal{R}(H_u)$ for $H_b \to H_u\tau\nu$ decays, in which the valence charm quark is replaced by a $u$ quark.] The ratios $R(H_c)$ should differ from unity not only from the reduced phase space as $m_\tau \gg m_{e,\mu}$, but also because of the mass-dependent coupling to the longitudinal $W$ mode. The theory uncertainties entering into the SM predictions for this quantity are then dominated by uncertainties in the form factor contributions coupling exclusively to the lepton mass, such as the form factor ratios $S_1/V_1$ and $R_0(w)$ in $B \to D$ and $D^*$, respectively.

In Table I we show a summary of various predictions as collated by the Heavy Flavor Averaging Group (HFLAV) (Amhis *et al.*, 2019). Before 2017, $\mathcal{R}(D^{(*)})$ predictions based on experimental data used the CLN parametrization, since this was the only experimentally implemented form factor parametrization. An unfolded analysis by Belle (Abdesselam *et al.*, 2017) has since allowed the use of other parametrizations, with the different (and more consistent) theoretical inputs as described in Table I. At present, given the different theoretical inputs and correlations in the results of these analyses, the HFLAV SM prediction is a naive arithmetic average of the $\mathcal{R}(D)$ and $\mathcal{R}(D^*)$ predictions and uncertainties for each mode independently. A subsequent Belle 2018 analysis of $B \to D^*\ell\nu$ (Waheed *et al.*, 2019) provided response functions and efficiencies, into which different parametrizations may be folded to generate predictions for bin yields in various marginal distributions. For example, Gambino, Jung, and Schacht (2019) found $\mathcal{R}(D^*) = 0.254^{+0.007}_{-0.006}$ and Jaiswal, Nandi, and Patra (2020) found $0.251^{+0.004}_{-0.005}$, with and without LCSR inputs, respectively. Finally, preliminary lattice results for $B \to D^*$ beyond zero recoil predict $\mathcal{R}(D^*) = 0.266(14)$ (Bazavov *et al.*, 2021).

On occasion, the phase-space constrained ratio

$$\tilde{\mathcal{R}}(H_c) = \frac{\int_{m_\tau^2}^{Q^2} dq^2 (d\Gamma[H_b \to H_c \tau\nu]/dq^2)}{\int_{m_\tau^2}^{Q^2} dq^2 (d\Gamma[H_b \to H_c \ell\nu]/dq^2)}, \qquad \ell = e, \mu, \tag{22}$$

is also considered, in which the relative phase-space suppression for the tauonic mode is factored out. For instance, the SM predictions are, using the fit results of Bernlochner *et al.* (2017),

$$\tilde{\mathcal{R}}(D) = 0.576(3), \qquad \tilde{\mathcal{R}}(D^*) = 0.342(2), \tag{23}$$

with a correlation coefficient of 0.53.

#### 2. Longitudinal and polarization fractions

In the helicity basis for the $D^*$ polarization, the $D^* \to D\pi$ decay amplitudes within $B \to (D^* \to D\pi)l\nu$ decays are simply $L = 1$ spherical harmonics $e^{i\lambda\phi_v} Y_{1,\lambda}(\theta_v)$, with respect to the helicity angles defined in Fig. 1. That is, the $B \to (D^* \to D\pi)l\nu$ amplitudes may be expressed in the schematic form

TABLE I. $\mathcal{R}(D^{(*)})$ predictions as currently collated and arithmetically averaged by HFLAV. Predictions shown below the HFLAV row are not included in the arithmetic average.

| Inputs | $\mathcal{R}(D)$ | $\mathcal{R}(D^*)$ | Correlation |
|---|---|---|---|
| LQCD + Belle/*BABAR* data[a] | $0.299 \pm 0.003$ | ⋯ | ⋯ |
| LQCD + HQET $\mathcal{O}(\alpha_s, 1/m_{c,b})$ + Belle 2017 analysis[b,c] | $0.299 \pm 0.003$ | $0.257 \pm 0.003$ | 0.44 |
| BGL + BLPR + $\sim 1/m_c^2$ + Belle 2017 analysis[d] | ⋯ | $0.260 \pm 0.008$ | ⋯ |
| BGL + BLPR + $\sim 1/m_c^2$ + Belle 2017 analysis[e] | $0.299 \pm 0.004$ | $0.257 \pm 0.005$ | 0.1 |
| HFLAV arithmetic averages | $0.299 \pm 0.003$ | $0.258 \pm 0.005$ | ⋯ |
| LQCD[f] | $0.300 \pm 0.008$ | ⋯ | ⋯ |
| CLN + Belle data[g] | ⋯ | $0.252 \pm 0.003$ | ⋯ |

[a]See Bigi and Gambino (2016).
[b]See Abdesselam *et al.* (2017).
[c]The "BLPR" parametrization (Bernlochner *et al.*, 2017).
[d]Includes estimations of $1/m_c^2$ uncertainties (Bigi, Gambino, and Schacht, 2017). See also Gambino, Jung, and Schacht (2019).
[e]Fits nuisance parameters for $1/m_c^2$ terms (Jaiswal, Nandi, and Patra, 2017). See also Jaiswal, Nandi, and Patra (2020).
[f]World average (Aoki *et al.*, 2020).
[g]See Fajfer, Kamenik, and Nisandzic (2012).

$\sum_\lambda A_\lambda[B \to D^* l\nu](\theta_l, \phi_l - \phi_v) \times Y_{1,\lambda}(\theta_v)$. The $D^*$ longitudinal polarization fraction[4]

$$F_{L,l}(D^*) = \frac{\Gamma_{\lambda=0}[B \to D^* l\nu]}{\Gamma[B \to D^* l\nu]}, \tag{24}$$

thus arises as a physical quantity in $B \to (D^* \to D\pi) l\nu$ decays via the marginal differential rate

$$\frac{1}{\Gamma}\frac{d\Gamma_{B\to(D^*\to D\pi)l\nu}}{d\cos\theta_v} = \frac{3}{2}\left[F_{L,l}\cos^2\theta_v + (1 - F_{L,l})\frac{\sin^2\theta_v}{2}\right]. \tag{25}$$

The interference terms between amplitudes with different $\lambda$ vanish under integration over $\phi_l - \phi_v$. As in $\mathcal{R}(D^{(*)})$, theory uncertainties in $|V_{cb}|$ are factored out of $F_{L,l}$. Some recent and new SM predictions for $F_{L,\tau}(D^*)$ are provided in Table II using a variety of theoretical inputs. We also include a SM prediction for $F_{L,\ell}(D^*)$.

A similar analysis may be applied to $\tau \to h\nu$ decay amplitudes within $B \to D^{(*)}(\tau \to h\nu)\bar{\nu}$. For example, in the helicity basis for the $\tau$, the $\tau \to \pi\nu$ amplitudes are the $j = 1/2$ Wigner-$D$ functions $e^{i\phi_h/2}\sin(\theta_h/2)$ or $e^{-i\phi_h i/2}\cos(\theta_h/2)$ for $\lambda_\tau = \mp$, respectively, where the helicity angles $\theta_h$ and $\phi_h$ are as defined in Fig. 1. The $\tau$ polarization

$$P_\tau(D^{(*)}) = \frac{(\Gamma_{\lambda_\tau=+} - \Gamma_{\lambda_\tau=-})[B \to D^{(*)}\tau\nu]}{\Gamma[B \to D^{(*)}\tau\nu]} \tag{26}$$

is a physical quantity in $B \to D^{(*)}(\tau \to \pi\nu)\bar{\nu}$ decays via the marginal differential rate

$$\frac{1}{\Gamma}\frac{d\Gamma_{B\to D^{(*)}(\tau\to\pi\nu)\bar{\nu}}}{d\cos\theta_h} = \frac{1}{2}[1 + P_\tau(D^{(*)})\cos\theta_h]. \tag{27}$$

The interference terms between amplitudes with different $\lambda_\tau$ vanish under integration over $\phi_\tau - \phi_h$. This generalizes to other final states such as $h = \rho, 3\pi$ as

$$\frac{1}{\Gamma}\frac{d\Gamma_{B\to D^{(*)}(\tau\to h\nu)\bar{\nu}}}{d\cos\theta_h} = \frac{1}{2}[1 + \alpha_h P_\tau(D^{(*)})\cos\theta_h], \tag{28}$$

in which $\alpha_h$ is the analyzing power that depends on the final state $h$. In particular, the pion is a perfect polarizer $\alpha_\pi = 1$, while $\alpha_\rho = (1 - 2m_\rho^2/m_\tau^2)/(1 + 2m_\rho^2/m_\tau^2)$. Just as for $F_{L,\tau}(D^*)$, some recent and new SM predictions for $P_\tau(D^{(*)})$ are provided in Table II using a variety of potentially differing theoretical inputs. The missing energy in the $\tau$ decay means that $\theta_h$ is reconstructible only up to twofold ambiguities in present experimental frameworks.

### E. Excited and other states

Thus far we have discussed mainly the ground-state meson transitions $B \to D^{(*)} l\nu$. However, much of the previous discussion can be extended to excited charm states, baryons, charm-strange hadrons, and double-heavy hadrons. Several of these processes exhibit fewer HQ symmetry constraints or greater theoretical cleanliness than the ground states. This may be exploited to gain higher sensitivity to NP effects or better insight or control over theoretical uncertainties such as $1/m_c^2$ contributions.

Four orbitally excited charm mesons, collectively labeled as the $D^{**}$, comprise in spectroscopic notation the states $D_0^* \sim {}^3P_0$, $D_1' \sim {}^3P_1$, $D_2^* \sim {}^3P_2$, and the $D_1 \sim {}^1P_1$.[5] In the language of HQ symmetry, the $D_0^*$ and $D_1'$ ($D_1$ and $D_2^*$) furnish a heavy-quark doublet whose dynamics is described by the $s_\ell^P = 1/2^+$ ($s_\ell^P = 3/2^+$) HQET. The $1/2^+$ doublet is quite broad, with widths ∼0.2 and 0.4 GeV, while the $3/2^+$ states are an order of magnitude narrower. The $B \to D^{**} l\nu$ decays produce important feed-down backgrounds to $B \to D^{(*)} l\nu$; see Secs. IV and V.C.

Several of the $B \to D^{**}$ form factors vanish at leading order in the heavy-quark limit at zero recoil, so the higher-order $\mathcal{O}(1/m_{c,b})$ corrections become important, as included in the Leibovich-Ligeti-Stewart-Wise (LLSW) parametrization

[4]Another common notation is $F_{L,\tau}(D^*) = F_L^{D^*}$.

[5]The $D_1'$ is also often denoted by $D_1^*$.

TABLE II. SM predictions for the $D^*$ longitudinal fraction and the $\tau$ polarization in $B \to D^{(*)}$. We also show simple arithmetic averages of the predictions and uncertainties. The CLN-based predictions shown in the bottom row are not included in the arithmetic average.

| Inputs | $F_{L,\tau}(D^*)$ | $F_{L,\ell}(D^*)$ | $P_\tau(D^*)$ | $P_\tau(D)$ |
|---|---|---|---|---|
| BLPR, $\sim 1/m_c^2$, LCSR[a] | 0.441(6) | ⋯ | −0.508(4) | 0.325(3) |
| BGL, BLPR, $\sim 1/m_c^2$, LCSR[b] | 0.464(10) | ⋯ | −0.496(15) | 0.321(3) |
| BGL, BLPR, $\sim 1/m_c^2$ [c] | 0.469(10) | ⋯ | −0.492(25) | ⋯ |
| BLPR[d] | 0.455(3) | 0.517(5) | −0.504(4) | 0.323(2) |
| Arithmetic averages | 0.455(6) | 0.517(5) | −0.501(11) | 0.324(3) |
| CLN[e] | 0.46(4) | ⋯ | ⋯ | ⋯ |

[a]Per Huang *et al.* (2018) using the fit of Jung and Straub (2019).
[b]Per Bordone, Jung, and Dyk (2020) with Belle 2019 data (Waheed *et al.*, 2019).
[c]Per Jaiswal, Nandi, and Patra (2020) with Belle 2019 data (Waheed *et al.*, 2019).
[d]Using the fit of Bernlochner *et al.* (2017). The correlation between $P_\tau(D^*)$ and $P_\tau(D)$ is $\rho = 0.33$.
[e]See Alok *et al.* (2017).

(Leibovich *et al.*, 1997, 1998). This can lead to higher sensitivities to various NP currents compared to the ground states (Biancofiore, Colangelo, and Fazio, 2013; Bernlochner, Ligeti, and Robinson, 2018). These decays must therefore be incorporated consistently, especially for LFUV analyses with NP contributions. The current SM predictions for all four modes from fits to Belle data including higher-order HQET contributions at $\mathcal{O}(\alpha_s, 1/m_{c,b})$ are (Bernlochner and Ligeti, 2017; Bernlochner, Ligeti, and Robinson, 2018)

$$\mathcal{R}(D_0^*) = 0.08(3), \qquad \mathcal{R}(D_1') = 0.05(2),$$
$$\mathcal{R}(D_1) = 0.10(2), \qquad \mathcal{R}(D_2^*) = 0.07(1). \tag{29}$$

These are smaller than $\mathcal{R}(D^{(*)})$ because of the smaller phase space and reduced $w$ range. An additional useful quantity is the ratio for the sum of the four $D^{**}$ states (Bernlochner and Ligeti, 2017; Bernlochner, Ligeti, and Robinson, 2018),

$$\mathcal{R}(D^{**}) = \frac{\sum_{X\in D^{**}}\Gamma[B \to X\tau\bar{\nu}]}{\sum_{X\in D^{**}}\Gamma[B \to X\ell\bar{\nu}]} = 0.08(1), \tag{30}$$

taking into account correlations in the SM predictions.

An identical discussion proceeds for $B_s \to D_s^{(*,**)} l\nu$ decays, with the light spectator quark replaced by a strange quark. The typical size of flavor SU(3) breaking, seen in, e.g., $f_K/f_\pi$, suggests ∼20% corrections relative to the predictions for $B \to D^{(*,**)}$. Lattice studies are available for $B_s \to D_s$ (McLean *et al.*, 2020) beyond zero recoil as are preliminary results for $B_s \to D_s^*$ (Harrison and Davies, 2021), with the respective predictions

$$\mathcal{R}(D_s) = 0.2987(46), \qquad \mathcal{R}(D_s^*) = 0.2442(79)(35), \tag{31}$$

and there is some evidence of relative insensitivity of the matrix elements to the light spectator quark (McLean *et al.*, 2019), despite the expectations from SU(3) breaking. A recent analysis for $B_{(s)} \to D_{(s)}^{(*)}$ (Bordone *et al.*, 2020) combines model-dependent QCDSR inputs with LCSR inputs extrapolated from beyond the physical recoil limit. This analysis predicts

$$\mathcal{R}(D) = 0.298(3), \qquad \mathcal{R}(D_s) = 0.297(3),$$
$$\mathcal{R}(D^*) = 0.250(3), \qquad \mathcal{R}(D_s^*) = 0.247(8). \tag{32}$$

The resulting $\mathcal{R}(D^*)$ prediction agrees with the prior predictions in Table I at the $1\sigma - 2\sigma$ level. At the LHC and at the $Z$ peak, non-negligible feed-downs to $\mathcal{R}(D^*)$ arise from $B_s \to D_{s1}'\tau\nu$ decays because of their subsequent decay to $D^{(*)}\tau\nu X$, which must be taken into account. Likewise $B_s \to D_{s2}^*\tau\nu$ decays may feed down to $\mathcal{R}(D)$: see Sec. IV.C.

The light degrees of freedom in the ground-state baryons $\Lambda_{b,c}$ have spin-parity $s_\ell^P = 0^+$, which corresponds to the simplest, and therefore most constrained, HQET. In particular, the $\Lambda_b \to \Lambda_c$ form factors receive hadronic corrections to the leading-order IW function only at $1/m_{c,b}^2$. Beyond zero recoil lattice data are available for both SM and NP form factors (Detmold, Lehner, and Meinel, 2015). Predictions for $\Lambda_b \to \Lambda_c\tau\nu$, however, are at present more precise when LQCD results are combined with data-driven fits for $\Lambda_b \to \Lambda_c\ell\nu$ plus HQET relations. In particular, a data-driven HQET-based form factor parametrization, when combined with the lattice data, provides the currently most precise prediction (Bernlochner *et al.*, 2018)

$$\mathcal{R}(\Lambda_c) = 0.324(4), \tag{33}$$

as well as the ability to directly extract or constrain the $1/m_c^2$ corrections. The latter are found to be consistent with HQ symmetry power counting expectations. Similar techniques will be applicable to the two $\Lambda_c^*$ excited states with $s_\ell^P = 1^-$ (Leibovich and Stewart, 1998; Böer *et al.*, 2018) once data are available. At present, predictions for $\mathcal{R}(\Lambda_c^*)$ may be derived using a constituent quark model approach (Pervin, Roberts, and Capstick, 2005) similar to ISGW2, yielding $\mathcal{R}(\Lambda_c^*(2595)) \simeq 0.16$ and $\mathcal{R}(\Lambda_c^*(2625)) \simeq 0.11$.

Finally, the semileptonic decay $B_c \to J/\psi(\to\ell\ell)l\nu$ provides an extremely clean signature to test LFUV. The aforementioned HQ symmetry arguments, however, cannot be applied to double-heavy quark mesons such as $B_c$ and $J/\psi$ (or the pseudoscalar $\eta_c$): They cannot be thought of as a single heavy quark dressed by brown muck. Rather, large kinetic energy terms break the heavy-quark flavor symmetry, leaving an approximate residual heavy-quark spin symmetry

(Jenkins *et al.*, 1993). Hence, a HQET description is not used for these modes. A variety of quark-model-based analyses and predictions have been conducted, with wide-ranging predictions for $\mathcal{R}(J/\psi) \sim 0.2$–$0.4$. A recent model-independent combined analysis for $B_{(s)} \to D^{(*)}{}_{(s)}$ and $B_c \to J/\psi$ and $\eta_c$, which made use of a combination of dispersive bounds, lattice results, and HQET where applicable, provided a prediction $\mathcal{R}(J/\psi) = 0.25(3)$ (Cohen, Lamm, and Lebed, 2019). A subsequent LQCD result provided the following high-precision prediction (Harrison, Davies, and Lytle, 2020b):

$$\mathcal{R}(J/\psi) = 0.2582(38). \tag{34}$$

Preliminary lattice results for the $B_c \to \eta_c$ form factors beyond zero recoil are also available (Colquhoun *et al.*, 2016).

### F. $b \to u l \nu$ processes

The dispersive analysis used in Sec. II.C.1 to parametrize the form factors for $B \to D^{(*)}$ may also be employed for the light hadron $b \to u l \nu$ processes. For $B \to \pi l \nu$, in particular, significant simplifications arise because there is only a single possible subthreshold resonance (the $B^*$) for the $f_+$ form factor, and no subthreshold resonance for $f_0$. Combining this with general analyticity properties of the $B \to \pi$ matrix element leads to the Bourrely-Caprini-Lellouch parametrization (Bourrely, Caprini, and Lellouch, 2009). Expanding in $z = z(q^2, q^2_{\rm opt})$, one obtains

$$f_+(q^2) = \frac{1}{1 - q^2/m^2_{B^*}} \sum_{j=0}^{N} b_j^+ \left[ z^j - (-1)^{j-N} \frac{j}{N} z^N \right],$$
$$f_0(q^2) = \sum_{j=0}^{N} b_j^0 z^j, \tag{35}$$

where $N$ is the truncation order. Lattice results beyond zero recoil are available for all $B \to \pi$ form factors (Bailey *et al.*, 2015a, 2015b) and can be incorporated into global fits to available experimental data. The SM prediction is (Bernlochner, 2015)

$$\mathcal{R}(\pi) = 0.641(16). \tag{36}$$

Higher-twist LCSR results are available for the $B \to \rho$ and $B \to \omega$ SM and NP form factors, in which they are parametrized by the optimized $z = z(q^2, q^2_{\rm opt})$ expansion (Bharucha, Straub, and Zwicky, 2016). These results may be applied to obtain a correlated, beyond zero recoil fit between the SM and NP form factors and the measured $q^2$ spectra of the corresponding light-lepton modes. The SM predictions from this fit are (Bernlochner, Prim, and Robinson, 2021)

$$\mathcal{R}(\rho) = 0.535(9), \qquad \mathcal{R}(\omega) = 0.543(15). \tag{37}$$

Quark model approaches have also been applied to the double-heavy to heavy-light decays $B_c \to D^{(*)} l \nu$ [see Ivanov, Körner, and Santorelli (2006) and Leljak and Melic (2020)]; lattice results are anticipated soon for these decays.

### G. Inclusive processes

The inclusive process $B \to X_c l \nu$, where $X_c$ is a single-charm (multi)hadron final state of any invariant mass, admits a different, cleaner theoretical description than the exclusive processes. For instance, in the limit $m_b \to \infty$ the inclusive process is described simply by the underlying $b \to c l \nu$ free quark decay, rather than in terms of an unknown Isgur-Wise function.

The square of the inclusive matrix element $|\langle X_c | J | \bar{B} \rangle|^2$ can be reexpressed in terms of the time-ordered forward matrix element $\langle \bar{B} | T(J^\dagger J) | \bar{B} \rangle$. The latter can be computed via an OPE order by order in $1/m_b$ and $\alpha_s$, yielding theoretically clean predictions. State-of-the-art predictions include $1/m_b^2$ terms (Ligeti and Tackmann, 2014) and two-loop QCD corrections (Biswas and Melnikov, 2010), which may be combined to generate the precision prediction (Freytsis, Ligeti, and Ruderman, 2015)

$$\mathcal{R}(X_c) = 0.223(4), \tag{38}$$

as well as precision predictions for the dilepton invariant mass and lepton energy distributions. Because the theoretical uncertainties in $B \to X_c l \nu$ are of a different origin than the exclusive modes, the measurement of $B \to X_c \tau \nu$ would provide a hadronic-model-independent cross-check of lepton flavor universality; see Sec. VI.C. The inclusive baryonic decays $\Lambda_b \to X_c l \nu$ may be similarly considered; see Balk, Korner, and Pirjol (1998) and Colangelo, Fazio, and Loparco (2020).

### H. New physics operators

NP may enter the $b \to c \tau \nu$ processes via a heavy mediator such that the semileptonic decay is generated by four-Fermi operators of the form

$$\mathcal{O}_{XY} = \frac{c_{XY}}{\Lambda^2_{\rm eff}} (\bar{c} \Gamma_X b)(\bar{\tau} \Gamma_Y \nu_\tau), \tag{39}$$

where $\Gamma_{X(Y)}$ is any Dirac matrix with $X$ ($Y$) labeling the chiral structure of the quark (lepton) current and $c_{XY}$ is a Wilson coefficient defined at scale $\mu \sim m_{c,b}$. The Wilson coefficient is normalized against the SM such that $\Lambda_{\rm eff} = (2\sqrt{2} G_F V_{cb})^{-1/2} \simeq 870$ GeV. If we denote by $M$ the characteristic scale of an ultraviolet (UV) completion that matches onto the effective NP operators in Eq. (39), then order 10%–20% variations in $\mathcal{R}(D^{(*)})$ or other observables from SM predictions typically probe $M \sim \Lambda_{\rm eff}/\sqrt{c_{XY}} \sim$ a few TeV. This is tantalizingly within reach of direct collider measurements and near the natural scale for UV completions of electroweak dynamics.

A common basis choice for $\Gamma_X$ is the set of chiral scalar, vector, and tensor currents: $P_{R,L}$, $\gamma^\mu P_{R,L}$, and $\sigma^{\mu\nu} P_{R,L}$, respectively. Assuming only SM left-handed neutrinos, the lepton current is always left-handed, and the tensor current may only be left-handed. It is common to write the five remaining Wilson coefficients as $c_{XY} = c_{SR}, c_{SL}, c_{VR}, c_{VL}$, and $c_T$. We use this notation for the Wilson coefficients hereafter. As for the SM, the NP leptonic amplitude still takes

the form $D^j_{m1,m2}(\theta_l,\phi_l)$, with $j=0$ or 1, and $|m_{1,2}|\leq j$, and the structure of the differential decay rate resembles Eq. (9), but with additional dependencies on NP Wilson coefficients, $w$, and $r$.

The (pseudo)scalar and tensor operators run under the renormalization group (RG) evolution of QCD, while the vector and axial vector operators correspond to conserved currents and do not [for this reason the normalization of Eq. (3) is well defined]. At one-loop order in the leading-log approximation, the running of $c_{SR,SL,T}$ is dominated by contributions below the top quark mass $m_t$ and only weakly affected by variations in $M\sim\Lambda_{\rm eff}$. Electroweak interactions, however, may induce mixing between $c_{SR,SL,T}$ that can become non-negligible for RG evolution above the weak scale (González-Alonso, Camalich, and Mimouni, 2017). RG evolution from $M\simeq\Lambda_{\rm eff}>m_t$ to $\mu\simeq\sqrt{m_c m_b}$ generates at leading-log order

$$c_{SR,SL}(\mu)/c_{SR,SL}(M)\simeq 1.7,\qquad c_T(\mu)/c_T(M)\simeq 0.84. \quad (40)$$

These running effects are particularly important in translating the low scale effective field theory (EFT) implications of $b\to c\tau\nu$ measurements to collider measurements at high scales.

#### I. Connection to other processes

LFUV in $b\to cl\nu$ necessarily implies violation in the crossed process $B_c\to l\nu$. The latter decays are extremely theoretically clean: Their tauonic versus leptonic LFUV ratios are simply the ratios of chiral suppression and two-body phase-space factors, i.e., $m_\tau^2(1-r_\tau^2)^2/m_\ell^2(1-r_\ell^2)^2$, in which $r_l=m_l/m_{B_c}$. These ratios are precisely known.

In the SM, the branching ratio

$$\mathcal{B}[B_c\to l\nu]=\tau_{B_c}G_F^2|V_{cb}|^2 m_{B_c}^3 f_{B_c}^2 r_l^2(1-r_l^2)^2/8\pi, \quad (41)$$

in which the decay constant $f_{B_c}\simeq 0.434(15)$ GeV from lattice data (Colquhoun *et al.*, 2015) and the $B_c$ lifetime $\tau_{B_c}=0.510(9)\times 10^{-12}$ s is well measured (Zyla *et al.*, 2020). In particular, in the SM one predicts $\mathcal{B}[B_c\to\tau\nu]\simeq 2.2(2)\%\times(|V_{cb}|/0.04)^2$.

In the presence of NP, the NP Wilson coefficients generate an additional factor

$$\mathcal{B}[B_c\to\tau\nu]=\mathcal{B}_{\rm SM}\left|1+c_{VL}-c_{VR}+\frac{m_{B_c}^2(c_{SR}-c_{SL})}{m_\tau(\bar m_b+\bar m_c)}\right|^2, \quad (42)$$

where $\bar m_{c,b}$ are quark masses in the rescaled minimal subtraction ($\overline{\rm MS}$) renormalization scheme at scale $\mu$ entering via equations of motion. Because the NP pseudoscalar current induces a chiral flip, there is no chiral suppression in the pseudoscalar term. As a result this term is enhanced by a factor of $m_{B_c}/m_\tau\sim 3.5$ versus the $V-A$ current contribution. This leads to large tauonic branching ratio enhancements that may then be in tension with naive expectations that the $B_c$ hadronic branching ratios ~70%–90% (Li, Yang, and Zhang, 2016; Akeroyd and Chen, 2017; Alonso, Grinstein, and Camalich, 2017; Bardhan and Ghosh, 2019). A corollary is that a future measurement or bounds of $\mathcal{B}[B_c\to\tau\nu]$ alone would tightly constrain the NP pseudoscalar contributions.

In the absence of any NP below the electroweak scale, the NP effective operators in Eq. (39) must match onto an electroweak-consistent EFT constructed from SM quark and lepton doublets and singlets under $\mathrm{SU}(2)_L\times\mathrm{U}(1)_Y$. In particular, because the SM neutrino belongs to an electroweak lepton doublet $L_L$, electroweak symmetry requires the presence of at least two electroweak doublets in any operator that generates the $b\to c\tau\nu$ decay. (An exception applies if right-handed sterile neutrinos are present.) In any given NP scenario, this may generate relations between $b\to c\tau\nu$ and other processes that arise when at least one of the four fermions is replaced by its electroweak partner. For example, various minimal NP models, depending on their flavor structure, may be subject to tight bounds from the rare $b\to s\nu\nu$ or $b\to s\tau\tau$ decays or bounds on $Z\to\tau\tau$ or $W\to\tau\nu$ branching ratios (Sakaki *et al.*, 2013; Freytsis, Ligeti, and Ruderman, 2015), or the high-$p_T$ scattering $pp\to b\tau\nu$ (Altmannshofer, Bhupal Dev, and Soni, 2017) and $pp\to\tau\tau$ or $\tau\nu$ (Greljo and Marzocca, 2017; Greljo, Camalich, and Ruiz-Álvarez, 2019). Ultraviolet completions with nontrivial flavor structures may further generate relations to charm decay processes or $b\to s\ell\ell$. The latter is particularly intriguing, because of an indication for light-lepton universality violation in the ratios (Aaij *et al.*, 2017c, 2019c)

$$\mathcal{R}_{K^{(*)}}\equiv\frac{\Gamma[B\to K^{(*)}\mu\mu]}{\Gamma[B\to K^{(*)}ee]}, \quad (43)$$

at the $2\sigma$ to $3\sigma$ level in each mode; see Sec. VI.E. Extensive literature has considered possible common origins of LFUV in semitauonic processes with LFUV in these rare decays. See Bhattacharya *et al.* (2015), Calibbi, Crivellin, and Ota (2015), Buttazzo *et al.* (2017), and Kumar, London, and Watanabe (2019), among many others, for extensive discussions of combined explanations for semileptonic and rare decay LFUV anomalies.

## III. EXPERIMENTAL METHODS

### A. Production and detection of *b* hadrons

Since the discovery of the $b$ quark in 1977 (Herb *et al.*, 1977), large samples of $b$ hadrons have been produced at colliders such as CESR, LEP, and Tevatron. However, it was not until the advent of the $B$ factories and the LHC, with their even larger samples and specialized detectors, that the study of third generation LFUV in $B$ mesons became feasible. This is because of the stringent analysis selections that are required to achieve adequate signal purity when reconstructing final states that include multiple unreconstructed neutrinos. The $B$ factories (Bevan *et al.*, 2014), KEKB in Japan and PEP-II in the United States, took data from 1999 to 2010. Their detectors, Belle (Abashian *et al.*, 2002) and *BABAR* (Aubert *et al.*, 2013), recorded more than a billion $B\bar B$ events originating from clean $e^+e^-$ collisions. The LHCb detector (Augusto Alves *et al.*, 2008; Aaij *et al.*, 2015a) at the CERN LHC, which started taking data in 2010, had recorded an unprecedented trillion $b\bar b$ pairs as of 2020, which allowed it to

TABLE III. Approximate number of $b$ hadrons produced and expected at the $B$ factories (Bevan *et al.*, 2014; Altmannshofer *et al.*, 2019) and at the LHCb experiment (Albrecht *et al.*, 2019), including some of the latest developments (Béjar Alonso *et al.*, 2020). The LHCb numbers take into account an average geometrical acceptance of about 15%. Note that the overall $B$ reconstruction efficiencies at LHCb are usually significantly lower than those at the $B$ factories (see text). The two values of integrated luminosities and center-of-mass energies shown for Belle and Belle II correspond to data taking at the $\Upsilon(4S)$ and $\Upsilon(5S)$ resonances, respectively. The $B$-factory experiments also recorded datasets at lower center-of-mass energies (below the open beauty threshold) that are not included in this table.

| | | | | LHCb | | | |
|---|---|---|---|---|---|---|---|
| Experiment | *BABAR* | Belle | Belle II | Run 1 | Run 2 | Runs 3 + 4 | Runs 5 + 6 |
| Completion date | 2008 | 2010 | 2031 | 2012 | 2018 | 2031 | 2041 |
| Center-of-mass energy | 10.58 GeV | 10.58/10.87 GeV | 10.58/10.87 GeV | 7/8 TeV | 13 TeV | 14 TeV | 14 TeV |
| $b\bar{b}$ cross section (nb) | 1.05 | 1.05/0.34 | 1.05/0.34 | $(3.0/3.4)\times 10^5$ | $5.6\times 10^5$ | $6.0\times 10^5$ | $6.0\times 10^5$ |
| Integrated luminosity ($\text{fb}^{-1}$) | 424 | 711/121 | $(40/4)\times 10^3$ | 3 | 6 | 40 | 300 |
| $B^0$ mesons ($10^9$) | 0.47 | 0.77 | 40 | 100 | 350 | 2500 | 19 000 |
| $B^+$ mesons ($10^9$) | 0.47 | 0.77 | 40 | 100 | 350 | 2500 | 19 000 |
| $B_s$ mesons ($10^9$) | ⋯ | 0.01 | 0.5 | 24 | 84 | 610 | 4600 |
| $\Lambda_b$ baryons ($10^9$) | ⋯ | ⋯ | ⋯ | 51 | 180 | 1300 | 9800 |
| $B_c$ mesons ($10^9$) | ⋯ | ⋯ | ⋯ | 0.8 | 4.4 | 19 | 150 |

compensate for the more challenging environment of $pp$ collisions. The recently commissioned Belle II experiment and the LHCb detector, to be upgraded in 2019–2021 and 2031, are expected to continue taking data over the next decade and a half, surpassing the current data samples by more than an order of magnitude. In the following, we describe how $b$ hadrons are produced and detected at these facilities.[6] Table III summarizes the number of $b$ hadrons produced and expected at the $B$ factories and at the LHCb experiment.

### 1. The *B* factories

KEKB and PEP-II produced $B$ mesons by colliding electron and positron beams at a center-of-mass energy of 10.579 GeV. At this energy, $e^+$ and $e^-$ annihilation produces $\Upsilon(4s)$ mesons in about 24% of the hadronic collision processes, with the production of $c\bar{c}$ and other light-quark pairs accounting for the remaining 76%. Together with other processes producing pairs of fermions, the latter form the so-called continuum background.

The $\Upsilon(4s)$ meson is a $b\bar{b}$ bound state that, as a result of having a mass only about 20 MeV above the $B\bar{B}$ production threshold, decays almost exclusively to $B^+B^-$ or $B^0\bar{B}^0$ pairs. Some limited running away from the $\Upsilon(4s)$ resonance was performed in order to study the continuum background and the properties of the bottomonium resonances $\Upsilon(1s)-\Upsilon(5s)$. The largest dataset produced by KEKB was used to study $B_s$ mesons obtained from $\Upsilon(5s)$ decays. However, the resulting $B_s^{(*)}\bar{B}_s^{(*)}$ data sample was small, about 3% of the total $B\bar{B}$ sample, as shown in Table III.

On the one hand, compared to hadron colliders, the $b\bar{b}$ production cross section in lepton colliders such as the $B$ factories is much smaller: even at the thus far highest instantaneous luminosity of $2.4\times 10^{34}\ \text{cm}^{-2}\,\text{s}^{-1}$ achieved by SuperKEKB in the summer of 2020, $B\bar{B}$ pairs were produced at a rate of only about 25 Hz. On the other hand, one of the significant advantages of colliding fundamental particles like electrons and positrons is that the initial state is fully known; i.e., nearly 100% of the $e^+e^-$ energy is transferred to the $B\bar{B}$ pair. This feature can be exploited by tagging techniques (Sec. III.C.1) that reconstruct the full collision event and can determine the momenta of missing particles such as neutrinos so long as the detectors are capable of reliably reconstructing all of the visible particles. The *BABAR* and Belle detectors managed to cover close to 90% of the total solid angle by placing a series of cylindrical subdetectors around the interaction point and complementing them by end caps that reconstructed the particles that were ejected almost parallel to the beam pipe. This is sketched in Fig. 2.

The specific technologies employed in both $B$-factory detectors were described in detail by Bevan *et al.* (2014). Four or five layers of precision silicon sensors placed close to the interaction point reconstruct the decay vertices of long-lived particles, as well as the first ≈10 cm of the tracks left by charged particles. The trajectories and ionization energy loss are measured by 40–50 layers of low-material drift chambers as a function of distance ($dE/dx$) of charged particles. Time-of-flight and Cherenkov systems provide particle identification (PID) that allow kaon and pion discrimination. Crystal calorimeters measure the electromagnetic showers created by electrons and photons. A solenoid magnet generates the 1.5 T magnetic field parallel to the beam pipe that bends the trajectories of charged particles to allow for determination of their momenta. A series of steel layers instrumented with muon chambers guide the return of the magnetic flux and provide muon and $K_L^0$ PID.

Between 1998 and 2008–2010, the *BABAR* and Belle detectors recorded a total of 4.71 and $7.72\times 10^8$ $B\bar{B}$ pairs, respectively. These large samples, which are still being analyzed, allowed for the first measurement of $CP$ violation in the $B$ system, the observation of $B$ mixing, and many other novel results (Bevan *et al.*, 2014). These further included the first observations of $B\to D^{(*)}\tau\nu$ decays (see Sec. IV), which

[6]Other current experiments might also be able to make contributions to semitauonic LFUV measurements in the future. For instance, the CMS experiment at the LHC recorded in 2018 a large parked sample of unbiased $b$-hadron decays, with the primary goal of measuring the $\mathcal{R}_{K^{(*)}}$ ratios. This sample could conceivably also be used to measure semitauonic decays if, e.g., the challenges arising from the multiple neutrinos in the final state can be overcome.

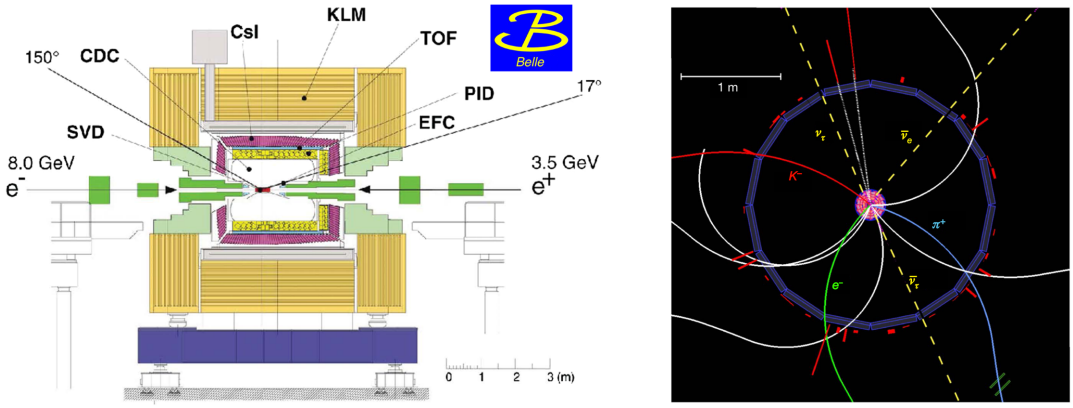


FIG. 2. Left panel: side view of the Belle detector. See Abashian *et al.* (2002) for further details on the subdetectors and their acronyms. The *BABAR* detector has a similar configuration. Right panel: view perpendicular to the beam axis. The displayed event is reconstructed as a $\Upsilon(4S) \to B^+B^-$ candidate, with $B^- \to D^0\tau^-\bar{\nu}_\tau$, $D^0 \to K^-\pi^+$, and $\tau^- \to e^-\nu_\tau\bar{\nu}_e$, and the $B^+$ decaying to five charged particles (white solid lines) and two photons. The directions of undetected neutrinos are indicated as dashed lines. From Abashian *et al.*, 2002, and Ciezarek *et al.*, 2017.

in turn began the study of third generation LFUV, the focus of this review. The success of the $B$ factories has led to the upgrade of the accelerator facilities at KEKB, so-called SuperKEKB (Akai, Furukawa, and Koiso, 2018), such that it will be capable of delivering instantaneous luminosities 30 times higher than before. The upgraded Belle detector, Belle II (Abe *et al.*, 2010), started taking data in 2018 with the aim of recording a total of more than 40 billion $B\bar{B}$ pairs. The LFUV prospects for Belle II are discussed in Sec. VII.A.2.

### 2. The LHCb experiment

At hadron colliders such as the LHC, $b$ quarks are predominantly pair produced in $pp$ collisions via the gluon fusion process $gg \to b\bar{b}$ plus subleading quark fusion contributions, with an approximate production cross section $\sigma(b\bar{b}) \sim 560\ \mu$b at $\sqrt{s} = 13$ TeV, scaling approximately linearly in $\sqrt{s}$ (Aaij *et al.*, 2017a). Electroweak production cross sections for single $b$ quarks or pairs of $b$ quarks via Drell-Yan processes or Higgs or top quark decays are 5 or more orders of magnitude smaller, with the largest such cross section $\sigma(Z \to b\bar{b}) \sim 10$ nb. As a result, $b$ quarks are effectively always accompanied in LHC collisions by a companion $\bar{b}$ quark. This feature is extremely important for unbiased trigger strategies enabling the study of one $b$-hadron decay while triggering on the other.

At leading order, the hadronization of a $b$ quark at the LHC is similar to the one observed in detail by the LEP experiments. For instance, the momentum distribution of the non-$b$-hadron fragments, which is relevant for same-side tagging studies, is well described by LEP-inspired Monte Carlo (MC) simulations (Sjöstrand *et al.*, 2015). More important is the relative production of the various $b$-hadron species: the main features (dominant production of $B^0$ and $B^+$ mesons and a sizable production fraction of $B_s$ and $\Lambda_b$) are the same, except that a much larger $\Lambda_b$ production fraction is observed for $p_T$ (momentum transverse to the beam axis) below 10 GeV (Aaij *et al.*, 2019a). LHCb can also study the decays of $B_c$ mesons, in spite of its low production rate, approximately 0.6% of the $B^+$ production cross section (Aaij *et al.*, 2015b). As discussed in Secs. II.E and II.I, $B_c$ mesons provide an interesting laboratory for testing LFUV in $B_c \to J/\psi\tau\nu$ or $B_c \to \tau\nu$ decays.

The parton center-of-mass energy required to produce a $b$-hadron pair at threshold is far smaller than the total available collision energy in the $pp$ system, leading to the production of a significant fraction of $b\bar{b}$ pairs with large forward or backward boosts. This characteristic is the basis of the LHCb experimental concept (Augusto Alves *et al.*, 2008; Aaij *et al.*, 2015a), which studies the $b\bar{b}$ pairs produced within a 400 mrad cone covering the forward region, corresponding to a pseudorapidity $2 \leq \eta \leq 5$. Despite this small solid angle, the LHCb detector captures ∼15% of the full $b\bar{b}$ cross section (Aaij *et al.*, 2018b).

Within this acceptance, the $b$ hadrons have a typical transverse momentum $p_T$ of 10 GeV, which corresponds to an overall energy of ∼200 GeV. This in turn corresponds to a typical boost factor of about 50, resulting in a mean flight distance of over 2 cm for each electroweakly decaying ground-state $b$ hadron: namely, $B^{0,+}$, $B_s$, $B_c$, or $\Lambda_b$. The sophisticated silicon trackers used in the LHCb detector provide a typical position resolution of 300 $\mu$m for the $B$ vertex along its flight direction, which results in flight distance significances between the $b$-hadron decay vertex and its primary vertex (PV) of over $100\sigma$. This precision leads to extremely clean signals even for high-multiplicity decay channels where the combinatorial background is potentially important (Aaij *et al.*, 2018b), provided that the primary production vertex can be identified.

The LHCb luminosity was kept low enough (Aaij *et al.*, 2015a) that the mean number of primary vertices per event until 2018 was between 1 and 2. This number is expected to rise to about 5 after the 2019–2021 upgrade (Bediaga *et al.*, 2012), and possibly to 50 after the 2031 upgrade (Aaij *et al.*, 2017b). The longitudinal size of the LHCb luminous region is 20 cm, so, with only a handful of $pp$ interactions in a given event, the primary vertex misconstruction is kept to a low level. The ATLAS and CMS experiments typically

accumulate 50 primary vertices in a given event (rising to 200 after 2027) and therefore face a different challenge. Nevertheless, they are capable of cleanly reconstructing low-multiplicity *b*-hadron decays thanks to their large coverage and high-granularity subdetectors. It should be stressed, however, that for semitauonic *b*-hadron decays the goal is not to simply isolate a decay vertex from a primary vertex, but rather to identify a chain of vertices comprising the PV, the *b*-hadron decay, and, in the case of hadronic-$\tau$ measurements, the $\tau$ decay. At the LHC, this is currently feasible only at LHCb.

As is the case in the *B* factories, PID capabilities are critical to properly identify *b*-hadron decays. For instance, at a hadron collider, misidentifying a pion as a kaon could lead to confusing a $B_s$ meson for a $B^0$ meson, and identifying a pion as a proton could lead to a $\Lambda_b$ baryon impersonating a $B^0$ meson. PID information is provided by the two ring imaging Cherenkov (RICH) detectors shown in the left panel of Fig. 3.

Table III lists the known production rates for all ground-state *b*-hadron species at both LHCb and the *B* factories. While the geometrical acceptance is included for the LHCb values, the average trigger and analysis requirements must be taken into account as well in order to compare LHCb with the *B* factories. These requirements limit the LHCb useful yield at LHCb to about 0.1% or less of the available sample. As an example, for their respective measurements of $\mathcal{R}_{K^+}$, LHCb (Aaij *et al.*, 2021) and Belle (Choudhury *et al.*, 2021) reconstructed 3850 and 42.3 $B^+ \to K^+\mu^+\mu^-$ signal candidates. These correspond to $8.6 \times 10^{-9}$ and $54.9 \times 10^{-9}$ candidates per $B^+$ meson in Table III, respectively, which translates to an overall signal reconstruction efficiency for this particular decay that is about 6 times lower for LHCb than for Belle.

Another feature of LHCb physics is the large production rate of excited *b*-hadron states: $B^{**}$, $B_s^{**}$, and $\Lambda_b^{**}$ can be studied in detail, as can baryons containing both *b* and *s* quarks, such as $\Xi_b$, $\Omega_b$, and their excited states. These can be useful to study semitauonic decays because, as described in Sec. III.C.3, the decay $B_{s2}^{**}2 \to BK$ can provide access to kinematic variables in the *B* center-of-mass frame via *B* tagging.

### B. Particle reconstruction

Ground-state *b* hadrons (i.e., hadrons decaying only through flavor-changing electroweak currents) have lifetimes of the order of 1 ps. Thus, they decay fast enough that they must all be reconstructed from their more stable decay products. At the same time, they live and fly long enough that their decay vertices can be separated from the vertex of the primary collision ($e^+e^-$ in the case of the *B* factories and $pp$ in the case of LHCb). The reconstruction of these stable decay products proceeds in a similar fashion for the *B* factories and the LHCb experiment, with some key differences.

#### 1. Charged particle reconstruction

The trajectories of charged particles, "tracks," are reconstructed based on the energy deposits left in the trackers, "hits." The momenta of these particles are determined based on the bending of these trajectories induced by the magnetic fields in each detector. As shown in Figs. 2 and 3, charged particles follow helical trajectories in the *B* factories due to their solenoidal magnetic fields, while in LHCb the particles are simply deflected by the dipole magnet. In either case, charged track reconstruction proceeds with efficiencies of over 95% [for $p > 300$ MeV at the *B* factories (Bevan *et al.*, 2014) and $p > 5$ GeV at LHCb (Aaij *et al.*, 2015a)] and the momentum determination is achieved with a typical resolution of 0.5%–1%.

The reconstruction of the *b*-hadron secondary vertices is of primary importance to distinguish signal from background decays, especially in LHCb. In the *B* factories (Bevan *et al.*, 2014), the decay vertices of the short-lived *B* and *D* mesons

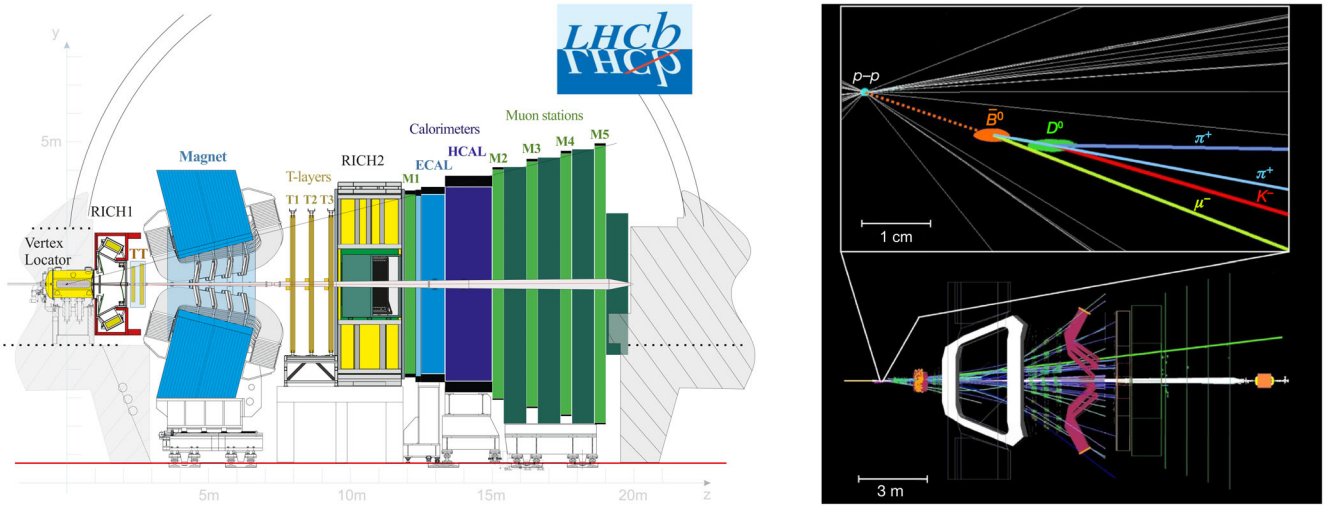


FIG. 3. Left panel: side view of the LHCb detector. See Augusto Alves *et al.* (2008) and Aaij *et al.* (2015a) for further details on the subdetectors and their acronyms. Right panel: side view of an event display for a $B^0 \to D^{*+}\tau^-\bar{\nu}_\tau$ decay. The area around the interaction point is enlarged in the inset at the top. The trajectory of the $B^0$ meson is indicated with a thick dotted line, and the trajectories of the particles from the subsequent $D^{*+} \to D^0\pi^+$, $D^0 \to K^-\pi^+$, and $\tau^- \to \mu^-\bar{\nu}_\mu\nu_\tau$ decays are illustrated with thick solid lines. Adapted from Aaij *et al.*, 2015a, and Ciezarek *et al.*, 2017.

were reconstructed with a resolution of 60–100 $\mu$m when they decayed inside the vertex trackers (about 80% of the time), and 100–400 $\mu$m when they decayed outside. LHCb reconstructs the impact parameter of the tracks, that is, their distance to the primary vertex in the plane transverse to the beam line, with an impressive resolution of 45 $\mu$m for $p_T = 1$ GeV, and down to 15 $\mu$m for high momenta tracks. As discussed in Sec. III.A.2, the vertex resolution along the beam line is of the order of 250 $\mu$m, which given the large boost of most particles at LHCb is sufficient to suppress prompt background processes by multiple orders of magnitude (Sec. IV.C.2).

For both the *B* factories and LHCb, charged leptons have generically clean signatures that can be differentiated from other types of particles with high efficiency. Electrons are reconstructed from tracks that match a cluster in the electromagnetic calorimeter with the appropriate shape and energy; muons are generally identified as tracks that leave hits in the outer muon detectors, with some additional inputs from the other subdetectors. However, the performance of the two kinds of experiments diverges substantially in the details.

At the *B* factories, both electrons and muons are reconstructed with efficiencies over 90% and with low misidentification rates, though the performance is generally better for electrons; see Fig. 4, Franco Sevilla (2012), and Aubert *et al.* (2013). For instance, a typical 2 GeV electron is reconstructed with 96% efficiency and a 0.3% pion misidentification probability, whereas a 2 GeV muon would have 92% efficiency and a 2.5% pion misidentification probability. In contrast, at LHCb the electron reconstruction is much more challenging because of the lower granularity of the electromagnetic calorimeter and the larger amount of material before it compared to the *B* factories. A 20 GeV electron is reconstructed with about 90% efficiency for a misidentification rate of 2.5%, while a muon with the same momentum would be reconstructed with 98% efficiency for a 1% misidentification rate [Fig. 5 and Aaij *et al.* (2015a)]. Additionally, the first level of the LHCb trigger from 2010 to 2018 was implemented on hardware and did not use information from the trackers, resulting in trigger efficiencies much lower for electrons than muons. This limitation will be overcome during the 2019–2021 upgrade by a software-only trigger.

Finally, charged light hadrons are identified primarily by their signatures in the Cherenkov detectors, as well as the energy deposition in the drift chamber for low momentum particles in the *B* factories. The right panels of Figs. 4 and 5 show the separation achieved for several species of charged hadrons in some of the Cherenkov detectors for *BABAR* and LHCb, respectively.

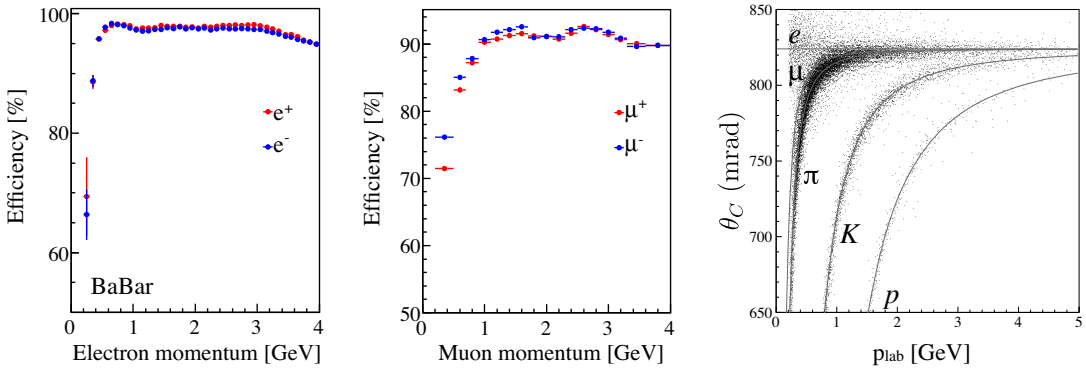


FIG. 4. Examples of particle reconstruction performance for the *BABAR* detector; the performance for the Belle detector is similar. Left panel: electron reconstruction efficiency. Middle panel: muon reconstruction efficiency. Right panel: Cherenkov angle measurement for different particles species at *BABAR*'s detector of internally reflected Cherenkov light. Adapted from Franco Sevilla, 2012, and Aubert *et al.*, 2013.

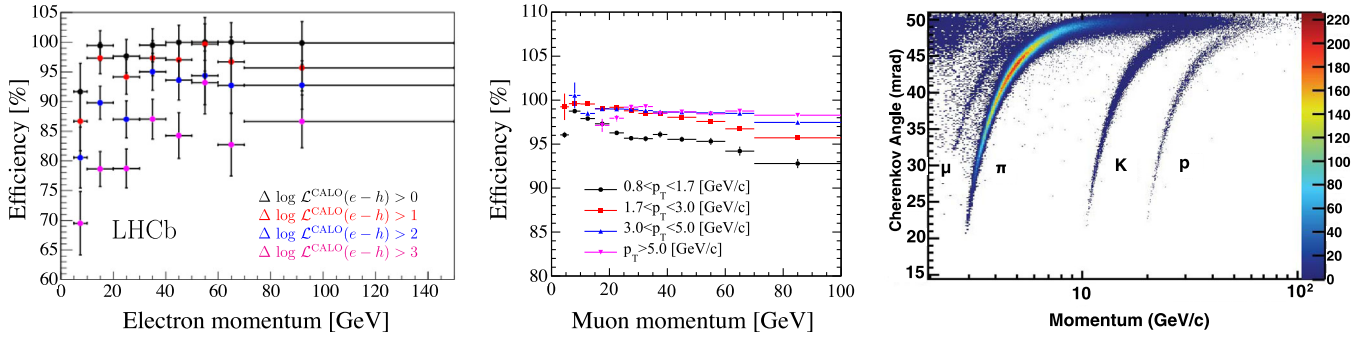


FIG. 5. Examples of particle reconstruction performance for the LHCb detector. Left panel: electron reconstruction efficiency. Middle panel: muon reconstruction efficiency. Right panel: Cherenkov angle measurement for different particle species at LHCb's Ring Imaging Cherenkov detector 1 (RICH1). Adapted from Aaij *et al.*, 2015a.

#### 2. Neutral particle reconstruction

Another key difference between $B$ factories and LHCb lies in the ability to efficiently reconstruct neutral particles: primarily photons in the case of LFUV measurements. The low material in front of the $B$-factory calorimeters, as well as their good resolution and granularities, allows them to fully reconstruct final states that contain $\pi^0$ mesons decaying to two photons (present, for instance, via the copious $D^0 \to K^-\pi^+\pi^0$ decay) as well as photons, such as those coming from $D^{*0} \to D^0\gamma$ decays. At LHCb, the previously discussed granularity and detector material challenges, as well as the high number of $b$ hadrons, have thus far led its LFUV measurements to avoid the reconstruction of final states with $\pi^0$ mesons or photons.

### C. Kinematic reconstruction: The *b*-hadron momentum

One of the major challenges in the reconstruction of semitauonic $H_b \to H_c\tau\nu$ decays is the determination of the parent $b$-hadron momentum. This momentum is necessary to measure important kinematic variables such as the momentum transfer $q^2 = (p_{H_b} - p_{H_c})^2 \equiv (p_\tau + p_\nu)^2$, which is not directly accessible because of the undetected neutrinos in the final state. In measurements involving the $\tau \to \ell\nu\bar{\nu}$ decay, the momentum of the parent $b$ hadron is further employed to reconstruct other invariants, such as the invariant mass of the unreconstructed particles

$$m^2_{\text{miss}} = (p_{H_b} - p_{H_c} - p_\ell)^2, \tag{44}$$

and the energy of the charged lepton in the $H_b$ rest frame

$$E^*_\ell = (p_\ell \cdot p_{H_b})/m_{H_b}. \tag{45}$$

In these leptonic-$\tau$ measurements, the signal and normalization modes ($H_b \to H_c\tau\nu$ and $H_b \to H_c\ell\nu$, respectively) are reconstructed in the same exact final state, differing only in the number of undetected neutrinos. Since normalization events only have one neutrino, their reconstructed $m^2_{\text{miss}}$ distribution is sharply peaked at zero, in contrast to the broad $m^2_{\text{miss}}$ distribution of signal events. Additionally, charged leptons in the signal events are generated in the secondary $\tau$ decay and thus have a lower maximum $E^*_\ell$ than those arising from normalization $H_b \to H_c\ell\nu$ decays.

In Sec. III.C.1 we describe how the $B$ factories take advantage of their precisely known $e^+e^-$ beam energies to determine the momentum of the signal $B$ in a $B\bar{B}$ event by reconstructing the accompanying tag $\bar{B}$. This procedure is not available in the busier hadronic environment of $pp$ collisions. Instead, LHCb employs the untagged methods detailed in Secs. III.C.2 and III.C.3. These methods have much higher efficiency than $B$ tagging, but at the cost of significantly worse $p_{H_b}$ resolution.

#### 1. *B* tagging at the *B* factories

As described in Sec. III.A.1, the $B$ factories produce $B$ mesons via $e^+e^- \to \Upsilon(4S) \to B\bar{B}$ decays. Since the momenta of the colliding electron-positron beams are known with high precision, the complete reconstruction of one of the two $B$ mesons (the tag $B$ or $B_{\text{tag}}$) can be used to fully determine the momentum of the other $B$ meson (the signal $B$ or $B_{\text{sig}}$) simply via $p_{B_{\text{sig}}} = p_{e^+e^-} - p_{B_{\text{tag}}}$.

This "tagging" has been implemented by the $B$ factories (Bevan *et al.*, 2014) in the following ways:

- *Hadronic B tagging*.—The $B_{\text{tag}}$ is fully reconstructed in final states that contain a charm hadron plus a number of pions and kaons. The full reconstruction of the decay results in the best possible $p_{B_{\text{sig}}}$ resolution (11%, as shown in Fig. 6) at the price of a lower 0.2%–0.8% efficiency (Table IV).
- *Semileptonic B tagging*.—The $B_{\text{tag}}$ is reconstructed in its $\bar{B}_{\text{tag}} \to D^{(*)}\ell\bar{\nu}$ decays. This leads to efficiencies as high as 2% thanks to the large values of the semileptonic branching fractions. The presence of an unreconstructed neutrino, however, results in a poor resolution of $p_{B_{\text{sig}}}$. To mitigate this effect, analyses employing this technique exploit the full reconstruction of the collision event and require that no unassigned charged or neutral particles should be present. They further avoid the direct use of $p_{B_{\text{sig}}}$.
- *Inclusive B tagging*.—No attempt is made to explicitly reconstruct the $B$ decay chain. Instead, a specific $B_{\text{sig}}$ candidate is first reconstructed. The tag side is then reconstructed using all remaining charged and neutral particles. This leads to a high efficiency, but also poor resolution of the tag-side momentum.

Table IV summarizes the performance of the most efficient algorithms employed by *BABAR*, Belle, and Belle II. The Belle II numbers are based on simulations.

The hadronic $B$ tagging algorithm of *BABAR* is based on the semiexclusive reconstruction (SER) of a charmed seed state of a $B \to H_cX$ cascade. Here $H_c$ can be either a charmed meson or a $J/\psi$ particle and $X$ is a number of charged and neutral pions or a single kaon. Combinations of seed mesons with

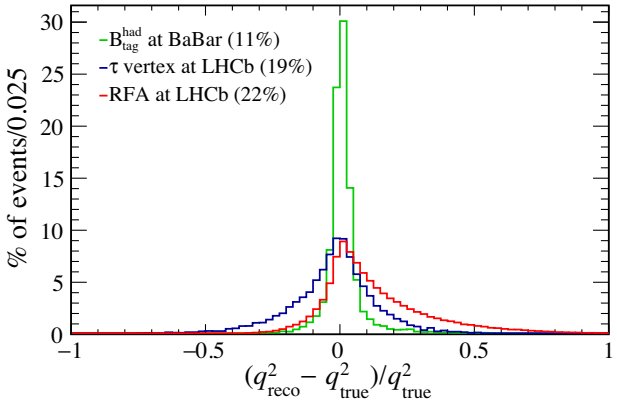


FIG. 6. Resolution on the $q^2$ reconstruction in simulated $B \to D^*\tau\nu$ decays for the different methods for estimating the $p_{B_{\text{sig}}}$ momentum. The $\tau$ vertex and rest-frame approximation (RFA) methods used at LHCb are described in Secs. III.C.2 and III.C.3, respectively. Each value in parentheses corresponds to the rms of the distribution. The various curves were extracted from Lees *et al.* (2013) and Aaij *et al.* (2015c, 2018b).

TABLE IV. Reconstruction efficiencies of some of the $B$ tagging algorithms employed by the $B$ factories. FEI stands for "full event interpretation," FR for "full reconstruction," and SER for "semi-exclusive reconstruction." The numbers were extracted from Lees *et al.* (2013) and Keck *et al.* (2019).

| $B$ tagging | Experiment | Algorithm | $B^{\pm}$ | $B^0$ |
|---|---|---|---|---|
| Hadronic | Belle II | FEI | 0.76% | 0.46% |
| | Belle II | FEI (FR channels) | 0.53% | 0.33% |
| | Belle | FR | 0.28% | 0.18% |
| | *BABAR* | SER | 0.4% | 0.2% |
| Semileptonic | Belle II | FEI | 1.80% | 2.04% |
| | Belle | FR | 0.31% | 0.34% |
| | *BABAR* | SER | 0.3% | 0.6% |

different $X$ constituents are selected based on the purity obtained from simulated samples.

Belle uses a similar ansatz, but relies on multivariate methods (either neural networks or boosted decision trees) to distinguish correctly reconstructed versus wrongly reconstructed tag candidates in a staged approach. Figure 7 illustrates this procedure for the full-event interpretation (FEI) algorithm described by Keck *et al.* (2019). This algorithm reconstructs one of the $B$ mesons produced in the collision event using either hadronic or semileptonic decay channels. Instead of attempting to reconstruct as many $B$ meson decay cascades as possible, the FEI algorithm employs a hierarchical reconstruction ansatz in several stages. At the initial stage, boosted decision trees are trained to identify charged tracks and neutral energy depositions as detector stable particles ($e^+$, $\mu^+$, $K^+$, $\pi^+$, $K_L^0$, and $\gamma$). At the following stages, these candidate particles are combined into composite particles ($\pi^0$ and $K_S^0$) and later heavier meson candidates ($J/\psi$, $D^0$, $D^+$, and $D_s$). For each target final state, a boosted decision tree is trained to identify probable candidates. The input features are the classifier outputs of the previous stages, vertex fit probabilities, and the four-momenta. Candidates for $D^{*0}$, $D^{*+}$, and $D_s^*$ mesons are formed similarly. At the final stage, all the information of the previous stages is combined to assess the viability of a $B_{\text{tag}}$ candidate. The full reconstruction (FR) algorithm uses a similar approach but one based on neural networks instead of boosted decision trees (BDTs). A more detailed description was given by Feindt *et al.* (2011). The performance of the FEI algorithm on early Belle II data was discussed by Abudinén *et al.* (2020).

In the future deep learning or graph-based network approaches might allow further increases in the reconstruction efficiency of algorithms like FEI at Belle II (Keck, 2017; Boeckh, 2020).

#### 2. $\tau \to \pi^-\pi^+\pi^-\nu$ vertex reconstruction at LHCb

At the LHC, the energies of the partons whose collisions produce the $b\bar{b}$ pairs are not known, so it is not possible to derive the four-momentum of one $b$ hadron from the reconstruction of the other. However, by taking advantage of the excellent vertexing capabilities of LHCb, in the case in which the $\tau$ lepton decays to at least three charged particles, the momentum of the parent $b$ hadron in $H_b \to H_{c,u}\tau\nu$ events can still be precisely determined up to a discrete ambiguity.

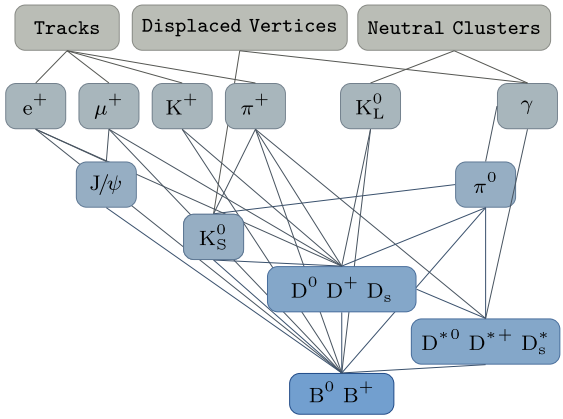


FIG. 7. Schematic illustration of the FEI algorithm. From Keck *et al.*, 2019.

This procedure was established in 2018 by the hadronic-$\tau$ measurement of $\mathcal{R}(D^{*+})$ with $\tau \to \pi^+\pi^+\pi^-\nu$ (Aaij *et al.*, 2018b).[7]

In general, about 100 tracks arise from a primary vertex (PV) within a $pp$ collision at LHCb, such that the location of this vertex can be measured to an excellent precision of around 10 $\mu$m along the beam direction. In $\bar{B}^0 \to D^{*+}\tau^-\bar{\nu}_\tau$ events with the $D^{*+}$ meson decaying promptly via the $D^{*+} \to D^0\pi^+$ strong decay, the $D^0$ vertex can be reconstructed as the intersection of its kaon and pion daughters with a 150 $\mu$m precision along the $z$ direction (Aaij *et al.*, 2018b) (see Fig. 8, top image). The vertex for the $\tau \to \pi^-\pi^+\pi^-\nu$ decay can be measured to a 200 $\mu$m precision. Because of the small angle between the directions of the bachelor pion produced in the $D^{*+}$ decay and the reconstructed $D^0$, their intersection has poor precision and is not used in the determination of the position of the $\bar{B}^0$ vertex. Instead, this position is estimated with a $\sim$1 mm resolution as the intersection of the $D^{*+}$ and $\tau$ trajectories, where the $\tau$ line of flight is approximated by the $\pi^-\pi^+\pi^-$ direction. Thanks to the large boost of $b$ hadrons at LHCb ($\beta\gamma \sim 50$), these three vertices are well separated and determine the directions of flight of the $\bar{B}^0$ meson and $\tau$ lepton momenta (the unit vectors $\hat{\boldsymbol{p}}_B$ and $\hat{\boldsymbol{p}}_\tau$, respectively) with fairly good precision.

With $\hat{\boldsymbol{p}}_\tau$ known and the $\pi^-\pi^+\pi^-$ hadronic state fully reconstructed, the $\tau$ energy can be determined up to a twofold ambiguity arising from the solution of the quadratic relation $(p_\tau - p_{\pi\pi\pi})^2 = 0$. This result, when further combined with $\hat{\boldsymbol{p}}_B$ and the full reconstruction of the $D^{*+}$, in turn allows the determination of the $B$ momentum up to a fourfold ambiguity from the quadratic $(p_B - p_{D^*} - p_\tau)^2 = 0$. The resulting overall $q^2$ resolution is around 19%.

#### 3. Rest-frame approximation with $\tau \to \mu\nu\bar{\nu}$ at LHCb

It is not possible to reconstruct the $\tau$ vertex when the $\tau$ lepton is identified by its one-prong $\tau \to \mu\nu\bar{\nu}$ decay (Fig. 8, bottom image). Thus, semitauonic measurements at LHCb that make use of this decay mode estimate the momentum of

[7]The channel $\tau \to \pi^-\pi^+\pi^-\nu$ always includes contributions from the $\tau \to \pi^-\pi^+\pi^-\pi^0(\pi^0)\nu$ channels unless otherwise specified.

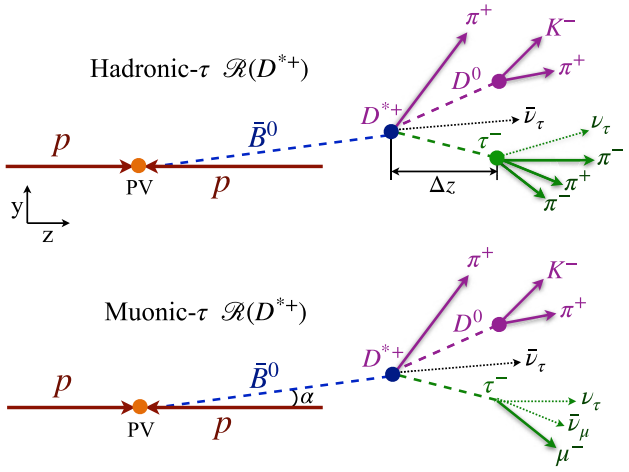


FIG. 8. Reconstructed topologies for the $B \to D^* \tau \nu$ decays in the hadronic-$\tau$ (Aaij *et al.*, 2018b) (top) and muonic-$\tau$ (Aaij *et al.*, 2015c) (bottom) measurements of $\mathcal{R}(D^{*+})$ at LHCb. The filled circles correspond to the reconstructed vertices, and solid lines to reconstructed particles. "PV" refers to the primary vertex, $\Delta z$ indicates the distance in the $z$ direction between the $\bar{B}^0$ (or $D^{*+}$) and $\tau^-$ vertices, and $\alpha$ refers to the angle between the beam axis and the momentum of the $\bar{B}^0$ meson.

the $b$ hadron via the rest-frame approximation (RFA) instead. This procedure assumes that the proper velocity of the $H_b$ hadron along the $z$ axis (the beam axis) is the same as that of the reconstructed charm-muon system, $\mu H_c$. This leads to the relationship $(p_{H_b})_z/m_{H_b} = (p_{\mu H_c})_z/m_{\mu H_c}$. Since the direction of flight of the $b$ hadron can be determined by the displacement of the $H_b$ decay vertex from the primary vertex, the $H_b$ momentum can then be estimated via

$$|p_{H_b}| = \frac{m_{H_b}}{m_{\mu H_c}} (p_{\mu H_c})_z \sqrt{1 + \tan^2\alpha}, \tag{46}$$

where $\alpha$ is the angle between the $H_b$ direction of flight and the $z$ axis, as shown in Fig. 8.

In the highly boosted regime of LHCb, the RFA is a fairly good approximation that leads to an adequate overall $q^2$ resolution of about 22% (see Fig. 6), albeit with a long tail on the positive side and some bias. Note that this resolution is highly $q^2$ dependent, as it varies between 34% for $q^2 < 5\ \mathrm{GeV}^2$ and 7% at $q^2 > 9\ \mathrm{GeV}^2$.

In general, semitauonic measurements at LHCb that make use of the hadronic-$\tau$ reconstruction will have better precision for the reconstruction of kinematic distributions than muonic-$\tau$ measurements. In contrast, the latter may have a better ultimate precision in the determination of the ratios $\mathcal{R}(H_c)$ because they do not depend on external branching fractions in the normalization of the signal $H_b \to H_c \tau \nu$ decays, such as those used in Eq. (53).

In the future, LHCb may be able to improve the precision on the $b$-hadron momentum reconstructrion by taking advantage of the large samples of $b$ hadrons that will be collected over the next decade and a half. For instance, the reconstruction of $B^+$ mesons arising from $B^*_{s2} \to B^+ K^-$ decays allows for a higher-precision determination of the $B^+$ kinematics by constraining the invariant mass of the $B^+ K^-$ system to the known $B^*_{s2}$ mass, but it comes at the price of a less than 1% reconstruction efficiency. This technique has already been successfully employed to reconstruct $B^- \to D^{(*,**)0} \mu^- \bar{\nu}_\mu$ decays (Aaij *et al.*, 2019b), and it could be applied to semitauonic decays in the future as well.

## IV. EXPERIMENTAL TESTS OF LEPTON FLAVOR UNIVERSALITY

The decay $B \to D^* \tau \nu$ was first observed in 2007 by the Belle Collaboration (Matyja *et al.*, 2007), and subsequent measurements by *BABAR* (Aubert *et al.*, 2008) and Belle (Adachi *et al.*, 2009; Bozek *et al.*, 2010) found evidence for $B \to D \tau \nu$ decays as well. These measurements all saw values of $\mathcal{R}(D^{(*)})$ that exceeded the SM expectations, but the significance of these excesses was low due to the large uncertainties involved in these early results: above 20% for $\mathcal{R}(D^*)$ and over 30% for $\mathcal{R}(D)$. All of these measurements have now been superseded, so they are not discussed further in this review.

The first evidence for an excess of $B \to D^{(*)} \tau \nu$ decays was reported by *BABAR* in 2012 (Lees *et al.*, 2012), a measurement that also included the first observation of $B \to D \tau \nu$ decays. Similar excesses have been reported since by the Belle (Huschle *et al.*, 2015; Sato *et al.*, 2016; Hirose *et al.*, 2018; Caria *et al.*, 2020) and LHCb experiments (Aaij *et al.*, 2015c, 2018b). The persistent nature of these anomalies has spurred wide interest in semitauonic decays and, as a result, other channels that proceed via $b \to u \tau \nu$ or different $b \to c \tau \nu$ transitions are being studied. Two such results have been published thus far: Belle's search for $B \to \pi \tau \nu$ decays (Hamer *et al.*, 2016) and LHCb's measurement of $\mathcal{R}(J/\psi)$ (Aaij *et al.*, 2018a). The first measurements of the polarization of some of the decay products were reported by Belle (Sato *et al.*, 2016; Abdesselam *et al.*, 2019) as well.

In this section we describe the key features of all of these measurements regarding their event selection, background determination, main uncertainties, and signal extraction. In Secs. IV.A–IV.D the various results are grouped according to their $b$-hadron tagging method, which, as we saw in Sec. III.C, can be employed to determine the momentum of the parent $b$ hadron and has a substantial impact on the approach to determining the signal yields and on the composition of the background contributions. Table V shows an overview of the results and the sections in which they are discussed. Additionally, Sec. V offers a deeper dive into the various sources of systematic uncertainty to which these measurements are subject, as well the prospects for its reduction. Section VI provides combinations of the various $\mathcal{R}(D^{(*)})$ results and comparisons of all the observables with their respective SM predictions.

There are, in addition, several measurements of the inclusive $B \to X_c \tau \nu$ rate that we do not cover in this section. These comprise LEP measurements of $b \to X \tau \nu$ (Acciarri *et al.*, 1994, 1996; Abreu *et al.*, 2000; Abbiendi *et al.*, 2001; Barate *et al.*, 2001) that require assumptions about the cancellation of hadronization effects in order to be interpreted as $B \to X \tau \nu$ measurements, as well as a recent result that is unpublished

TABLE V. Summary of the different results covered by this review, classified by the measured observable and the deployed method. The references for each experiment are given as table footnotes; the relevant sections of this review are provided beneath each result.

| Observable | Method: Hadronic tag | Semileptonic tag | Untagged |
|---|---|---|---|
| $\mathcal{R}(D)$ | 0.440(58)(42)[a] Sec. IV.A.1<br>0.375(64)(26)[c] Sec. IV.A.1 | 0.307(37)(16)[b] Sec. IV.B.1 | |
| $\mathcal{R}(D^*)$ | 0.332(24)(18)[a] Sec. IV.A.1<br>0.293(38)(15)[c] Sec. IV.A.1<br>$0.270(35)^{(+28)}_{(-25)}$[g] Sec. IV.A.1 | 0.302(30)(11)[d] Sec. IV.B.1<br>0.283(18)(14)[b] Sec. IV.B.1 | 0.336(27)(30)[e] Sec. IV.C.1<br>0.280(18)(25)(13)[f] Sec. IV.C.2 |
| $P_\tau(D^*)$ | $-0.38(51)^{(21)}_{(16)}$[g] Sec. IV.D.1 | | |
| $F_{L,\tau}(D^*)$ | | | 0.60(8)(4)[h] Sec. IV.D.2 |
| $\mathcal{R}(J/\psi)$ | | | 0.71(17)(18)[i] Sec. IV.C.3 |
| $\mathcal{R}(\pi)$ | 1.05(51)[j] Sec. IV.A.2 | | |

[a] *BABAR* (Lees *et al.*, 2012, 2013), with $\rho = -0.31$.
[b] Belle (Caria *et al.*, 2020), with $\rho = -0.52$.
[c] Belle (Huschle *et al.*, 2015), with $\rho = -0.50$.
[d] Belle (Sato *et al.*, 2016).
[e] LHCb (Aaij *et al.*, 2015c).
[f] LHCb (Aaij *et al.*, 2018b), with $\tau \to \pi^+\pi^+\pi^-\nu$ updated taking into account the latest HFLAV average of $\mathcal{B}(B^0 \to D^{*+}\ell\nu) = (5.08 \pm 0.02 \pm 0.12)\%$. The third uncertainty is from external branching fractions.
[g] Belle (Hirose *et al.*, 2017, 2018), with single-prong $\tau$ hadronic decays.
[h] Belle (Abdesselam *et al.*, 2019) using inclusive tagging.
[i] LHCb (Aaij *et al.*, 2018a).
[j] Belle (Hamer *et al.*, 2016) when combined with world-averaged $\mathrm{Br}(B \to \pi\ell\nu)$.

(Hasenbusch, 2018). A comparison of the predicted and measured rates from inclusive and exclusive semitauonic decays is presented in Sec. VI.C.

### A. *B*-factory measurements with hadronic tags

We describe here some of the most recent semitauonic results involving hadronic $B$ tags: the measurements of $B \to D^{(*)}\tau\nu$ decays by *BABAR* (Lees *et al.*, 2012, 2013) and Belle (Huschle *et al.*, 2015) in Sec. IV.A.1, as well as a 2015 search for $B \to \pi\tau\nu$ decays by Belle (Hamer *et al.*, 2016) in Sec. IV.A.2. An additional measurement of $B \to D^{(*)}\tau\nu$ decays by Belle involving hadronic tags focused on the polarization of the $\tau$ lepton (Hirose *et al.*, 2017, 2018) and is described in Sec. IV.D.

#### 1. $\mathcal{R}(D^{(*)})$ with $\tau \to \ell\nu\bar{\nu}$

The *BABAR* experiment published the first high-precision measurement of $\mathcal{R}(D^{(*)})$ based on their full dataset of $471 \times 10^6$ $B\bar{B}$ pairs in 2012 (Lees *et al.*, 2012, 2013). The Belle experiment followed in 2015 with an analysis of their $772 \times 10^6$ $B\bar{B}$ pair dataset (Huschle *et al.*, 2015), which employed a similar strategy. In both cases, signal ($B \to D^{(*)}\tau\nu$) and normalization ($B \to D^{(*)}\ell\nu$) decays were selected using the same particles in the final state: a $D$ or $D^*$ meson and a charged light lepton $\ell = e$ or $\mu$. In the case of signal events, the light lepton $\ell$ comes from the secondary $\tau \to \ell\nu\bar{\nu}$ decay, which leads to two additional neutrinos in the final state and a typically lower lepton momentum. The $D$ mesons are reconstructed by combinations of $K^+$, $K^0_S$, $\pi^+$, and $\pi^0$ mesons with invariant masses close to the nominal $D^0$ and $D^+$ masses, which cover 25%–35% of the total $D$ branching fractions. The heavier $D^*$ mesons are identified using the $D^{*+} \to D^0\pi^+, D^+\pi^0$ and $D^{*0} \to D^0\pi^0, D^0\gamma$ decays.

To separate signal from normalization decays as well as to reduce background contributions, the event is also required to have a fully reconstructed hadronic $B_{\mathrm{tag}}$ and no additional tracks; see Sec. III.C.1. As described there, the reconstruction efficiency of the $B_{\mathrm{tag}}$ is only ≈0.3%, but it allows these measurements to accurately determine the four-momentum of the signal $B$, which in turn is used to calculate the momentum transfer $q^2 = (p_{B_{\mathrm{sig}}} - p_{D^{(*)}})^2$ and the missing momentum of the unreconstructed neutrinos $p_{\mathrm{miss}} = p_{B_{\mathrm{sig}}} - p_{D^{(*)}} - p_\ell = p_{e^+e^-} - p_{B_{\mathrm{tag}}} - p_{D^{(*)}} - p_\ell$. The invariant missing mass $m^2_{\mathrm{miss}} = p^2_{\mathrm{miss}}$ peaks at zero for the one-neutrino normalization events but has a broad distribution at positive values for signal events with three neutrinos in the final state.

A key variable to further reduce background contributions is $E_{\mathrm{ECL}}$: the sum of the energy deposits in the calorimeter that are not associated with the tag or signal $B$ decays. Events involving signal and normalization decays have all their visible final state particles reconstructed, but background decays to $D^{**}$ mesons (among others) can enter the signal selection when their daughter $\pi^0$ mesons or photons are unassigned. Both *BABAR* and Belle feed $E_{\mathrm{ECL}}$ to multivariate classifiers that are trained to reject these background contributions. In the case of *BABAR*, the output of the classifier, a boosted decision tree, is required to have a minimum value for the event to be selected. As we later describe, Belle fits the output distributions of the classifier (from a neural network) directly. Finally, only events with $q^2 > 4\ \mathrm{GeV}^2$ are selected, a requirement that takes advantage of the momentum transfer of signal events being kinematically constrained to lie above $m^2_\tau = 3.16\ \mathrm{GeV}^2$.

The number of signal, normalization, and background events in each of the $D^0\ell$, $D^+\ell$, $D^{*0}\ell$, and $D^{*+}\ell$ data samples is determined by maximum likelihood fits to the observed data distributions. The ratios of yields for the isospin-related contributions (such as $D^0\ell$ vs $D^+\ell$ or $D^{*0}\ell$ vs $D^{*+}\ell$) are constrained by the known branching fractions and simulated relative efficiencies. *BABAR* employs an additional fit without these constraints that checks the consistency with the expected percent-level degree of isospin breaking. The probability distribution functions (PDFs) that describe each of the contributions are taken from Monte Carlo simulations that make use of the CLN form factor parametrization (Sec. II.C.2) for the signal and normalization modes, the

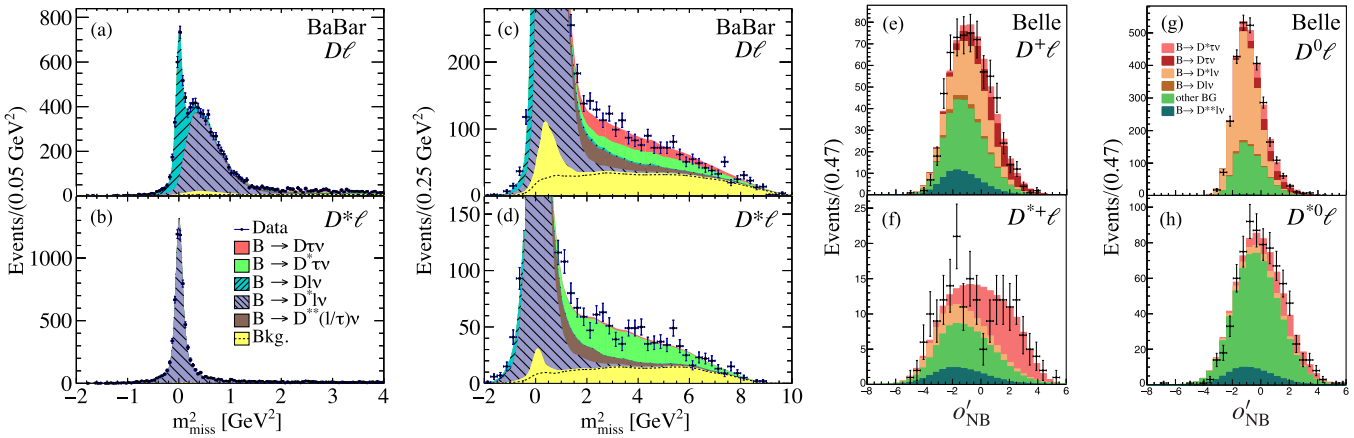


FIG. 9. Projections of the signal fits for the *BABAR* (Lees *et al.*, 2012) and Belle (Huschle *et al.*, 2015) measurements of $\mathcal{R}(D^{(*)})$ with hadronic tagging. (a),(b) Full $m^2_{\rm miss}$ projections of the *BABAR* fit showing the normalization components for the $D\ell$ and $D^*\ell$ samples (a combination of $D^{(*)0}\ell$ and $D^{(*)+}\ell$). (c),(d) $m^2_{\rm miss}$ projections of the *BABAR* fit focusing on the signal contributions at high $m^2_{\rm miss}$. (e)–(h) Full projections of the fit to the neural network output $o'_{\rm NB}$ by Belle in the region $m^2_{\rm miss} > 0.85$ GeV$^2$ for the four $D^{(*)}\ell$ samples.

LLSW form factor parametrization (Leibovich *et al.*, 1997) for $B \to D^{**} l\nu$ decays,[8] and other phase-space-based models augmented with corrections from data control samples for the rest of the background contributions. Additional assumptions on the $D^{**}$ branching fractions are described in Sec. V.C.2.

The *BABAR* analysis employs a two-dimensional fit to the $m^2_{\rm miss}$ and the charged lepton energy in the $B$ rest frame ($E^*_\ell$), while Belle fits the $m^2_{\rm miss}$ distribution for $m^2_{\rm miss} < 0.85$ GeV$^2$ and the output of the classifier at high $m^2_{\rm miss}$. Figure 9 shows some of the relevant projections for both fits. The narrow peaks in Figs. 9(a) and 9(b), including that of the *feed-down* $B \to D^*\ell\nu$ decays reconstructed in the $D\ell$ sample with a broader $m^2_{\rm miss}$ distribution, illustrate the power of hadronic tagging in discriminating signal from normalization decays. Table VI shows a comparison of their fitted yields. Although the Belle dataset is 64% larger, the signal yields are about 40% smaller due to the lower reconstruction efficiency. The differences in the background yields are primarily due to *BABAR* placing a requirement on the multivariate classifier and Belle fitting its output instead.

The most challenging background contribution arises from $B \to D^{**}\ell\nu$ and $B \to D^{**}\tau\nu$ decays. The $B \to D^{**}\ell\nu$ processes are estimated in control samples with the same selection as the signal samples, except for the addition of a $\pi^0$ meson. In these control samples, decays of the form $\bar{B} \to D^{(*)}\pi^0\ell^-\bar{\nu}_\ell$ have values of $m^2_{\rm miss}$ close to zero, so their yields are easily determined with fits to this variable. This fit is performed simultaneously with the fits to the signal samples, and the $B \to D^{**} l\nu$ contribution to both is linked by the ratio of expected yields taken from the simulation. Additional backgrounds from continuum and combinatorial $B$ processes are estimated from data control samples and are fixed in the fits.

[8]As a reminder, throughout this review $l$ stands for $e$, $\mu$, or $\tau$, and $\ell$ represents $e$ or $\mu$.

Table VII summarizes all the sources of uncertainty in the $\mathcal{R}(D^{(*)})$ ratios measured by both analyses. The largest uncertainties come from the $B \to D^{**} l\nu$ contributions and the limited size of the simulated samples ("MC stats"). The latter uncertainty primarily affects the PDFs describing the kinematic distributions of all the components in the fit. The branching fraction ratios are calculated as

$$\mathcal{R}(D^{(*)}) = \frac{N_{\rm sig}}{N_{\rm norm}} \frac{\epsilon_{\rm norm}}{\epsilon_{\rm sig}}, \tag{47}$$

where $N_{\rm sig}$ and $N_{\rm norm}$ are the number of signal and normalization events determined by the fit, respectively, and $\epsilon_{\rm sig}/\epsilon_{\rm norm}$ is the ratio of efficiencies taken from simulation. Since the signal and normalization decays are reconstructed using the same particles in the final state, many uncertainties cancel in the ratio, leading to a relatively small 2% to 3% overall uncertainty for this quantity.

Table VIII shows the results from the *BABAR* and Belle analyses, which are compatible within uncertainties. The isospin-unconstrained results from *BABAR* (Table XIX in Sec. VI.A) show good agreement with the expected percent-level degree of isospin breaking. The total uncertainty on

TABLE VI. Comparison of the total yields extracted by the isospin-constrained fits from *BABAR* (Lees *et al.*, 2012) and Belle (Huschle, 2015). The "$\epsilon$ ratio" column corresponds to the ratio of the Belle fitted yields to the *BABAR* fitted yields normalized by the datasets, $4.71 \times 10^8$ of $B\bar{B}$ pairs for *BABAR* and $7.72 \times 10^8$ pairs for Belle.

| Sample | Contribution | *BABAR* | Belle | $\epsilon$ ratio |
|---|---|---|---|---|
| $D\ell$ | $B \to D\tau\nu$ | 489 | 320 | 0.40 |
| | $B \to D\ell\nu$ | 2981 | 3147 | 0.64 |
| | $B \to D^{**} l\nu$ | 506 | 239 | 0.29 |
| | Other background | 1033 | 2005 | 1.18 |
| $D^*\ell$ | $B \to D^*\tau\nu$ | 888 | 503 | 0.35 |
| | $B \to D^*\ell\nu$ | 11 953 | 12 045 | 0.61 |
| | $B \to D^{**} l\nu$ | 261 | 153 | 0.36 |
| | Other background | 404 | 2477 | 3.74 |

TABLE VII. Summary of the relative uncertainties for the *BABAR* (Lees *et al.*, 2012) and Belle (Huschle *et al.*, 2015) measurements of $\mathcal{R}(D^{(*)})$ with hadronic tagging.

| | | Uncertainty (%) | | | | |
|---|---|---|---|---|---|---|
| | | *BABAR* | | Belle | | |
| Result | Contribution | Syst. | Stat. | Syst. | Stat. | Ratio |
| $\mathcal{R}(D)$ | $B \to D^{**} l\nu$ | 5.8 | | 4.4 | | 0.76 |
| | MC stats | 5.7 | | 4.4 | | 0.78 |
| | $B \to Dl\nu$ | 2.5 | | 3.3 | | 1.30 |
| | Other background | 3.9 | | 0.7 | | 0.18 |
| | Particle ID | 0.9 | | 0.5 | | 0.54 |
| | **Total systematic** | **9.6** | | **7.1** | | **0.74** |
| | **Total statistical** | | **13.1** | | **17.1** | **1.31** |
| | **Total** | **16.2** | | **18.5** | | **1.14** |
| $\mathcal{R}(D^*)$ | $B \to D^{**} l\nu$ | 3.7 | | 3.4 | | 0.90 |
| | MC stats | 2.8 | | 3.6 | | 1.31 |
| | $B \to D^* l\nu$ | 1.0 | | 1.3 | | 1.31 |
| | Other background | 2.3 | | 0.7 | | 0.29 |
| | Particle ID | 0.9 | | 0.5 | | 0.54 |
| | **Total systematic** | **5.6** | | **5.2** | | **0.93** |
| | **Total statistical** | | **7.1** | | **13.0** | **1.83** |
| | **Total** | **9.0** | | **14.0** | | **1.56** |

TABLE VIII. Results of the *BABAR* (Lees *et al.*, 2012) and Belle (Huschle *et al.*, 2015) measurements of $\mathcal{R}(D^{(*)})$ with hadronic tagging. The first uncertainty is statistical and the second is systematic.

| Result | *BABAR* | Belle |
|---|---|---|
| $\mathcal{R}(D)$ | $0.440 \pm 0.058 \pm 0.042$ | $0.375 \pm 0.064 \pm 0.026$ |
| $\mathcal{R}(D^*)$ | $0.332 \pm 0.024 \pm 0.018$ | $0.293 \pm 0.038 \pm 0.015$ |

$\mathcal{R}(D^{(*)})$ in these measurements is dominated by the statistical uncertainty, so the much larger data samples expected to be collected by Belle II should improve these results significantly.

Thorough checks of the stability of these results were performed, including separate fits to the muon and electron samples, fits to the various running periods, and fits to samples with modified selection requirements that varied the signal over background ratio $S/B$ from 1.27 to 0.27. In all cases, the results were compatible with the nominal result. Additionally, a number of kinematic distributions of signal-enriched samples were compared with the fitted SM signal plus background model and resulted in good agreement overall. Figure 10 shows the distributions for the energy substituted mass $m_{\rm ES} = \sqrt{E^2_{\rm beam} - \boldsymbol{p}^2_{\rm tag}}$, which peaks at the $B$ mass for correctly reconstructed events, and $E_{\rm ECL}$. In both cases, the distributions are consistent with the fitted signal events to be coming from $B$ mesons with no additional unreconstructed particles in the event.

Finally, Fig. 11 shows the measured efficiency-corrected $q^2$ distributions for $B \to D^{(*)}\tau\nu$ decays and displays good agreement with the SM expectations. The measured distributions are also compared in Figs. 11(e) and 11(f) with the expectations from the type-II two-Higgs doublet model (2HDM) with $\tan\beta/m_{H^\pm} = 0.45\ \text{GeV}^{-1}$, which proceeds primarily via a scalar mediator. The *BABAR* analysis recalculates the signal PDFs, reweighting the light-lepton momentum to approximately account for the changes in helicity, for each value of $\tan\beta/m_{H^\pm}$ and fits the data again, so the data points in Figs. 11(c) and 11(d) are somewhat different than those in Figs. 11(e) and 11(f) due to the slightly different background and signal cross-feed subtraction. Including systematic uncertainties, this benchmark model is excluded at greater than 95% confidence level.

### 2. Search for $B \to \pi\tau\nu$ decays

Charmless semitauonic decays offer an interesting independent probe of LFUV to complement the excesses observed in various $\mathcal{R}(D^{(*)})$ measurements. Although they involve different four-Fermi operators and are CKM suppressed, they also offer access to third generation semileptonic decays in an experimental setting with a significantly different background composition. The most promising candidate for a first observation is the $B \to \pi\tau\nu$ channel. Further, even modest

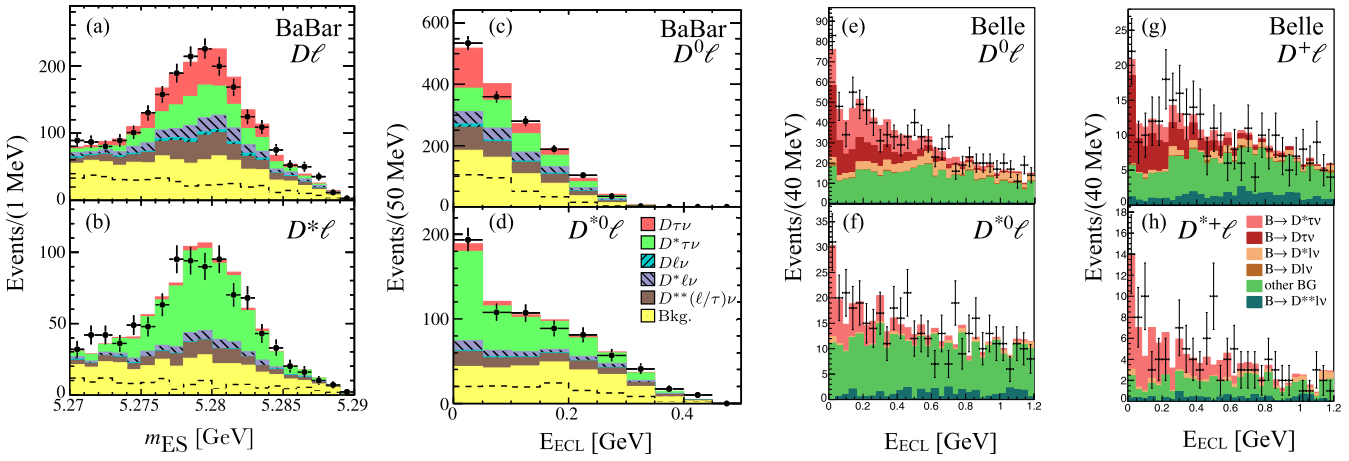


FIG. 10. Checks on the kinematic distributions for events in the signal enhanced high-$m^2_{\rm miss}$ region [$m^2_{\rm miss} > 1.5\ \text{GeV}^2$ for (a)–(d) and $m^2_{\rm miss} > 2\ \text{GeV}^2$ for (e)–(h)]. The solid histograms correspond to the simulation scaled to the fit results. Adapted from Lees *et al.*, 2013, and Huschle *et al.*, 2015.

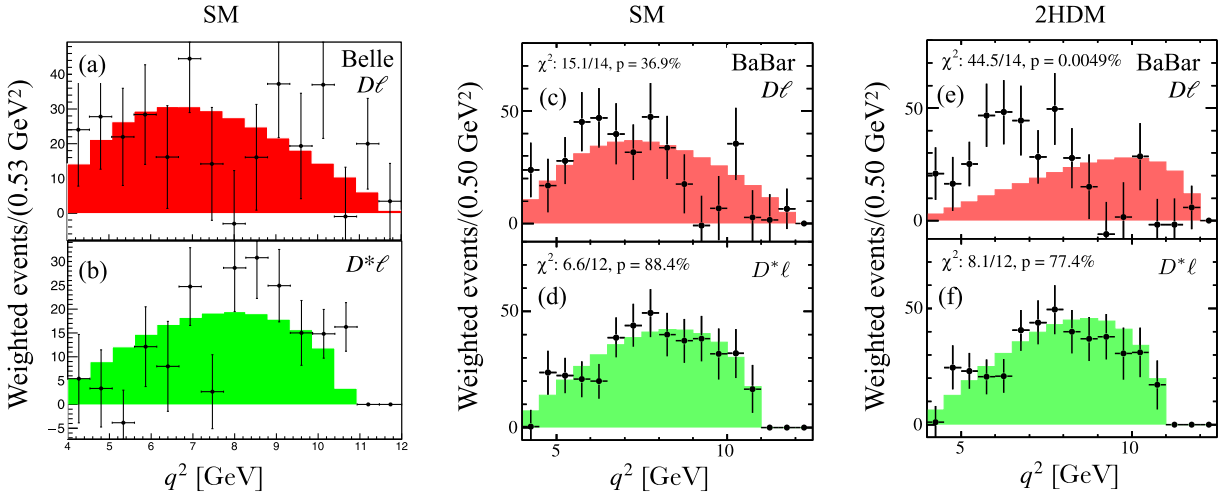


FIG. 11. Efficiency-corrected $q^2$ distributions for $B \to D\tau\nu$ (top panels) and $B \to D^*\tau\nu$ events (bottom panels) with (a), (b) $m^2_{\rm miss} > 0.85$ GeV$^2$ and (c)–(f) $m^2_{\rm miss} > 1.5$ GeV$^2$. The shaded distributions correspond to the SM expectations in (a)–(d) and a type-II 2HDM with $\tan\beta/m_{H^\pm} = 0.45$ GeV$^{-1}$, the value that reproduces that of $\mathcal{R}(D)$ measured by *BABAR*, in (e) and (f). The $\chi^2$ values are calculated based on the statistical uncertainties only. Adapted from Lees *et al.*, 2013, and Huschle *et al.*, 2015.

precision could already strongly constrain new physics models involving scalar mediators such as the type-II 2HDM (Bernlochner, 2015).

A first limit on the branching fraction of this decay was obtained by Belle in 2015 (Hamer *et al.*, 2016), which followed a similar strategy to that employed by Belle's hadronic tag measurement of $\mathcal{R}(D^{(*)})$. For the $B \to \pi\tau\nu$ analysis, $B_{\rm tag}$ mesons are selected only when the best candidate is compatible with the decay of a neutral $B$ meson. To boost the reconstructed number of $B \to \pi\tau\nu$ signal decays, both electronic $\tau \to e\nu\bar{\nu}$ and hadronic one-prong $\tau \to \pi\nu$ and $\tau \to \rho\nu$ decays were included in the reconstruction. The signal side is thus required to have at most two oppositely charged tracks, with one of those tracks having a particle identification compatible with an electron in the case of $\tau \to e\nu\bar{\nu}$ decays. For the $\rho^+ \to \pi^+\pi^0$ reconstruction, neutral pion candidates, which are not used in the tag reconstruction, are constructed from neutral energy depositions in the calorimeter. If multiple $\rho$ candidates exist, the one with the mass closest to the nominal $\rho$ mass is kept. To reduce the background from $B \to X_c\ell\nu$ decays, events with $K_L$ candidates are vetoed. Such candidates are identified by a cluster in the outer $K_L$-and-muon detector ("KLM" in Fig. 2) with no energy depositions in the electromagnetic calorimeter near the flight path of the $K_L$ candidate.

With all particles assigned to either the tag or signal side, $E_{\rm ECL}$ can be reconstructed from the remaining neutral clusters in the collision event. To further reduce the backgrounds, three boosted decision trees are trained: one for each probed $\tau$ decay mode. The input variables are as follows:

- The four-momenta of all signal particles.
- $q^2$ as calculated from the tag-side $B$ meson four-momentum and the signal-side pion with the highest momentum for signal decays $q^2 \geq m_\tau^2$, whereas lower values are possible for the backgrounds.
- $m^2_{\rm miss}$. For signal decays we expect a higher missing mass because of the additional neutrinos in the final state.

Requirements on the classifier outputs are chosen to select signal events such that each channel has an optimal statistical sensitivity. The resulting number of signal events is then extracted via a simultaneous fit of the respective $E_{\rm ECL}$ distributions. The postfit distributions are shown in Fig. 12. The measurement quotes an upper limit of $\mathcal{B}(B \to \pi\tau\nu) < 2.5 \times 10^{-4}$ at 90% C.L. This can be converted into a value of

$$\mathcal{R}(\pi) = 1.05 \pm 0.51, \tag{48}$$

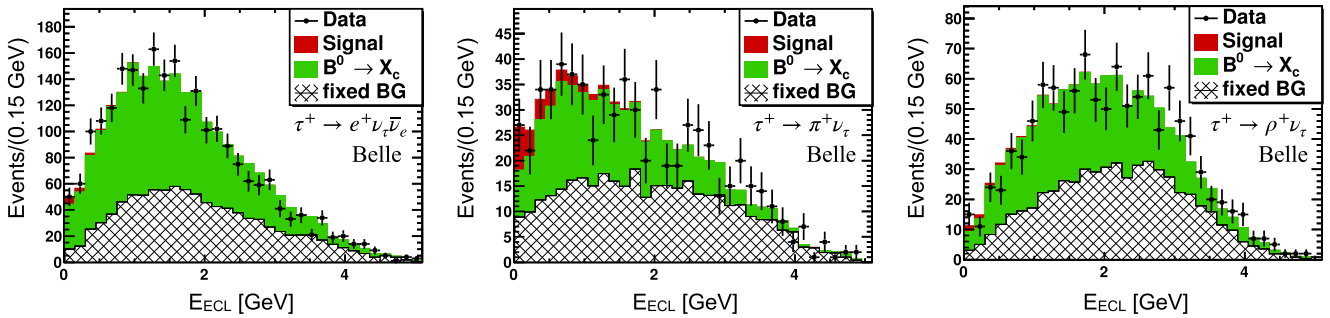


FIG. 12. Signal fit for the Belle measurement of $B \to \pi\tau\nu$ decays. The $E_{\rm ECL}$ distributions for the three reconstructed $\tau$ decay modes are shown: (left panel) $\tau \to e\nu\bar{\nu}$, (middle panel) $\tau \to \pi\nu$, and (right panel) $\tau \to \rho\nu$. Adapted from Hamer *et al.*, 2016.

TABLE IX. Summary of the relative uncertainties for the measurement of $B \to \pi\tau\nu$ decays by Belle (Hamer *et al.*, 2016).

| Contribution | Uncertainty (%) Syst. | Stat. |
|---|---|---|
| $B \to X_c \ell\nu$ | 2.2 | |
| Signal modeling | 1.8 | |
| Tagging calibration | 4.6 | |
| $K_L$ veto | 3.2 | |
| Particle ID | 2.4 | |
| Bkg. modeling | 4.4 | |
| Other | 3.2 | |
| **Total systematic** | **8.3** | |
| **Total statistical** | | **48** |
| **Total** | **49** | |

which is compatible with the SM expectation of $R(\pi)_{\mathrm{SM}} = 0.641 \pm 0.016$ (Bernlochner, 2015).

Table IX shows an overview of the systematic uncertainties of the result. The largest systematic uncertainties stem from the tagging calibration, as the measurement was not carried out as a ratio with respect to the light-lepton mode. The $K_L$ veto, used to reduce the background from CKM favored semileptonic decays, introduces a large uncertainty due to the poorly known $K_L$ reconstruction efficiency.

### B. Belle measurements with semileptonic tags

#### 1. $\mathcal{R}(D^{(*)})$ with $\tau \to \ell\nu\bar{\nu}$

The first measurement of $\mathcal{R}(D^*)$ using semileptonic tagging was performed by Belle (Sato *et al.*, 2016), a result that was subsequently superseded by Belle's combined measurement of $\mathcal{R}(D)$ and $\mathcal{R}(D^*)$ in 2020 (Caria *et al.*, 2020). This analysis employs the FEI algorithm (described in Sec. III.C.1) to efficiently identify semileptonic $B$ meson decays of the second $B$ meson ($B_{\mathrm{tag}}$) in the event. This allows for the full identification of all particles and decay cascades in the collision event and the reliable reconstruction of $E_{\mathrm{ECL}}$, the unassigned energy in the calorimeter, as already defined in Sec. IV.A. Tag-side $B \to D^{(*)}\ell\nu$ decays are selected by exploiting the observable

$$\cos\theta_{B,D^{(*)}\ell} \equiv \frac{2E_{\mathrm{beam}}E_{D^{(*)}\ell} - m_B^2 - m_{D^{(*)}\ell}^2}{2|\boldsymbol{p}_B||\boldsymbol{p}_{D^{(*)}\ell}|}, \tag{49}$$

in which the energies and momenta $E$ and $\boldsymbol{p}$ are all defined in the center-of-mass (c.m.) frame [the $\Upsilon(4S)$ rest frame] of the colliding beams. In particular, note that $E_{D^{(*)}\ell}$ and $\boldsymbol{p}_{D^{(*)}\ell}$ are the energy and momentum of the $D^{(*)}\ell$ system, respectively, and that in this frame $E_{\mathrm{beam}} = E_B$. For $B \to D^{(*)}\ell\nu$ decays with a single final state neutrino, which satisfy $(p_B - p_{D^{(*)}\ell})^2 = m_\nu^2 \simeq 0$, the definition of $\cos\theta_{B,D^*\ell}$ corresponds to the cosine of the angle between the tag $B$ meson and $D^{(*)}\ell$ system in the c.m. frame. Thus, for correctly reconstructed tag-side $B \to D^{(*)}\ell\nu$ decays, the right-hand side of Eq. (49) falls in the physical region such that $-1 \leq \cos\theta_{B,D^*\ell} \leq 1$ (with a tail toward negative values due to final state radiation). However, for incorrectly reconstructed tag-side decays such as $B \to D^{**}\ell\nu$ or semitauonic $B \to D^{(*)}\tau(\to \ell\nu\nu)\nu$ decays, the right-hand side of Eq. (49) will typically produce large negative values due to the absent term $(p_B - p_{D^{(*)}\ell})^2/2|\boldsymbol{p}_B||\boldsymbol{p}_{D^{(*)}\ell}| > 0$, which is needed for $\cos\theta_{B,D^{(*)}\ell}$ to represent a physical cosine: see Fig. 1 of Sato *et al.* (2016). Including finite resolution effects, a requirement of $\cos\theta_{B,D^*\ell} \in [-2, 1]$ thus captures most tag $B \to D^{(*)}\ell\nu$ decays while strongly suppressing $B \to D^{**}\ell\nu$ and $B \to D^{(*)}\tau(\to\ell\nu\bar{\nu})\nu$ decays.

On the signal side, lepton candidates are combined with $D$ and $D^*$ meson candidates. The decay modes used for the $D^0$ and $D^+$ candidates account for about 30% and 22%, respectively, of the overall decay branching fractions. To further improve the reconstruction, a decay vertex fit of the $D$ daughter particles is carried out. $D^{*+}$ candidates are reconstructed using both charged and neutral slow pion candidates, and neutral slow pion candidates and photons are used to build $D^{*0}$ candidates. The selection is refined by applying requirements on the masses of these candidates and other variables that are optimized to maximize the statistical significance of the final result. In case several tag- and signal-side candidates can be reconstructed, the candidate combination with the highest tagging classifier output from the FEI, and on the signal side the combination with the best $D$ vertex fit probability, is selected. Events with additional unassigned charged particles or displaced tracks are rejected. At this stage, all signal- and tag-side particles are identified and $E_{\mathrm{ECL}}$ can be reconstructed. Here only clusters in the barrel, forward region, and backward region with energies greater than 50, 100, and 150 MeV, respectively, are included. For correctly reconstructed normalization and signal decays, one expects no unassigned neutral depositions in the detector and also that $E_{\mathrm{ECL}}$ peaks at zero with a tail toward positive values due to reconstruction mistakes on the tag side, and to a lesser extent due to beam-background depositions and noise in the calorimeter.

To separate signal and normalization mode decays, a boosted decision tree is trained with the following distinguishing features, which are listed in order of importance:

- Signal-side $\cos\theta_{B,D^*\ell}$: for normalization mode decays this variable will be in the physical range of $[-1, 1]$, whereas for the signal mode large negative values are expected.
- Approximate missing mass squared $m_{\mathrm{miss}}^2$ (more details are given in Sec. III.C). The additional two neutrinos from the $\tau$ decay will produce on average a larger missing invariant mass than the normalization mode.
- The total visible energy $E_{\mathrm{vis}} = \sum_i E_i$ of all reconstructed particles $i$ in the event: the two additional neutrinos from the signal mode also will reduce the visible energy observed in the detector, in contrast to the normalization mode.

The classifier output $\mathcal{O}_{\mathrm{sig}}$ is then directly fitted along with the $E_{\mathrm{ECL}}$ of the event to disentangle signal, normalization, and background contributions. This is done by exploiting the isospin relations between the charged and neutral final states for the normalization and signal contributions, i.e., by fixing $\mathcal{R}(D^{(*)0}) = \mathcal{R}(D^{(*)+})$. The free parameters of the fit are the yields for the signal, normalization, $B \to D^{**}l\nu$, and feed-down from $D^{(*)}\ell$ components. The yields of other

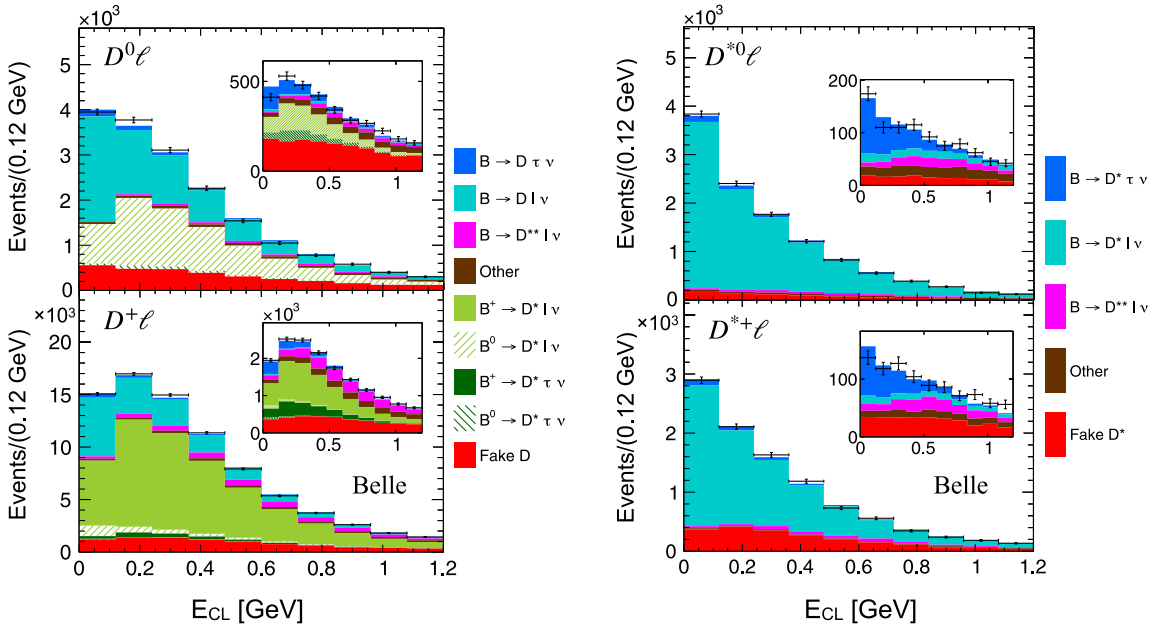


FIG. 13. Projection of the signal fit for the Belle measurement of $\mathcal{R}(D^{(*)})$ using semileptonic tagging. The four panels correspond to the four reconstruction categories: (top left panel) $D^0\ell$, (top right panel) $D^{*0}\ell$, (bottom left panel) $D^+\ell$, (bottom right panel) $D^{*+}\ell$. The signal-enriched regions, which were obtained using a cut on a multivariate classifier, are shown in the insets. The uncertainties are only statistical. Adapted from Caria *et al.*, 2020.

background contributions from continuum and $B$ meson decays are kept fixed to their expectation values.

Figure 13 shows the full postfit projections of $E_{\mathrm{ECL}}$ as well as those in the signal-enriched region of $\mathcal{O}_{\mathrm{sig}} > 0.9$. The final results are

$$\mathcal{R}(D) = 0.307 \pm 0.037(\mathrm{stat}) \pm 0.016(\mathrm{syst}), \quad (50)$$

$$\mathcal{R}(D^*) = 0.283 \pm 0.018(\mathrm{stat}) \pm 0.014(\mathrm{syst}), \quad (51)$$

with the first error being statistical and the second coming from systematic uncertainties, and an anticorrelation of $\rho = -0.52$ between the two values. The measurement is the most precise determination of these ratios to date and shows good compatibility with the SM expectation (Table I).

Table X summarizes the relative systematic and statistical uncertainties on $\mathcal{R}(D)$ and $\mathcal{R}(D^*)$. The limited size of the simulated sample, used to define the fit templates and to train the multivariate selection, results in the dominant systematic uncertainty. Uncertainties from lepton efficiencies and fake rates cancel to only a certain extent in the measured ratios because of the large differences in the momentum spectra of the signal and normalization decays. This leads to a sizable uncertainty of the efficiency ratios $\epsilon_{\mathrm{sig}}/\epsilon_{\mathrm{norm}}$. Uncertainties from the $B \to D^{**} l\nu$ background are less dominant.

### C. LHCb untagged measurements

The measurement of decays with multiple neutrinos in the final state is especially challenging at hadron colliders given the typically smaller signal-to-background ratios compared to the $B$ factories and the inability to effectively reconstruct a tag $b$ hadron to constrain the kinematics of the signal decay. These difficulties have been overcome by taking advantage of the large data samples of $b$ hadrons produced in high-energy $pp$ collisions and by cleverly estimating the kinematics of the signal $b$ hadron based on the particles that can be reconstructed. The measurements described in Secs. IV.C.1 and IV.C.3 make use of the relatively clean muonic decays of the $\tau$ lepton to limit the background contributions and estimate the $B$ or $B_c$ kinematics with the so-called rest-frame approximation (see Sec. III.C.3). The measurement detailed in Sec. IV.C.2 takes advantage of the additional vertex that can be reconstructed from $\tau \to \pi^-\pi^+\pi^-\nu$ hadronic decays not only to reduce hadronic backgrounds by 4 orders of magnitude but

TABLE X. Summary of the relative uncertainties for the Belle measurement of $\mathcal{R}(D^{(*)})$ using semileptonic tagging (Caria *et al.*, 2020).

| Result | Contribution | Uncertainty (%) Syst. | Stat. |
|---|---|---|---|
| $\mathcal{R}(D)$ | $B \to D^{**}\ell\bar{\nu}_\ell$ | 0.8 | |
| | PDF modeling | 4.4 | |
| | Other background | 2.0 | |
| | $\epsilon_{\mathrm{sig}}/\epsilon_{\mathrm{norm}}$ | 1.9 | |
| | **Total systematic** | **5.2** | |
| | **Total statistical** | | **12.1** |
| | **Total** | **13.1** | |
| $\mathcal{R}(D^*)$ | $B \to D^{**}\ell\bar{\nu}_\ell$ | 1.4 | |
| | PDF modeling | 2.3 | |
| | Other background | 1.4 | |
| | $\epsilon_{\mathrm{sig}}/\epsilon_{\mathrm{norm}}$ | 4.1 | |
| | **Total systematic** | **4.9** | |
| | **Total statistical** | | **6.4** |
| | **Total** | **8.1** | |

also to estimate the momentum of the signal $B$ meson relatively precisely; see Sec. III.C.2.

#### 1. $\mathcal{R}(D^{*+})$ with $\tau \to \mu\nu\bar{\nu}$

The LHCb experiment published the first measurement of a $b \to c\tau\nu$ transition in a hadron collider environment in 2015 (Aaij *et al.*, 2015c). This result was based on a 3 fb$^{-1}$ sample of $pp$ collision data and measured $\mathcal{R}(D^{*+})$, which under isospin symmetry has the same value as $\mathcal{R}(D^{*0})$ to a very good approximation. This first analysis chose to focus on $\mathcal{R}(D^*)$ over $\mathcal{R}(D)$ because the lower $B \to D\tau\nu$ branching fraction, the lack of a $D^*$ mass constraint, and the larger contributions from feed-down processes make $\mathcal{R}(D)$ a significantly more challenging observable to measure at a hadron collider. A combined $\mathcal{R}(D)$ and $\mathcal{R}(D^*)$ measurement from LHCb is expected in the near future.

Signal ($\bar{B}^0 \to D^{*+}\tau^-\bar{\nu}_\tau$) and normalization ($\bar{B}^0 \to D^{*+}\mu^-\bar{\nu}_\mu$) decays are selected by requiring that the trajectories of a $\mu^-$ and an oppositely charged $D^{*+}$ candidate, reconstructed exclusively via the decay chain $D^{*+} \to D^0(\to K^-\pi^+)\pi^+$, are consistent with a common vertex that is separated from the $pp$ PV. Events with an electron in the final state are not included because of the trigger and calorimeter limitations described in Sec. III.B. Compared to the $B$ factories, the reduction in signal reconstruction efficiency due to the exclusive use of muons and a single $D^0$ decay chain is compensated for by the far larger production cross section for $B$ mesons at LHCb.

An isolation BDT is trained to reject events arising from partially reconstructed $B$ decays. For each additional track in the event this algorithm evaluates the possibility that the track originates from the same vertex as the $D^{*+}\mu^-$ candidate based on quantities such as the track separation from the decay vertex and the angle between the track and the candidate momentum vector. The signal sample is made up of events where the $D^{*+}\mu^-$ candidate is found to be isolated from all other tracks in the event.

The isolation BDT is employed to further select three data control samples: a $D^{*+}\mu^-K^\pm$ sample that includes an additional kaon coming from the $D^{*+}\mu^-$ vertex, as well as the $D^{*+}\mu^-\pi^-$ and $D^{*+}\mu^-\pi^-\pi^+$ samples with an additional pion and pion pair, respectively. The $D^{*+}\mu^-K^\pm$ sample is enriched in double-charm decays of the type $\bar{B} \to D^{*+}H_cX$, where $H_c$ is a charmed hadron that decays semileptonically and $X$ refers to unreconstructed particles, while the samples with additional pions are enriched in $B \to D^{**}l\nu$ decays. Additional data control samples based on wrong charge combinations of the $D^{*+}$ and $D^{*+}$ decay products and muon are used to measure the combinatorial background. The misidentified muon background is estimated in a $D^{*+}h^\pm$ sample, where $h^\pm$ is a track that fails the muon identification requirements.

A three-dimensional binned maximum likelihood fit to the $q^2$, $m^2_{\text{miss}}$ [Eq. (44)], and $E^*_\ell$ [Eq. (45)] variables is performed to determine the signal, normalization, and background yields, as well as several parameters describing the shapes of the different distributions. The momentum of the $B$ meson, which is necessary to calculate the three fit variables, is estimated via the rest-frame approximation that is detailed in Sec. III.C.3.

The templates for the combinatorial and misidentified muon backgrounds are taken directly from the previously described data control samples, while the templates for the $\bar{B} \to D^{*+}H_cX$ and $B \to D^{**}l\nu$ backgrounds are based on Monte Carlo simulations with corrections extracted from a fit to the $D^{*+}\mu^-K^\pm$ and $D^{*+}\mu^-\pi^-(\pi^+)$ samples. Figure 14 shows the excellent agreement between the data and the resulting background model that is achieved.

The templates for the signal and normalization contributions are parameterized by CLN form factors (Sec. II.C.2) extracted from the fit to the signal sample. Figure 15 shows the fit projection of the $q^2$ variable in the full range, as well as the $m^2_{\text{miss}}$ and $E^*_\ell$ projections in the $q^2$ bin with the highest signal-to-background ratio.

As Table XI shows, the limited size of the simulated samples is the main source of systematic uncertainty in this

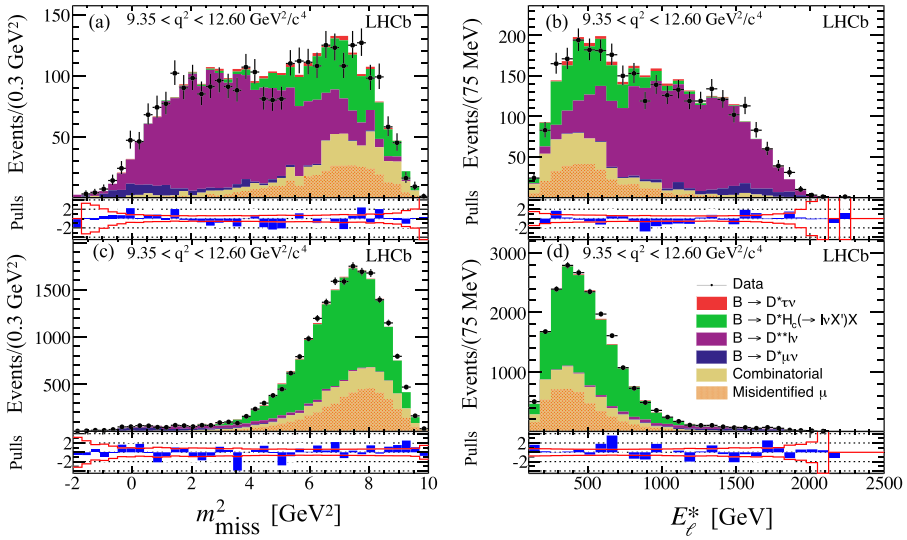


FIG. 14. Projections of the control sample fits in the highest $q^2$ bin for the LHCb measurement of $\mathcal{R}(D^{*+})$ involving muonic $\tau$ decays. (a),(b) $D^{*+}\mu^-\pi^-$ sample enriched in $B \to D^{**}l\nu$ decays and (c),(d) a $D^{*+}\mu^-K^\pm$ sample enriched in $\bar{B} \to D^{*+}H_cX$ decays. Adapted from Aaij *et al.*, 2015c.

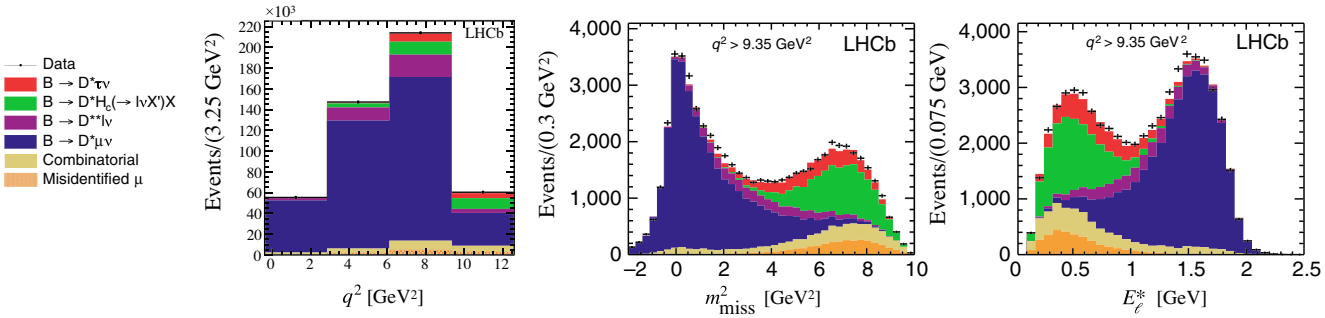


FIG. 15. Projections of the signal fit for the LHCb measurement of $\mathcal{R}(D^{*+})$ involving muonic $\tau$ decays (Aaij *et al.*, 2015c). Left panel: full $q^2$ projection. Middle panel: $m^2_{\rm miss}$ projection in the highest $q^2$ bin. Right panel: $E^*_\ell$ projection in the highest $q^2$ bin.

analysis, followed by the uncertainty in the background contributions and $B \to D^* l\nu$ templates. The overall systematic uncertainty is slightly larger than the statistical uncertainty, but as discussed in Sec. V many of the systematic uncertainties are expected to decrease commensurately with larger data samples. The result of this measurement is

$$\mathcal{R}(D^{*+}) = 0.336 \pm 0.027(\text{stat}) \pm 0.030(\text{syst}), \quad (52)$$

which is in good agreement with the previous measurements by the $B$ factories.

### 2. $\mathcal{R}(D^{*+})$ with $\tau \to \pi^-\pi^+\pi^-\nu$

Instead of a leptonic $\tau$ decay, the 2018 measurement of $\mathcal{R}(D^{*+})$ by LHCb (Aaij *et al.*, 2018b) employed the three-prong $\tau^- \to \pi^-\pi^+\pi^-\nu_\tau$ decay. This channel is interesting *a priori* because it is presently the only $\tau$ decay for which it is practical to reconstruct the $\tau$ decay vertex. This in turn provides good precision on the reconstruction of the $\bar{B}^0$ momentum, as described in Sec. III.C. Moreover, when aggregated with the $\tau^- \to \pi^-\pi^+\pi^-\pi^0\nu_\tau$ channel, the three-prong decays have a total branching fraction of 13.5%, which is comparable to that of the muonic decay channel, and the pion-triplet dynamics provides powerful discrimination against the largest background contributions.

TABLE XI. Summary of the relative uncertainties for the LHCb measurement of $\mathcal{R}(D^{*+})$ involving muonic $\tau$ decays (Aaij *et al.*, 2015c). FF stands for form factor.

| Contribution | Uncertainty (%) Syst. | Stat. |
|---|---|---|
| Simulated sample size | 6.2 | |
| Misidentified $\mu$ background | 4.8 | |
| $B \to D^{**} l\nu$ background | 2.1 | |
| $B \to D^* l\nu$ FFs | 1.9 | |
| Hardware trigger | 1.8 | |
| Double-charm background | 1.5 | |
| MC data correction | 1.2 | |
| Combinatorial background | 0.9 | |
| Particle ID | 0.9 | |
| **Total systematic** | **8.9** | |
| **Total statistical** | | **8.0** |
| **Total** | **12.0** | |

In this measurement, signal $\bar{B}^0 \to D^{*+}\tau^-\bar{\nu}_\tau$ decays are selected by requiring that the trajectories of a $\tau^-$ lepton and an oppositely charged $D^{*+}$ candidate, reconstructed exclusively via the decay chain $D^{*+} \to D^0(\to K^-\pi^+)\pi^+$, are consistent with a common vertex separated from the PV. The $\tau$ lepton is reconstructed by requiring that the tracks of three pions with the appropriate charges share a common vertex (Fig. 8, top panel). Since the final state does not contain any charged lepton, fully hadronic $\bar{B}^0 \to D^{*+}\pi^-\pi^+\pi^- X$ decays initially dominate the selected event sample. However, this background contribution may be reduced by 4 orders of magnitude by taking advantage of the long $\tau$ lifetime: the $\pi\pi\pi$ vertex in a signal decay is typically displaced downstream of the $B$ vertex. This allows one to distinguish such from the prompt topology of $\bar{B}^0 \to D^{*+}\pi^-\pi^+\pi^- X$ decays, in which the $\pi\pi\pi$ and the $\bar{B}^0$ vertices overlap, by requiring that the distance between the $\tau$ and the $B$ vertex positions along the beam axis is larger than 4 times its reconstructed uncertainty (Fig. 16). Additionally, strict isolation from other charged particles is required to reject charm decays with more than three charged daughters, as well as fake detached vertices where the $D^*$ meson and the three pions come from other $b$ hadrons present in the event.

One of the major challenges in hadronic-$\tau$ measurements is that the normalization ($\bar{B}^0 \to D^{*+}\mu^-\bar{\nu}_\mu$) decays are not

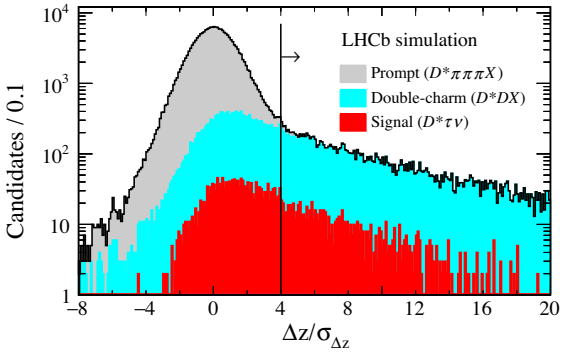


FIG. 16. Distribution of the distance between the $\bar{B}^0$ vertex and the $\tau$ vertex along the beam direction (Fig. 8, top panel) divided by its uncertainty in simulated events for the LHCb measurement of $\mathcal{R}(D^{*+})$ involving $\tau \to \pi^-\pi^+\pi^-\nu$ decays (Aaij *et al.*, 2018b). The vertical line shows the $4\sigma$ requirement used in the analysis to separate signal events in red (dark gray) from the prompt background component in medium gray.

measured simultaneously with the signal ($\bar{B}^0 \to D^{*+}\tau^-\bar{\nu}_\tau$) decays. Since absolute branching fraction measurements are exceedingly difficult at LHCb, this analysis normalizes the signal yield against that of the prompt $\bar{B}^0 \to D^{*+}\pi^-\pi^+\pi^-$ decay, which has the same particle content as the signal, and then relies on two external branching fractions to calculate $\mathcal{R}(D^*)$ via

$$\mathcal{R}(D^*) = \left.\frac{\mathcal{B}(\bar{B} \to D^*\tau\nu_\tau)}{\mathcal{B}(\bar{B} \to D^*\pi\pi\pi)}\right|_{\text{fit}} \times \left.\frac{\mathcal{B}(\bar{B} \to D^*\pi\pi\pi)}{\mathcal{B}(\bar{B} \to D^*\mu\nu_\mu)}\right|_{\text{ext}}. \quad (53)$$

After selecting events with large $\tau$ flight significance, as previously described, the dominant remaining background contributions consist of double-charm $B \to D^{*+}D_{(s)}^{(*,**)}$ decays. These decays were also the largest background contributions to the muonic-$\tau$ measurement of $\mathcal{R}(D^{*+})$, but their relative amount in $D$ and $D_s^+$ mesons are very different. Because of the large inclusive branching fraction of the $D_s^+$ meson to final states with three pions (about 30%) and the small rate to semileptonic final states, the double-charm background in the hadronic-$\tau$ sample contains 10 times more $D_s^+$ mesons than that for the muonic-$\tau$ sample. Interestingly, the $D_s^+$ inclusive three-pion modes proceed mainly from two-body and quasi-two-body decay channels involving $\eta$, $\eta'$, $\omega$, and $\phi$ mesons, which leads to significantly different three-pion kinematics with respect to those of the signal. That is, the $\tau \to \pi^-\pi^+\pi^-\nu$ decay is well described within resonance chiral theory (Ecker, Gasser, Leutwyler *et al.*, 1989; Ecker, Gasser, Pich, and de Rafael, 1989), which features chiral terms as well as single-resonance $\rho$ and double-resonance $a_1 \to \rho$ contributions (Shekhovtsova *et al.*, 2012; Nugent *et al.*, 2013), leading to prominent $\rho$ peaks in the distribution of both the minimum and maximum masses to the two $\pi^+\pi^-$ mass combinations: $\min(m_{\pi^+\pi^-})$ and $\max(m_{\pi^+\pi^-})$, respectively.

These kinematic differences are effectively exploited by a BDT that also includes other variables such as the energy measured in the electromagnetic calorimeter in a cone whose axis is defined by the three-pion momentum. The kinematics of the three-pion system in background $D^0$ and $D^+$ decays is more similar to that in signal decays because the inclusive $\pi\pi\pi$ final state from these two mesons is dominated by the $Ka_1$ channel (Zyla *et al.*, 2020). Some discrimination is still possible, however, due to the restricted phase space of this virtual $a_1$ meson.

Many of the $B$ branching fractions to double-charm final states are known with poor precision or have not yet been measured. The following data control samples are used to reduce the uncertainty due to the composition of these background contributions:

- A low-BDT sample enriched with inclusive $D_s^+$ decays constrains the composition of $B \to D^{*+}D_s^-X$ decays. The simulation is reweighted to match a fit to the $\min(m_{\pi^+\pi^-})$, $\max(m_{\pi^+\pi^-})$, $m_{\pi^+\pi^-\pi^+}$, and $m_{\pi^+\pi^+}$ distributions. These variables capture the combined dynamics of the various inclusive $D_s^+$ decay channels to three pions [Figs. 17(a)–17(d)].
- A highly pure $B \to D^{*+}D_s^-(\to\pi^-\pi^+\pi^-)X$ sample selected by imposing a requirement on $m_{\pi^+\pi^-\pi^+}$ around the $D_s^+$ mass. A template fit to the $m_{\pi^+\pi^-\pi^+}$ distribution is used to measure the relative fractions of $D_s^+$ mesons produced directly and from $D_s^*$ or $D_s^{**}$ decays. The shape of the $D_s^*$ broad peak depends on the degree of longitudinal polarization of the $D_s^*$ and was adjusted in the simulation to reproduce the data. These measurements are important since the $q^2$ distributions of these decays differ significantly from each other, as shown in Fig. 17(f).
- Clean $B \to D^{*+}D^0(\to K^-\pi^+\pi^-\pi^+)X$ and $B \to D^{*+}D^-(\to K^-\pi^+\pi^-)X$ samples selected by explicitly reconstructing the $D^0$ and $D^-$ mesons. These samples are used to monitor and understand the non-$D_s^+$ background composition.

A three-dimensional binned maximum likelihood fit to $q^2$, the BDT output, and the decay time of the reconstructed $\tau$ is performed to determine the signal and background yields.

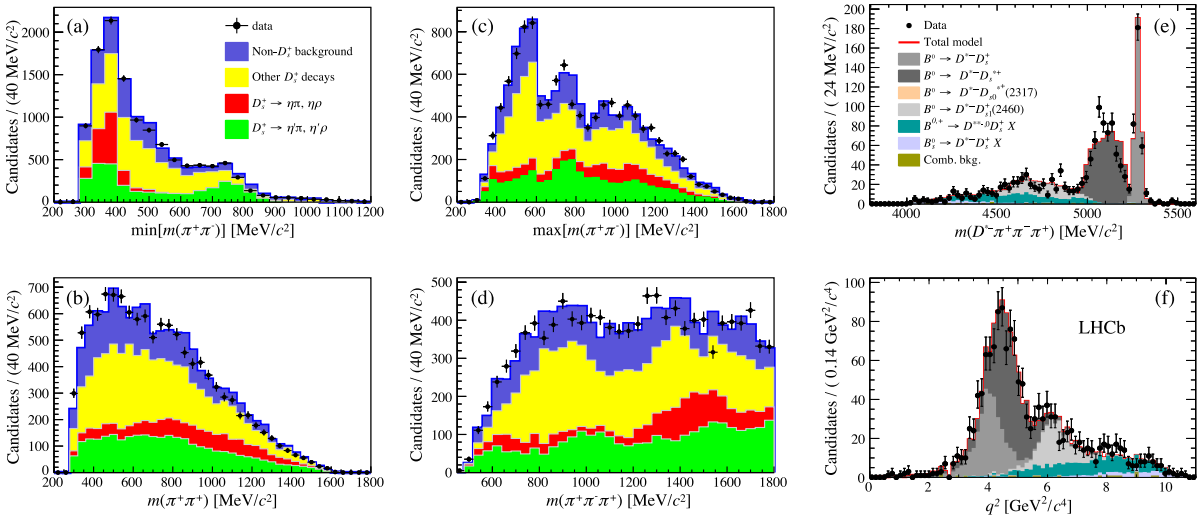


FIG. 17. Control sample fits for the LHCb measurement of $\mathcal{R}(D^{*+})$ involving $\tau \to \pi^-\pi^+\pi^-\nu$ decays (Aaij *et al.*, 2018b) employed to evaluate the composition of the various double-charm background contributions. (a)–(d) Low-BDT sample. (e),(f) $B \to D^{*+}D_s^-(\to \pi^-\pi^+\pi^-)X$ sample.

The calculation of $q^2$ relies on the $B$ momentum determination described in Sec. III.C.2. The decay time of the reconstructed $\tau$ ($t_\tau$) is computed from its flight distance and momentum obtained by the partial kinematic reconstruction. This variable is useful for separating $\tau$ from $D^-$ decays since the lifetime of the $D^-$ meson is 3.5 times longer than that of the $\tau$ lepton. The fit results for the LHC Run 1 data sample, corresponding to a luminosity of 3 fb$^{-1}$, are displayed in Fig. 18. An interesting feature of this method relative to the muonic-$\tau$ measurement is that the highest BDT output bin provides a fairly clean sample of signal decays with a purity of about 40%.

As shown in Table XII, the uncertainties related to the double-charm background and the limited size of the simulated samples are the dominant systematic uncertainties in this measurement. The uncertainties due to the limited knowledge of external branching fractions in Eq. (53), currently 4.6%, are worth mentioning because, unlike many of the other systematic uncertainties, these will not be reduced with the increasing LHCb data samples that will be collected. Instead, additional measurements from Belle II will be needed (Sec. V.E).

The result of this measurement was reported as $\mathcal{R}(D^{*+}) = 0.291 \pm 0.019 \pm 0.026 \pm 0.013$ in 2018. When one takes into account the latest HFLAV average of $\mathcal{B}(B^0 \to D^{*+}\ell\nu) = 5.08 \pm 0.02 \pm 0.12)\%$ (Amhis *et al.*, 2019), the result is

$$\mathcal{R}(D^{*+}) = 0.280 \pm 0.018(\text{stat}) \pm 0.025(\text{syst}) \pm 0.013, \qquad (54)$$

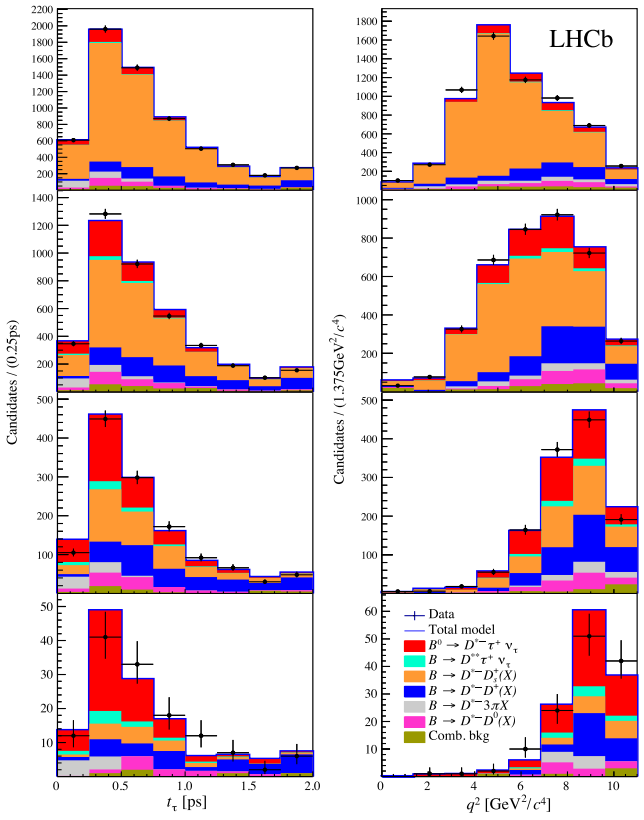


FIG. 18. Projections of the signal fit for the LHCb measurement of $\mathcal{R}(D^{*+})$ involving $\tau \to \pi^-\pi^+\pi^-\nu$ decays (Aaij *et al.*, 2018b). The four rows correspond to the four BDT bins for increasing values of the BDT response.

TABLE XII. Summary of the relative uncertainties for the LHCb measurement of $\mathcal{R}(D^{*+})$ involving $\tau \to \pi^-\pi^+\pi^-\nu$ decays (Aaij *et al.*, 2018b).

| Contribution | Uncertainty (%) Syst. | External | Stat. |
|---|---|---|---|
| Double-charm background | 5.4 | | |
| Simulated sample size | 4.9 | | |
| Corrections to simulation | 3.0 | | |
| $B \to D^{**}l\nu$ background | 2.7 | | |
| Normalization yield | 2.2 | | |
| Trigger | 1.6 | | |
| PID | 1.3 | | |
| Signal FFs | 1.2 | | |
| Combinatorial background | 0.7 | | |
| Modeling of $\tau$ decay | 0.4 | | |
| **Total systematic** | **9.1** | | |
| $\mathcal{B}(B \to D^*\pi\pi\pi)$ | | 3.9 | |
| $\mathcal{B}(B \to D^*\ell\nu)$ | | 2.3 | |
| $\mathcal{B}(\tau^+ \to 3\pi\nu)/\mathcal{B}(\tau^+ \to 3\pi\pi^0\nu)$ | | 0.7 | |
| **Total external** | | **4.6** | |
| **Total statistical** | | | **6.5** |
| **Total** | | **12.0** | |

where the third uncertainty is due to the aforementioned external branching fractions.

### 3. $\mathcal{R}(J/\psi)$ with $\tau \to \mu\nu\bar{\nu}$

The ratio $\mathcal{R}(J/\psi)$ was measured for the first time in 2018 by the LHCb experiment (Aaij *et al.*, 2018a), thus opening the possibility for the exploration of LFUV in decays subject to very different sources of both experimental and theoretical uncertainties compared to those in $\mathcal{R}(D^{(*)})$. This measurement leverages two of the key techniques developed for the muonic $\mathcal{R}(D^{*+})$ analysis described in Sec. IV.C.1: the isolation BDT and the rest-frame approximation. Just as for the $\mathcal{R}(D^{*+})$ measurement, the $\tau$ lepton is reconstructed via $\tau \to \mu\nu\bar{\nu}$ so that signal $B_c \to J/\psi\tau\nu$ and normalization $B_c \to J/\psi\mu\nu$ decays share the same final state. The event is selected if the only additional tracks close to the muon coming from the $\tau$ decay are a pair of oppositely charged muons that form a vertex separated from the PV and whose invariant mass is compatible with the $J/\psi \to \mu\mu$ decay.

The signal and normalization yields are extracted from a four-dimensional binned maximum likelihood fit to $q^2$, $m^2_{\text{miss}}$, $E^*_\ell$, and the proper time elapsed between the production and decay of the $B_c$ meson: the decay time. The first three variables are calculated with the same techniques as used in the muonic $\mathcal{R}(D^{*+})$ analysis (Sec. IV.C.1). The inclusion of the decay time among the fit variables improves the separation of $B_c$ decays from $B_{u,d,s}$ decays because the $B_c$ lifetime is almost 3 times shorter than that of the $B_{u,d,s}$ mesons.

A key difference with respect to the $\mathcal{R}(D^{(*)})$ measurements is that background contributions from partially reconstructed $B_c$ decays are significantly reduced thanks to the narrow invariant mass of the $J/\psi$ meson and its clean dimuon final state. As a result of this reduction and the overall small $B_c$ production rate, the main sources of background in the $\mathcal{R}(J/\psi)$ analysis are misidentified $H_b \to J/\psi h^+$ decays, where $H_b$ is a more abundant $b$ hadron and $h^+$ is a hadron

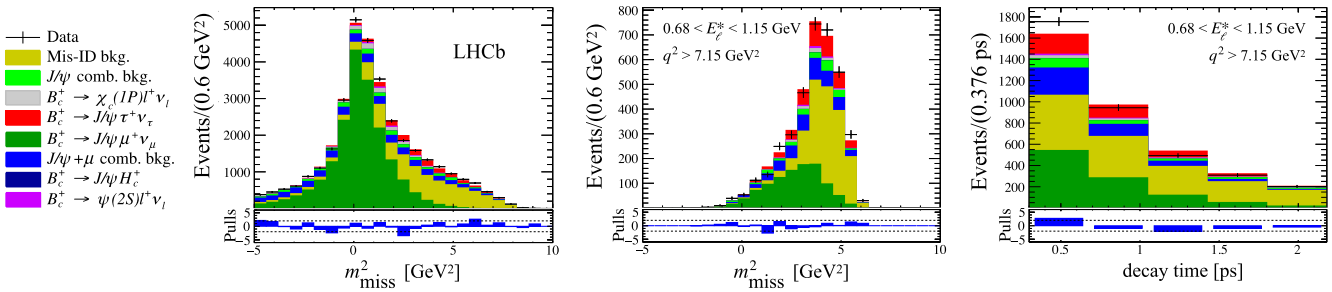


FIG. 19. Projections of the signal fit for the LHCb muonic measurement of $\mathcal{R}(J/\psi)$ (Aaij *et al.*, 2018a). Left panel: full $m^2_{\rm miss}$ projection. Middle panel: $m^2_{\rm miss}$ projection in the highest $q^2$ and lowest $E^*_\ell$ bins. Right panel: decay time projection in the highest $q^2$ and lowest $E^*_\ell$ bins.

incorrectly identified as a muon, as well as random combinations of muons.

The template for the $J/\psi h^+$ contribution is estimated by applying the misidentification probabilities for different hadron species, as determined in high-purity samples of identified hadrons, to a control sample with a $J/\psi$ and an additional track that fails the muon identification. This template is treated as free floating in the signal fit. The combinatorial backgrounds are estimated in the sidebands of the $B_c$ mass and the $J/\psi$ masses, $m(J/\psi\mu) > 6.4$ GeV and $3150 < m(\mu^+\mu^-) < 3190$ MeV, respectively. The small contributions from higher-mass $B_c^- \to \psi(2S)\ell^-\bar{\nu}_\ell$ and $B_c^- \to \chi_c(1P)\ell^-\bar{\nu}_\ell$ are extracted from the fit with templates taken from MC simulation.

Figure 19 shows the fit projections for $m^2_{\rm miss}$ over the full range, as well as $m^2_{\rm miss}$ and the $B_c$ decay time in the $E^*_\ell$ and $q^2$ ranges with the highest signal-to-background ratio. The agreement is good overall, and a small but significant signal contribution at high $m^2_{\rm miss}$ and low decay times can be observed.

Table XIII summarizes the sources of uncertainty in this measurement. The leading contribution comes from the $B_c \to J/\psi l\nu$ decay form factors, which have not yet been measured and had to be determined in the signal fit itself. As discussed in Sec. II.E, HQET cannot be used to describe a decay with a heavy spectator quark. As a result, at the time of publication of this measurement only quark model predictions, untested by experiment, were available. The recent results of lattice calculations will reduce this uncertainty substantially. Sizable uncertainties also arise due to the limited size of the simulated samples and the fit model. These are also expected to be reduced in future measurements.

TABLE XIII. Summary of the relative uncertainties for the LHCb muonic measurement of $\mathcal{R}(J/\psi)$ (Aaij *et al.*, 2018a).

| Contribution | Uncertainty (%) Syst. | Stat. |
|---|---|---|
| Signal and normalization FFs | 17.0 | |
| Simulated sample size | 11.3 | |
| Fit model | 11.2 | |
| Misidentified $\mu$ background | 7.9 | |
| Partial $B_c$ background | 6.9 | |
| Combinatorial background | 6.5 | |
| $\epsilon_{\rm sig}/\epsilon_{\rm norm}$ | 0.9 | |
| **Total systematic** | **25.4** | |
| **Total statistical** | | **23.9** |
| **Total** | **34.9** | |

The result of this measurement is

$$\mathcal{R}(J/\psi) = 0.71 \pm 0.17(\text{stat}) \pm 0.18(\text{syst}), \tag{55}$$

which lies within 2 standard deviations of the SM prediction in Eq. (34).

### D. Belle polarization measurements

#### 1. $\tau$ polarization with $\tau \to \pi\nu$ and $\tau \to \rho\nu$

The Belle experiment measured (Hirose *et al.*, 2017, 2018) the $\tau$ polarization fraction $P_\tau(D^*)$ introduced in Sec. II.D.2. The analysis strategy is similar to that of the hadronic tag measurements of $B \to D^*\tau\nu$ decays (Lees *et al.*, 2012, 2013; Huschle *et al.*, 2015) but reconstructs the $\tau$ lepton in the hadronic one-prong $\tau \to \pi\nu$ and $\tau \to \rho\nu$ modes. For these final states, the helicity angle $\cos\theta_h$ can be explicitly reconstructed by taking advantage of the fully reconstructed tag-side $B$ meson to boost the visible $\tau$ daughter particles into the center-of-mass frame of the $\tau\bar{\nu}_\tau$ lepton pair whose four-momentum

$$q = p_{e^+e^-} - p_{B_{\rm tag}} - p_{D^*}. \tag{56}$$

The terms on the right-hand side of Eq. (56) are the momenta of the colliding $e^+e^-$ pair, the reconstructed tag-side $B$ meson, and the reconstructed $D^*$ candidate, respectively. In the $\tau\bar{\nu}_\tau$ center-of-mass frame, the $\tau$ energy and momentum magnitude are fully determined by $q^2$ and the $\tau$ lepton mass $m_\tau$ as follows:

$$E_\tau = \frac{q^2 + m_\tau^2}{2\sqrt{q^2}}, \qquad |\vec{p}_\tau| = \frac{q^2 - m_\tau^2}{2\sqrt{q^2}}. \tag{57}$$

In this frame, the cosine of the angle between the spatial momenta of the $\tau$ lepton and its daughter meson $h$ is

$$\cos\theta_{\tau h} = \frac{2E_\tau E_h - m_\tau^2 - m_h^2}{2|\vec{p}_\tau||\vec{p}_h|}, \tag{58}$$

in which $E_h$ and $|\vec{p}_h|$ are the daughter meson energy and absolute spatial momentum, respectively. By applying a boost

into the $\tau$ rest frame, one can then express the cosine of the helicity angle as

$$\cos\theta_h = \frac{1}{|\vec{p}_h^{\,\tau}|}(\gamma|\vec{p}_h|\cos\theta_{\tau h} - \gamma\beta E_h). \tag{59}$$

In Eq. (59) $\gamma = E_\tau/m_\tau$, $\beta = |\vec{p}_\tau|/E_\tau$, and $|\vec{p}_h^{\,\tau}| = (m_\tau^2 - m_h^2)/2m_\tau$ denotes the absolute daughter meson spatial momentum in the $\tau$ rest frame.

To reduce backgrounds, only candidates with $q^2 > 4$ GeV$^2$ and with a physical value of $\cos\theta_h \in [-1, 1]$ are retained. Unassigned neutral energy depositions fulfilling photon-energy reconstruction criteria are summed to reconstruct $E_{\rm ECL}$ and only candidates with $E_{\rm ECL} < 1.5$ GeV are retained. In order not to be dependent on the $B_{\rm tag}$ reconstruction, whose efficiency likely differs between data and simulation, the measured signal event yields are normalized to $B \to D^*\ell\nu$ events. These can be identified and separated from background processes using $m^2_{\rm miss}$; cf. Sec. III.C. For both signal and normalization candidates, events with additional charged tracks or $\pi^0$ candidates are rejected.

The observables $\mathcal{R}(D^*)$ and $P_\tau(D^*)$ are extracted from a fit to the $E_{\rm ECL}$ distribution in two bins of $\cos\theta_h$: $[-1, 0]$ and $[0, 1]$. This fit is performed simultaneously on the two $\tau$ decay samples, $\tau \to \pi\nu$ and $\tau \to \rho\nu$. The free parameters in the fit include the yields for the $B \to D^*\tau\nu$, $B \to D^*\ell\nu$, $B \to D^{**}l\nu$, continuum, and fake $D^*$ contributions, among others. Figure 20 shows the fitted $E_{\rm ECL}$ distribution for all the reconstructed modes combined together. The fitted signal yields are then converted into measurements of $\mathcal{R}(D^*)$ and $P_\tau(D^*)$ with

$$\mathcal{R}(D^*) = \frac{1}{\mathcal{B}(\tau \to h\nu)}\frac{\epsilon_{\rm norm}}{\epsilon_{\rm sig}}\frac{N_{\rm sig}}{N_{\rm norm}}, \tag{60}$$

$$P_\tau(D^*) = \frac{2}{\alpha}\frac{N_{\rm sig}^{\cos\theta_h>0} - N_{\rm sig}^{\cos\theta_h<0}}{N_{\rm sig}^{\cos\theta_h>0} + N_{\rm sig}^{\cos\theta_h<0}}, \tag{61}$$

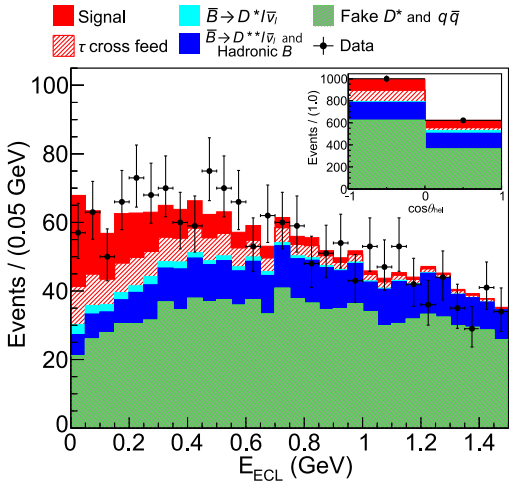


FIG. 20. Signal fit for the measurement of the $\tau$ polarization fraction $P_\tau(D^*)$ by Belle (Hirose *et al.*, 2017). The fits to the neutral and charged $B$ candidates as well as the $\tau \to \pi\nu$ and $\tau \to \rho\nu$ decay modes and the two $\cos\theta_h$ bins are combined.

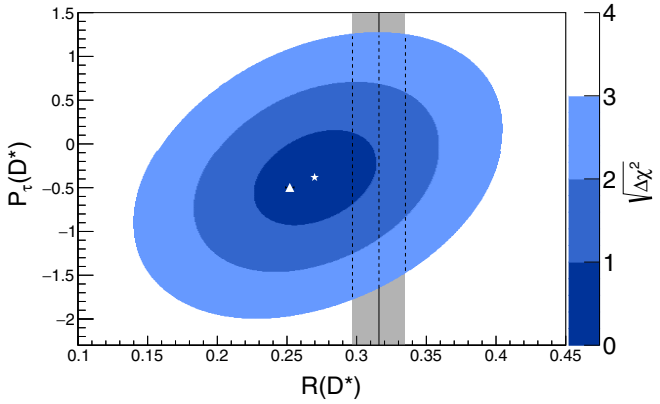


FIG. 21. Values of $\mathcal{R}(D^*)$ and $P_\tau(D^*)$ (white star) and the $1\sigma$, $2\sigma$, and $3\sigma$ contours as measured by Belle (Hirose *et al.*, 2017). The SM expectations (Tanaka and Watanabe, 2013; Amhis *et al.*, 2019) are shown as a white triangle. The gray band shows the then-world-average measurement of $\mathcal{R}(D^*)$.

with $\alpha$ a factor that accounts for the sensitivity on the polarization and efficiency differences of both channels. The obtained values are

$$R(D^*) = 0.270 \pm 0.035(\text{stat})^{+0.028}_{-0.025}(\text{syst}), \tag{62}$$

$$P_\tau(D^*) = -0.38 \pm 0.51(\text{stat})^{+0.21}_{-0.16}(\text{syst}), \tag{63}$$

with a total correlation including systematic uncertainties of $\rho = 0.33$. These results are in good agreement with the SM expectations, as shown in Fig. 21. A summary of the uncertainties on these measurements can be found in Table XIV. The largest systematic uncertainties stem from the composition of the hadronic $B$ meson background and the limited size of the simulated samples used to determine the fit PDFs.

### 2. $D^*$ polarization with inclusive tagging

In Abdesselam *et al.* (2019), the Belle experiment reported a first preliminary measurement of the longitudinal $D^*$ polarization fraction $F_{L,l}(D^*)$ (see Sec. II.D.2) based on

TABLE XIV. Summary of the relative uncertainties for Belle's hadronic tag measurement of $\mathcal{R}(D^*)$ and $P_\tau(D^*)$ (Hirose *et al.*, 2017, 2018).

| Result | Contribution | Uncertainty (%) Syst. | Stat. |
|---|---|---|---|
| $\mathcal{R}(D^*)$ | $B \to D^{**}\ell\bar{\nu}_\ell$ | 2.4 | |
| | PDF modeling | 3.4 | |
| | Other background | 8.4 | |
| | $\epsilon_{\rm sig}/\epsilon_{\rm norm}$ | 3.2 | |
| | **Total systematic** | **9.9** | |
| | **Total statistical** | | **12.9** |
| | **Total** | **16.3** | |
| $P_\tau(D^*)$ | PDF modeling | 33 | |
| | Other background | 31 | |
| | **Total systematic** | **48** | |
| | **Total statistical** | | **134** |
| | **Total** | **143** | |

inclusively tagged events (Sec. III.C.1). First, a viable $B^0 \to D^{*-}\tau^+\nu_\tau$ signal candidate with $\tau \to \ell\nu\bar{\nu}$ or $\tau \to \pi\nu$ and $D^{*-} \to \bar{D}^0\pi^-$ is reconstructed. The $\bar{D}^0$ meson is reconstructed in $\bar{D}^0 \to K^+\pi^-$, $\bar{D}^0 \to K^+\pi^-\pi^0$, and $\bar{D}^0 \to K^+\pi^+\pi^-\pi^-$ modes. Thereafter, no explicit reconstruction is attempted of the other (tag) $B$ meson produced in the $e^+e^-$ collision. Instead, an inclusive reconstruction approach that sums over all unassigned charged particles and neutral energy depositions above a certain energy threshold in the calorimeter is employed. Compared to hadronic or semileptonic tagging, this approach has the benefit of a higher reconstruction efficiency, as it does not rely on the correct identification of the decay cascades, but results in a poorer $B$ momentum resolution.

The tag side is required to be compatible with a well-reconstructed $B$ meson by requiring

$$M_{\rm tag} = \sqrt{E_{\rm beam}^2 - |\mathbf{p}_{\rm tag}|^2} > 5.2 \text{ GeV} \tag{64}$$

and $-0.30 < E_{\rm tag} - E_{\rm beam} < 0.05$ GeV, where $E_{\rm beam} = \sqrt{s}/2$ is the energy of each of the colliding $e^+e^-$ beams in the c.m. frame.

The sizable background contributions are suppressed with the signal-side normalized variable

$$X_{\rm miss} = \frac{E_{\rm miss} - |\mathbf{p}_{D^*} + \mathbf{p}_{d_\tau}|}{\sqrt{E_{\rm beam}^2 - m_{B^0}^2}}, \tag{65}$$

where $E_{\rm miss} = E_{\rm beam} - (E_{D^*} + E_{d_\tau})$ and $d_\tau$ refers to the visible $\tau$ daughter. Events with one neutrino have values of $X_{\rm miss}$ in the range $[-1, 1]$, while events with multiple undetected particles tend to take larger values. The analysis optimizes the signal significance by requiring $X_{\rm miss}$ to be larger than 1.5 or 1 for the $\tau \to \ell\nu\bar{\nu}$ and $\tau \to \pi\nu$ decay modes, respectively.

The helicity angle $\theta_v$ is defined as the angle between the reconstructed $\bar{D}^0$ and the direction opposite to the $B^0$ meson in the $D^{*-}$ frame (see the definition in Fig. 1; the Belle analysis uses the notation $\theta_{\rm hel}$). Because of the low $D^*$ reconstruction efficiency for $\cos\theta_v > 0$, the analysis focuses on the $-1 \le \cos\theta_v \le 0$ range. The signal yields are extracted in three bins of $\cos\theta_v$ from fits to the $M_{\rm tag}$ distribution; see Fig. 22 for an example. Most backgrounds do not peak in this variable, with the exception of semileptonic decays into light leptons. The yields for these peaking contributions are determined in the sidebands of kinematic variables. The $D^*$ polarization fraction is determined by a fit to the signal yields as a function of $\cos\theta_v$. Given the size of the $\cos\theta_v$ bins, resolution effects are assumed to be negligible. Figure 23 shows the measured helicity angle distribution, corrected for acceptance effects. The resulting fitted value for the longitudinal $D^*$ polarization fraction is

$$F_{L,\tau}(D^*) = 0.60 \pm 0.08(\text{stat}) \pm 0.04(\text{syst}), \tag{66}$$

with its uncertainty dominated by the limited size of the data sample. The largest systematic uncertainty in this measurement stems from the signal and nonresonant background

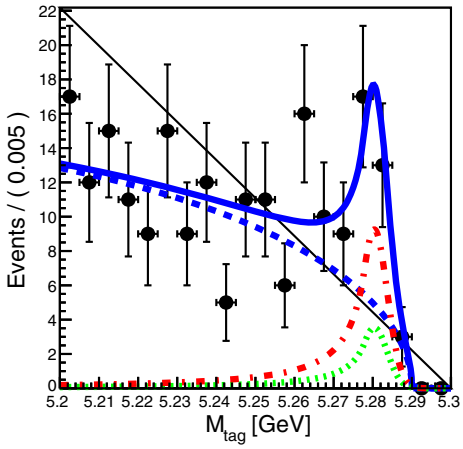


FIG. 22. Signal fit to the lowest $\cos\theta_v$ bin, $[-1, -0.67]$, in the $\bar{D}^0 \to K^+\pi^-\pi^0$ channel for the measurement of the longitudinal $D^*$ polarization fraction by Belle (Abdesselam *et al.*, 2019). The red (gray dash-dotted) curve corresponds to the signal contribution, and the blue (dark gray dashed) and green (light gray dotted) curves display the nonresonant and resonant background contributions, respectively.

shapes used in the $M_{\rm tag}$ fits, followed by the uncertainty on the modeling of $B \to D^{**}\tau\nu$ decays.

This result agrees with the SM prediction of $F_{L,\tau}(D^*)_{\rm SM} = 0.455(6)$ (Sec. II.D.2; from an arithmetic average of the various SM predictions) at the $1.6\sigma$ level. An important control measurement is the $D^*$ polarization of the light-lepton states, $F_{L,\ell}(D^*) = 0.56 \pm 0.02$ (statistical uncertainty only), which is in agreement with the prediction of $F_{L,\ell}(D^*)^{\rm BLPR}_{\rm SM} = 0.517(5)$ within 2.1 standard deviations.

## V. COMMON SYSTEMATIC UNCERTAINTIES AND FUTURE PROSPECTS

The different measurements of $\mathcal{R}(D^{(*)})$ thus far are fairly independent of each other because their uncertainties are

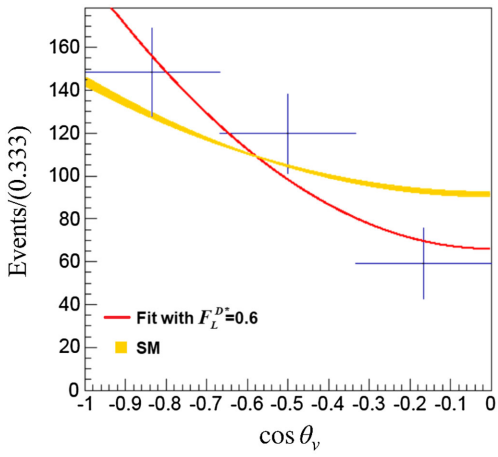


FIG. 23. Measured $\cos\theta_v$ distribution in $B^0 \to D^{*-}\tau^+\nu_\tau$ decays for the determination of the longitudinal $D^*$ polarization fraction by Belle. The red (dark gray) solid curve shows the best fit of the longitudinal polarization fraction and the yellow (light gray) band corresponds to the SM expectation (Huang *et al.*, 2018). Adapted from Abdesselam *et al.*, 2019.

TABLE XV. Summary of the uncertainties on the $\mathcal{R}(D^{(*)})$ measurements. The "other background" column primarily includes contributions from $DD$ and combinatorial backgrounds. The "other sources" column is dominated by particle identification and external branching fraction uncertainties.

| | | | | Systematic uncertainty (%) | | | | | Total uncertainty (%) | | |
|---|---|---|---|---|---|---|---|---|---|---|---|
| Result | Experiment | $\tau$ decay | Tag | MC stats | $D^{(*)}l\nu$ | $D^{**}l\nu$ | Other background | Other sources | **Syst.** | **Stat.** | **Total** |
| $\mathcal{R}(D)$ | *BABAR*[a] | $\ell\nu\nu$ | Hadronic | 5.7 | 2.5 | 5.8 | 3.9 | 0.9 | **9.6** | **13.1** | **16.2** |
| | Belle[b] | $\ell\nu\nu$ | Semileptonic | 4.4 | 0.7 | 0.8 | 1.7 | 3.4 | **5.2** | **12.1** | **13.1** |
| | Belle[c] | $\ell\nu\nu$ | Hadronic | 4.4 | 3.3 | 4.4 | 0.7 | 0.5 | **7.1** | **17.1** | **18.5** |
| $\mathcal{R}(D^*)$ | *BABAR*[a] | $\ell\nu\nu$ | Hadronic | 2.8 | 1.0 | 3.7 | 2.3 | 0.9 | **5.6** | **7.1** | **9.0** |
| | Belle[b] | $\ell\nu\nu$ | Semileptonic | 2.3 | 0.3 | 1.4 | 0.5 | 4.7 | **4.9** | **6.4** | **8.1** |
| | Belle[c] | $\ell\nu\nu$ | Hadronic | 3.6 | 1.3 | 3.4 | 0.7 | 0.5 | **5.2** | **13.0** | **14.0** |
| | Belle[d] | $\pi\nu$, $\rho\nu$ | Hadronic | 3.5 | 2.3 | 2.4 | 8.1 | 2.9 | **9.9** | **13.0** | **16.3** |
| | LHCb[e] | $\pi\pi\pi(\pi^0)\nu$ | ⋯ | 4.9 | 4.0 | 2.7 | 5.4 | 4.8 | **10.2** | **6.5** | **12.0** |
| | LHCb[f] | $\mu\nu\nu$ | ⋯ | 6.3 | 2.2 | 2.1 | 5.1 | 2.0 | **8.9** | **8.0** | **12.0** |

[a]See Lees *et al.* (2012, 2013).
[b]See Caria *et al.* (2020).
[c]See Huschle *et al.* (2015).
[d]See Hirose *et al.* (2018).
[e]See Aaij *et al.* (2018b).
[f]See Aaij *et al.* (2015c).

dominated by the limited size of the data and the simulation samples. However, over the next decade and a half, Belle II and LHCb will collect data samples 50 to 200 times larger than those used for the present measurements of $\mathcal{R}(D^{(*)})$ (Table III), so the relative impact of other systematic uncertainties will increase. Some of these uncertainties are due to aspects of the experimental analysis that are shared among all measurements, and can therefore lead to common systematic uncertainties. As a result, the combination of the measurements will entail a more complex treatment of these uncertainties. Table XV and Secs. V.A–V.F describe the main sources of systematic uncertainty in the measurement of $\mathcal{R}(D^{(*)})$ and the level of commonality among the various approaches.[9]

We also discuss in Secs. V.A–V.F the future prospects to reduce the total uncertainty in $\mathcal{R}(D^{(*)})$, as well as in LFUV ratios in many other decay modes, down to a few percent or less. In particular, reducing the systematic uncertainties commensurately with the statistical uncertainties will require meeting key challenges in computation, the modeling of $b$-hadron semileptonic decays, and background estimation in the years to come.

### A. Monte Carlo simulation samples

Table XV shows that one of the principal sources of uncertainty in the $\mathcal{R}(D^{(*)})$ measurements arises from the limited size of the simulation samples. This limitation results in large uncertainties through two different but parallel considerations: First, $B \to D^{(*)}l\nu$ decays have some of the largest $B$ branching fractions, necessitating enormous simulation samples to acceptably model the data. Such uncertainties, however, are statistical in nature and thus independent among different experimental analyses.

Second, semitauonic decays involve final states with multiple neutrinos, which escape detection. As a result, the reconstructed kinematic distributions employed to separate signal from background events are broad and difficult to describe analytically. Instead, experiments rely upon Monte Carlo simulations to derive the templates that are used in the signal extraction fit. Because of the broad nature of these distributions, multiple dimensions are necessary to disentangle the various contributions, which results in the simulated events being widely distributed among the numerous bins in the templates.

Monte Carlo–based uncertainties can be reduced simply by producing more simulated events. However, given the size of future data samples, it will be both a time and a cost challenge to continue producing simulated events in sufficient numbers such that these uncertainties remain controlled. Thus, different solutions will need to be considered. At present the most promising approaches are as follows:

(i) *Hardware*.—The high-energy physics (HEP) community has historically relied upon the exponential increase in computing throughput for relatively stable investments. As this exponential growth slows, either greater funding will have to be found or new avenues will need to be explored to keep up. Monte Carlo simulations are highly parallelizable, which makes them a favorable target for graphics processing unit (GPU) computation. Efforts to make increasing use of GPUs are under way, and expertise and appropriate tools will have to be further developed by the HEP community to ensure the widespread adoption of GPUs and reaping of their benefits.

[9]Note that, while some uncertainties are multiplicative, i.e., they scale with the resulting central value (such as uncertainties on the signal efficiency), the majority of the uncertainty is additive (such as uncertainties associated with the background subtraction or signal shapes). As a result, changes in the central values would alter the value of the uncertainty when expressed as a percentage. However, given that the overall uncertainty has become smaller than 20% and that the central values are starting to converge (see Fig. 25), the presentation of uncertainties as percentages should give a broadly accurate representation of the uncertainties and allow for comparisons across different measurements.

(ii) *Fast simulation (FastSim).*—The most resource intensive step in the generation of simulated events is the simulation of the detector response. Several procedures have been developed and are already in use that accelerate this step by simulating only parts of the detectors, or parametrizing its response; see the examples given by de Favereau *et al.* (2014) and Müller *et al.* (2018). New machine learning techniques such as generative adversarial networks may be able to further optimize this aspect of event simulation. See, for example, Vallecorsa (2018) and Erdmann, Glombitza, and Quast (2019) for proof-of-concept studies.

(iii) *Aggressive generator-level selections.*—These can help reduce the number of events that need to be fully simulated. Fiducial selections are already widely applied, but as data become abundant and the computing resources are stretched thin, analyses may have to start focusing on reduced regions of phase space with an even better signal-to-noise ratio. The generator-level selections would then have to be adjusted as closely as possible to these reduced areas to maximize the physics output of the simulation. For Belle II an attractive option to increase the size of simulated samples in analyses that use hadronic tagging would be to generate only the low branching fraction modes actually targeted by the tagging algorithms. See, for example, Kahn (2019) for a proof-of-concept implementation using generative adversarial networks.

Note that none of these approaches alone will be sufficient to cover all future needs. For instance, the FastSim implementations currently employed at LHCb allow for simulated events to be produced with about 10 times fewer resources than those with full simulation. However, this order of magnitude improvement covers only the increased needs from Run 1 (3.1 $\text{fb}^{-1}$) to Run 2 (6 $\text{fb}^{-1}$, twice the $b\bar{b}$ cross section and higher efficiency than in Run 1). Meeting the needs for the 50 $\text{ab}^{-1}$ that will be collected by Belle II, or the 300 $\text{fb}^{-1}$ by LHCb, will probably involve the combined use of the previously listed approaches (and perhaps others).

### B. Modeling of $B \to D^{(*)} l\nu$

As discussed in Sec. II, the predominant theoretical uncertainties in the modeling of $b \to c\tau\nu$ decays arise in the description of their hadronic matrix elements. Precision parametrizations of these matrix elements are currently achieved either by data-driven model-independent approaches, such as fits to HQET-based parametrizations (Sec. II.C.2), or by lattice QCD results (Sec. II.C.5), or by a combination of the two. This applies to predictions for both the ground states and the excited states (Sec. II.E) that often dominate background contributions. In the case of $B \to D^{(*)}\ell\nu$, these approaches have led to form factor determinations whose uncertainties contribute only at the 1% to 2% level in the measurements of $\mathcal{R}(D^{(*)})$.

Especially for semitauonic analyses using the electronic or muonic $\tau$ decay channels, a reliable description of $B \to D^{(*)}\ell\nu$ semileptonic decays is a critical input for controlling lepton cross-feed backgrounds. The hadronic $\tau$ decay analyses also rely on these light semileptonic inputs, but to a lesser extent. Finally, there is some degree of additional uncertainty in the modeling of the detector resolution for the kinematic variables that these analyses depend upon that can be shared across results from the same experiment.

### C. $B \to D^{**}\tau\nu$ and other $B \to D^{**}$ backgrounds

#### 1. Evaluation and control of systematic uncertainties

Excited $D^{**}$ states decay to $D^*$, $D^0$, or $D^\pm$ mesons plus additional photons or pions, which can escape detection. As a result, both $B \to D^{**}\ell\nu$ and $B \to D^{**}\tau\nu$ decays can easily lead to extraneous candidates in $\mathcal{R}(D^{(*)})$ analyses, although the former contributes only to measurements that employ the leptonic decays of the $\tau$ lepton. In hadronic-$\tau$ analyses, another background source associated with $D^{**}$ production is formed by $B \to D^{**}D_s^{(*,**)}$ decays with $D_s^+ \to \pi^+\pi^-\pi^+X$. While all analyses exploit dedicated $D^{**}$ control samples where some of the parameters describing these contributions are measured, a number of assumptions are shared among the various measurements, namely, the form factor parametrization of the $B \to D^{**}l\nu$ decays (Sec. II.E) and the $D^{**}$ decay branching fractions.

The first data-driven fits of the $B \to D^{**}$ form factors have been performed (Bernlochner and Ligeti, 2017; Bernlochner, Ligeti, and Robinson, 2018), but the resulting parameters, especially for the broad states, are not yet well constrained. The chosen approach is, however, improvable with future data. Just as for the $B \to D^{(*)}$ modes, data-driven predictions for $B \to D^{**}$ [Eq. (29)] are thus likely to improve in precision until they reach the naive order of the $1/m_c^2$ contributions (i.e., a few percent), beyond which the number of parameters required to describe higher-order effects becomes too large to be effectively constrained. Combination with future LQCD results [see, for example, Bailas *et al.* (2020)], however, may permit even more precise predictions. Additionally, the $\mathcal{R}(D^{**})$ ratios have not yet been measured, so the various experiments have relied on theoretical predictions, assigning a relatively large uncertainty. The size of this uncertainty is, however, arbitrary and could lead to a common underestimate of the systematic uncertainty from the $D^{**}$ feed-down; see Sec. V.C.2. With the latest theoretical predictions [Eq. (29)], this uncertainty should be reduced in the future.

Dedicated experimental efforts are also presently ongoing to further address these issues. In particular, they are as follows:

(i) Improved measurements are anticipated for the $B \to D^{**}\ell\nu$ relative branching fractions and kinematic distributions such as the four-momentum transfer squared or further angular relations. This is especially important for the broad $D_1'$ and $D_0^*$ states, which are still poorly known compared to the narrow $D_1$ and $D_2^*$ states. Such measurements can in principle already be carried out with currently available datasets.

(ii) Measurements involving a hadronized $W \to D_s^+$, i.e., $B \to (D^{**} \to D^{(*)}\pi)D_s^+$ (Aaij *et al.*, 2020a;

LHCb Collaboration, 2020). This approach offers much better sensitivity to decays involving the wide $D^{**}$ states because the $D^{(*)}\pi$ spectrum can be cleanly measured via the sideband subtraction on the narrow $B$ mass peak. Additionally, the presence of a $D_s^+$ meson in the final state offers two unique features: (a) in contrast to decays where the virtual $W$ produces a single pion, the $q^2$ range for production of a $D_s^+$ meson is in the range of interest for semitauonic decays, and (b) the relative rates of the various $D^{**}$ states can be measured when associated with both spin-0 ($D_s$) and spin-1 ($D_s^*$) states.

(iii) The direct measurement of $B \to D^{**}\tau\nu$ decays for the narrow states $D^{**} = D_1$ or $D_2^*$. When combined with the estimated branching fractions for the narrow $D^{**}$ versus the total $D^{**}$ rate and expectations from isospin symmetry (the feed-down is dominated by $D^{**\pm}$ states, while much better experimental precision will be achieved for $D^{**0}$), these $B \to D^{**}\tau\nu$ results might be used to control the $D^{**}$ feed-down rate in the $\mathcal{R}(D^{(*)})$ signal regions.

Significant progress can therefore be expected in the control of this important common systematic uncertainty in the near term, such that the systematic uncertainty due to $B \to D^{**}l\nu$ decays is likely to be reduced to the percent level or less.

#### 2. $D^{**}$ branching fraction assumptions in $\mathcal{R}(D^{(*)})$ analyses

While the estimation of the normalization of the contributions from background $B \to D^{**}l\nu$ decays is largely data driven, a number of assumptions in the various branching fractions involved can have a significant impact in the measurement of $\mathcal{R}(D^{(*)})$. These are as follows:

(i) $\mathcal{B}(D^{**} \to D^{(*)}\pi(\pi))$: These branching fractions are primary inputs to all the $B \to D^{**}l\nu$ templates employed in the signal extraction fits. Using the approach of Bernlochner and Ligeti (2017), $\mathcal{B}(D^{**} \to D^{(*)}\pi)$ can be estimated by combining data for the ratios $\mathcal{B}(D^{**} \to D^*\pi)/\mathcal{B}(D^{**} \to D\pi)$ (Zyla *et al.*, 2020), isospin relations, and measurements of ratios of non-$D^*$-resonant three-body $D_1^0$ and $D_2^{*0}$ decays to $D^0\pi^+\pi^-$ versus two-body decays to $D^{*+}\pi^-$ (Aaij *et al.*, 2011). The latter are used to estimate the total non-$D^*$-resonant branching fractions to all possible $D\pi\pi$ final states with an isospin correction factor $\simeq 2$. The resulting estimates for exclusive two-body decays and the sum of non-$D^*$-resonant three-body decays are shown in Table XVI. The experimental analyses, however, have used various other sets of different numbers, which is worth revisiting.

(ii) $\mathcal{B}(B \to D^{**}\ell\nu)$.—As previously mentioned, the hadronic-$\tau$ measurements are not sensitive to this contribution. The leptonic-$\tau$ analyses have some sensitivity to these branching fractions, but it is small because the total contribution from $B \to D^{**}\ell\nu$ decays for the four $D^{**}$ states is floated in the various fits. Since the four contributions are combined together in the same fit template, the relative $B \to D^{**}\ell\nu$ branching fractions, which are typically taken from Zyla *et al.* (2020), impact the measured $\mathcal{R}(D^{(*)})$ values at the 0.3%–0.8% level (Lees *et al.*, 2013).

TABLE XVI. Estimates for $D^{**}$ strong decay branching fractions to exclusive two-body decays, and the sum of non-$D^*$-resonant three body decays ($\sum D\pi\pi$) based on the approach of Bernlochner and Ligeti (2017) and measurements from Aaij *et al.* (2011) and Zyla *et al.* (2020).

| Parent | Final state | | | | |
|---|---|---|---|---|---|
| | $D^*\pi^+$ | $D^*\pi^0$ | $D\pi^+$ | $D\pi^0$ | $\sum D\pi\pi$ |
| $D_2^*$ | 0.26 | 0.13 | 0.40 | 0.20 | ⋯ |
| $D_1$ | 0.42 | 0.21 | ⋯ | ⋯ | 0.36 |
| $D_1'$ | 0.67 | 0.33 | ⋯ | ⋯ | ⋯ |
| $D_0$ | ⋯ | ⋯ | 0.67 | 0.33 | ⋯ |

(iii) $\mathcal{B}(B \to D^{**}\tau\nu)$.—All $\mathcal{R}(D^{(*)})$ measurements are sensitive to this contribution because the kinematics of the final state particles in these decays are similar to those in signal decays. Some leptonic-$\tau$ measurements tie this contribution to the fitted $B \to D^{**}\ell\nu$ yields via $\mathcal{R}(D^{**})$ or merge it with other background contributions. The *BABAR* analysis (Lees *et al.*, 2013) assumes that $\mathcal{R}(D^{**}) = 0.18$ for all $D^{**}$ states. Investigation of the numerical simulation inputs used by Belle analyses (Huschle *et al.*, 2015; Caria *et al.*, 2020) suggests that they assumed an average of $\mathcal{R}(D^{**}) = 0.15$, while the LHCb result (Aaij *et al.*, 2015c) uses $\mathcal{R}(D^{**}) = 0.12$. The hadronic-$\tau$ $\mathcal{R}(D^*)$ measurement from LHCb (Aaij *et al.*, 2018b) ties the $B \to D^{**}\tau\nu$ yield to be 11% of the fitted $B \to D^*\tau\nu$ yield and further decreases the value of $\mathcal{R}(D^*)$ by 3% to take into account an additional contribution from $B_s \to D_{s1}'\tau\nu$ decays. Notably, all these assumed values for $R(D^{**})$ are significantly above the predicted central values [Eq. (29)], by about 50%. The impact on the measured values can be estimated from the $\mathcal{R}(D^{**})$ systematic uncertainty estimated by Lees *et al.* (2013). A 50% downward variation of the assumed $\mathcal{R}(D^{**}) = 0.18$ value results in $\mathcal{R}(D^{(*)})$ increasing by 1.7%–1.8%. A shift of this magnitude would result in an increase of the tension of the $\mathcal{R}(D^{(*)})$ world average with the SM predictions by more than $0.5\sigma$. For future measurements, we therefore advocate that researchers revisit their assumptions regarding the $D^{**}$ feed-down in light of available data-driven predictions.

(iv) $\mathcal{B}(B_s \to D_s^{**}X)$.—Additional feed-down contributions to the LHCb measurements of $\mathcal{R}(D^{(*)})$ come from decays involving partially reconstructed heavy $D_s^{**}$ mesons, namely, $B_s \to D_{s1}^*$ and $B_s \to D_{s2}^*$. The $D_{s1}^*$ and $D_{s2}^*$ mesons are heavy enough that they decay primarily as $D_s^{**} \to D^{(*)}K$. Given that the $B_s \to D_s^{**}l\nu$ branching fractions have not yet been

measured and the considerable $B_s$ meson production at the LHC (see Table III), these decays can lead to sizable uncertainties on $\mathcal{R}(D^{(*)})$. In a fashion similar to the $B \to D^{**} l\nu$ decays, $B_s \to D_s^{**}\ell\nu$ decays contribute only to measurements that employ the leptonic decays of the $\tau$ lepton, while $B_s \to D_s^{**}\tau\nu$ decays contribute to both leptonic- and hadronic-$\tau$ measurements, and $B_s \to D_s^{**}D_s^{+}X$ decays with $D_s^{+} \to \pi^{+}\pi^{-}\pi^{+}X$ contribute to hadronic-$\tau$ results. As an example of the potential size of these contributions, the present correction due to the $B_s \to D_s^{**}\tau\nu$ feed-down in the hadronic-$\tau$ measurement of $\mathcal{R}(D^{*})$ by LHCb is 3%, with a relative uncertainty of 50%. Future measurements of the $B_s \to D_s^{**}$ branching fractions will thus be important in enabling one to reach percent-level uncertainties in the LHCb measurements of $\mathcal{R}(D^{(*)})$, as well as in $\mathcal{R}(D_s^{(*)})$.

### D. Modeling other signal modes

Some insight into the precision of future form factor predictions, and their role in LFUV analyses, can be obtained from considering the case of $B_c \to J/\psi\tau\nu$. As can be seen in Table XIII, a dominant systematic uncertainty (17%) in the 2018 LHCb analysis (Aaij *et al.*, 2018a) arose from the poorly known description of the $B_c \to J/\psi$ form factors. At the time, the prediction for $\mathcal{R}(J/\psi)$ was known only at the 10% level or worse. However, recent LQCD results for the $B_c \to J/\psi$ form factors [Eq. (34)] now permit percent-level predictions such that one might expect the corresponding systematic uncertainty to similarly drop by an order of magnitude in a future analysis.

With regard to $\Lambda_b \to \Lambda_c^{(*)}$ decays, while the ground-state form factors are already known to high precision, a combination of anticipated LQCD results and future data may similarly permit the excited state form factors to be constrained at or beyond the $1/m_c^2$ level. Finally, future LQCD studies may be expected to improve predictions for $B_s \to D_s^{(*,**)}$ form factors to a level comparable to that for $B \to D^{(*,**)}$, which is well beyond the ∼20% uncertainties from flavor symmetry arguments.

### E. Other background contributions

Double-charm decays of the forms $B \to D^{(*,**)}D_s^{(*,**)}$ and $B \to D^{(*,**)}D^{(*,**)}K^{(*)}$ can lead to final state topologies that are similar to those of semitauonic processes whenever the decay of one of the charm mesons mimics that of a $\tau$ lepton. Examples are $D_s^{(*,**)} \to X\tau\nu, X\pi^{+}\pi^{-}\pi^{+}$ or $D^{(*,**)} \to X\ell\nu$, with $X$ referring to unreconstructed particles. Such processes are significant background modes for $\mathcal{R}(D^{(*)})$ measurements at LHCb and, to a somewhat lesser extent, for $B$-factory measurements. While several of these analyses estimate the overall double-charm contribution using data control samples, all measurements rely on averages of previously measured branching fractions of $B$ and $D$ decays from the Particle Data Group compilation (Zyla *et al.*, 2020). These averages are used as an input to produce the right mixture of decay modes for background templates. Additionally, the extrapolations into the signal regions often rely on simulations whose models for the decay dynamics might not reflect the full resonance structure of such transitions. This set of assumptions can be common to several experiments.

Although a wealth of branching fraction determinations regarding these and other relevant decays have been accumulated by BESIII (Ablikim *et al.*, 2010), *BABAR*, Belle, and LHCb, there are significant areas where measurements that are in principle feasible have not been carried out or are not precise enough to provide useful constraints. Instances of these are double-charm decays with excited kaons in the final state or hadronic and double-charm processes involving $D^{**}$ states. These are especially important because they cover the high $q^2$ range that has the highest signal purity in $\mathcal{R}(D^{(*)})$ results. In the near future, Belle II and LHCb will provide new measurements of branching fractions for such decays that will alleviate the reliance on common assumptions for the various double-charm decay modes. Additionally, more precise information about the semileptonic and $\pi^{+}\pi^{-}\pi^{+}$ decays of charm mesons, which can be provided by BESIII in the near future, will be needed.

### F. Other systematic uncertainties

The remaining uncertainties in Table XV are dominated by particle identification and external branching fraction uncertainties. The latter are especially relevant for measurements that utilize the hadronic decays of the $\tau$ lepton. The final state for the signal decays in these measurements does not correspond to that of the $B \to D^{(*)}\ell\nu$ decays needed for the $\mathcal{R}(D^{(*)})$ denominator and, as a result, intermediate normalization modes are employed. For instance, the current precision on the normalization decays for the $\tau \to \pi^{-}\pi^{+}\pi^{-}\nu$ analysis from LHCb (Aaij *et al.*, 2018b), $B \to D^{*}\pi^{+}\pi^{-}\pi^{+}$ and $B \to D^{*}\mu\nu$, as shown in Eq. (53), is limited to 3% to 4%, so new measurements of these branching fractions are necessary to reduce the overall uncertainty beyond that level. In fact, what is required is the ratio of these two quantities. This can be measured more precisely than each branching ratio separately: a measurement that Belle II may be able to perform relatively easily.

Radiative contributions from $B \to D^{(*)}l\gamma\nu$ decays reconstructed as $B \to D^{(*)}l\nu$ are further sources of common systematic uncertainties. These may arise at approximately the few percent level, and are thought to be well approximated in experimental simulations by PHOTOS (Barberio and Was, 1994), although Coulomb-term corrections may eventually also become important (de Boer, Kitahara, and Nisandzic, 2018; Calí *et al.*, 2019; Klaver, 2019).

## VI. COMBINATION AND INTERPRETATION OF THE RESULTS

The semitauonic measurements described in Sec. IV exhibit various levels of disagreement with the SM predictions. In this section, we further examine these results and explore these tensions. To resummarize, the following recent measurements

TABLE XVII. Summary of $\mathcal{R}(D^{(*)})$ measurements and world averages. The hadronic-$\tau$ LHCb result (Aaij *et al.*, 2018b) has been updated by taking into account the latest HFLAV average of $\mathcal{B}(B^0 \to D^{*+}\ell\nu) = (5.08 \pm 0.02 \pm 0.12)\%$. The values for "Average ($\hat{\rho}_{D^{**}}$)" are calculated by profiling the unknown $B \to D^{**}l\nu$ correlation and obtaining $\hat{\rho}_{D^{**}} = -0.88$ as described in Sec. VI.B.

| Experiment | $\tau$ decay | Tag | $\mathcal{R}(D)$ | $\mathcal{R}(D^*)$ | $\rho_{\text{tot}}$ |
|---|---|---|---|---|---|
| *BABAR*[a] | $\mu\nu\nu$ | Hadronic | 0.440(58)(42) | 0.332(24)(18) | −0.31 |
| Belle[b] | $\mu\nu\nu$ | Semileptonic | 0.307(37)(16) | 0.283(18)(14) | −0.52 |
| Belle[c] | $\mu\nu\nu$ | Hadronic | 0.375(64)(26) | 0.293(38)(15) | −0.50 |
| Belle[d] | $\pi\nu$, $\rho\nu$ | Hadronic | | $0.270(35)^{(+28)}_{(-25)}$ | ⋯ |
| LHCb[e] | $\pi\pi\pi(\pi^0)\nu$ | ⋯ | ⋯ | 0.280(18)(25)(13) | ⋯ |
| LHCb[f] | $\mu\nu\nu$ | ⋯ | ⋯ | 0.336(27)(30) | ⋯ |
| Average ($\hat{\rho}_{D^{**}}$) | | | 0.337(30) | 0.298(14) | −0.42 |
| HFLAV Avg.[g] | | | 0.340(30) | 0.295(14) | −0.38 |

[a]See Lees *et al.* (2012, 2013).
[b]See Caria *et al.* (2020).
[c]See Huschle *et al.* (2015).
[d]See Hirose *et al.* (2018).
[e]See Aaij *et al.* (2018b).
[f]See Aaij *et al.* (2015c).
[g]See Amhis *et al.* (2019).

are currently available (see also Table V and references therein):

(1) $B \to D^{(*)}\tau\nu$ decays
   (a) Six measurements of $\mathcal{R}(D^*)$ and three measurements of $\mathcal{R}(D)$. For convenience we resummarize these results in Table XVII.
   (b) One measurement of the $\tau$ polarization fraction, $P_\tau(D^*) = -0.38 \pm 0.51^{+0.21}_{-0.16}$.
   (c) One measurement of the $D^*$ longitudinal polarization fraction, $F_{L,\tau}(D^*) = 0.60 \pm 0.08 \pm 0.04$.
   (d) Two measurements of the efficiency-corrected $q^2$ distributions shown in Fig. 11.
(2) One measurement of a $b \to c\tau\nu$ transition using $B_c$ decays, $\mathcal{R}(J/\psi) = 0.71 \pm 0.17 \pm 0.18$.
(3) One measurement of a $b \to u\tau\nu$ transition, $\mathcal{R}(\pi) = 1.05 \pm 0.51$.

In Sec. VI.A, we inspect the measurements of $\mathcal{R}(D^{(*)})$ in terms of the light-lepton normalization modes, the isospin-conjugated modes, and their measured values as a function of time. Thereafter we revisit in Sec. VI.B the combination of the measured $\mathcal{R}(D^{(*)})$ values. In particular, we discuss the role of nontrivial correlation effects on such averages and point out that, with more precise measurements on the horizon, these effects will need to be revisited. In Sec. VI.C we discuss the saturation of the measured inclusive rate by exclusive contributions implied by the current world averages of $\mathcal{R}(D^*)$ and $\mathcal{R}(D)$ together with the expected $B \to D^{**}\tau\nu$ rates. Finally, Secs. VI.D and VI.E discuss the challenges in developing self-consistent new physics interpretations of the observed tensions with the SM and possible connections to the present-day flavor-changing neutral-current (FCNC) anomalies, respectively.

### A. Dissection of $\mathcal{R}(D^{(*)})$ results and SM tensions

The current status of LFUV measurements versus SM predictions, and the significance of their respective tensions or agreements, is summarized in Table XVIII and includes the current HFLAV combination of the $\mathcal{R}(D^{(*)})$ data. For the SM predictions the arithmetic averages discussed in Sec. II are quoted. The individual tensions of all LFUV measurements with the SM expectations range from $0.2\sigma$ to $2.5\sigma$. The combined value of $\mathcal{R}(D)$ and $\mathcal{R}(D^*)$ is in tension with the SM expectation by $3.1\sigma$ because of their anticorrelation. Note also that the value of $P_\tau(D^*)$ is slightly correlated with both averages.

TABLE XVIII. Current status of LFUV measurements (see Sec. IV) versus SM predictions in Sec. II and their respective agreements or tensions. For $P_\tau(D^*)$ and $F_{L,\tau}(D^*)$ we show a naive arithmetic average of the SM predictions (Table II), as was done for $\mathcal{R}(D^{(*)})$. For $\mathcal{R}(D^{(*)})$ we show the world average from the HFLAV combination (Amhis *et al.*, 2019). In the last two rows we show for comparison the results of the $\mathcal{R}(D^{(*)})$ world average obtained in this review; see Sec. VI.B.

| Observable | Current world-average data | Current SM prediction | Significance | |
|---|---|---|---|---|
| $\mathcal{R}(D)$ (HFLAV) | $0.340 \pm 0.030$ | $0.299 \pm 0.003$ | $1.2\sigma$ | $3.1\sigma$ |
| $\mathcal{R}(D^*)$ (HFLAV) | $0.295 \pm 0.014$ | $0.258 \pm 0.005$ | $2.5\sigma$ | |
| $P_\tau(D^*)$ | $-0.38 \pm 0.51^{+0.21}_{-0.16}$ | $-0.501 \pm 0.011$ | $0.2\sigma$ | |
| $F_{L,\tau}(D^*)$ | $0.60 \pm 0.08 \pm 0.04$ | $0.455 \pm 0.006$ | $1.6\sigma$ | |
| $\mathcal{R}(J/\psi)$ | $0.71 \pm 0.17 \pm 0.18$ | $0.2582 \pm 0.0038$ | $1.8\sigma$ | |
| $\mathcal{R}(\pi)$ | $1.05 \pm 0.51$ | $0.641 \pm 0.016$ | $0.8\sigma$ | |
| $\mathcal{R}(D)$ (this review) | 0.337±0.030 | $0.299 \pm 0.003$ | $1.3\sigma$ | $3.6\sigma$ |
| $\mathcal{R}(D^*)$ (this review) | 0.298±0.014 | $0.258 \pm 0.005$ | $2.5\sigma$ | |

A subset of the existing measurements provide values of $\mathcal{R}(D^{(*)})$ normalized to either electron or muon final states. These results present an important check because the values reported for the semitauonic ratios are typically an average for the electron and muon normalizations assuming that

$$\mathcal{R}(D^{(*)}) = \mathcal{R}(D^{(*)})_e = \mathcal{R}(D^{(*)})_\mu, \tag{67}$$

with

$$\mathcal{R}(D^{(*)})_e \equiv \frac{\mathcal{B}(\bar{B} \to D^{(*)}\tau^-\bar{\nu}_\tau)}{\mathcal{B}(\bar{B} \to D^{(*)}e^-\bar{\nu}_e)}, \tag{68}$$

$$\mathcal{R}(D^{(*)})_\mu \equiv \frac{\mathcal{B}(\bar{B} \to D^{(*)}\tau^-\bar{\nu}_\tau)}{\mathcal{B}(\bar{B} \to D^{(*)}\mu^-\bar{\nu}_\mu)}. \tag{69}$$

LHCb measures only $\mathcal{R}(D^{(*)})_\mu$, but the $B$ factories have access to the electron normalization as well. Figure 24 compares $\mathcal{R}(D^{(*)})_e$ and $\mathcal{R}(D^{(*)})_\mu$, and no systematic deviation between the two ratios is observed. Note that these results were released as stability checks that compare the compatibility of the electron and muon channels, not as optimized measurements of $\mathcal{R}(D^{(*)})_{e/\mu}$. For instance, Franco Sevilla (2012) did not include the full systematic uncertainties and correlation for the electron and muon $\mathcal{R}(D^{(*)})$, so the values from the full $\mathcal{R}(D^{(*)})$ results are used in Fig. 24, increasing the correlation to account for the larger statistical uncertainty of the $\mathcal{R}(D^{(*)})_e$ and $\mathcal{R}(D^{(*)})_\mu$ results. Additionally, the double ratio

$$\mathcal{R}(D^{(*)})_{\text{light}} = \frac{\mathcal{R}(D^{(*)})_\mu}{\mathcal{R}(D^{(*)})_e} = \frac{\mathcal{B}(\bar{B} \to D^*e^-\bar{\nu}_e)}{\mathcal{B}(\bar{B} \to D^*\mu^-\bar{\nu}_\mu)} \tag{70}$$

that would be obtained from dividing these results would have unnecessarily large uncertainties because the common $\mathcal{B}(B \to D^{(*)}\tau\nu)$ factor is obtained with $\tau \to e\nu\bar{\nu}$ decays in the case of $\mathcal{R}(D^{(*)})_e$, and $\tau \to \mu\nu\bar{\nu}$ decays for $\mathcal{R}(D^{(*)})_\mu$. A high-precision measurement of $\mathcal{R}(D^{(*)})_{\text{light}}$ was recently released by the Belle Collaboration (Waheed *et al.*, 2019)

$$\mathcal{R}(D^{(*)})_{\text{light}} = 1.01 \pm 0.01 \pm 0.03 \tag{71}$$

and is compatible with unity.

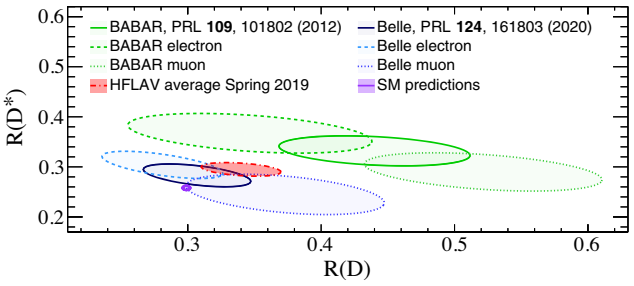


FIG. 24. Measurements of $\mathcal{R}(D^{(*)})$, $\mathcal{R}(D^{(*)})_e$, and $\mathcal{R}(D^{(*)})_\mu$ from *BABAR* (Franco Sevilla, 2012) and Belle (Caria, 2019).

TABLE XIX. Results of the isospin-unconstrained fits for the *BABAR* analysis (Lees *et al.*, 2012, 2013). The first uncertainty is statistical and the second systematic.

| Result | *BABAR* |
|---|---|
| $\mathcal{R}(D^0)$ | $0.429 \pm 0.082 \pm 0.052$ |
| $\mathcal{R}(D^+)$ | $0.469 \pm 0.084 \pm 0.053$ |
| $\mathcal{R}(D^{*0})$ | $0.322 \pm 0.032 \pm 0.022$ |
| $\mathcal{R}(D^{*+})$ | $0.355 \pm 0.039 \pm 0.021$ |

Table XIX shows the results of the isospin-unconstrained fits of the *BABAR* $\mathcal{R}(D^{(*)})$ analysis, which exhibit good compatibility between charged and neutral $D$ and $D^*$ modes. Such measurements might be particularly interesting in the context of obtaining data-driven insight into the size of semiclassical radiative corrections, which are expected to enter at the subpercent level.

Another interesting comparison is to examine the measurements of $\mathcal{R}(D^{(*)})$ as a function of time: more precise knowledge of normalization and background processes can lead to shifts in the central values. Figure 25 displays the measured value as a function of paper submission time and illustrates the improving precision with time. The most recent measurements tend to display better agreement with the SM expectations. It is not clear, however, whether this is a systematic shift or a statistical fluctuation, as there have not been meaningful changes in the procedures that determine the background, normalization, and signal components. Note also that all measurements are compatible among themselves, with a $\chi^2$ probability of 27%.

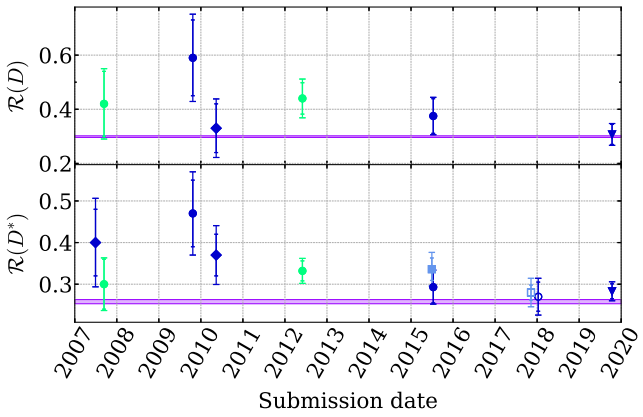


FIG. 25. Measurements of $\mathcal{R}(D^{(*)})$ as a function of paper submission time. Green (light gray) refers to *BABAR*, dark blue (dark gray) refers to Belle, light blue (medium gray) refers to LHCb, and violet refers to the SM predictions. Circular markers refer to hadronic tagging, triangles refer to semileptonic tagging, diamonds refer to inclusive tagging, and squares refer to untagged measurements. Filled markers refer to measurements using muonic decays of the $\tau$ lepton, while hollow markers refer to hadronic decays. Some of the earlier results measured $\mathcal{B}(B \to D^{(*)}\tau\nu)$ instead of $\mathcal{R}(D^{(*)})$. In those cases, the values for $\mathcal{R}(D^{(*)})$ were obtained by normalizing the $\tau$ branching fraction with the latest world averages for $\mathcal{B}(B \to D^{(*)}\ell\nu)$ (Zyla *et al.*, 2020).

### B. Revisiting of $\mathcal{R}(D^{(*)})$ world averages via $D^{**}$ correlations

To further investigate the tension of the measured values of $\mathcal{R}(D^{(*)})$ with the SM, we examine and update their averages. We note that the systematic uncertainties of all measurements have significant correlations (see Sec. V) that need to be properly taken into account. The most important ones stem from the modeling of the $B \to D^{**} l\nu$ processes, which have constituted a significant background source in all measurements to date. The manner in which the uncertainties of these background contributions are estimated varies considerably. As discussed in Sec. V.C.1, the normalization or shape uncertainties from the hadronic form factors are, in some measurements, validated or constrained by control regions. Thus, a simple correlation model will not be able to properly quantify such correlations.

One particularly important point here is the treatment of the correlations of these systematics between $\mathcal{R}(D^*)$ and $\mathcal{R}(D)$ measurements. In individual measurements that measure both quantities simultaneously, this treatment is straightforward. However, it becomes unclear how to relate systematic uncertainties between $\mathcal{R}(D)$ and $\mathcal{R}(D^*)$ in two separate measurements. To provide a concrete example, consider the *BABAR* measurement of $\mathcal{R}(D)$ [in the context of the combined $\mathcal{R}(D^{(*)})$ determination made by Lees *et al.* (2012, 2013)] and the Belle measurement of $\mathcal{R}(D^*)$ [in the combined $\mathcal{R}(D^{(*)})$ analysis of Huschle *et al.* (2015)]. In the individual measurements, the systematic uncertainty associated with $B \to D^{**}\ell\bar{\nu}_\ell$ is 45% and −15% correlated between $\mathcal{R}(D)$ and $\mathcal{R}(D^*)$, respectively.[10] From this information alone it is impossible to derive the correct correlation structure between $\mathcal{R}(D)$ and $\mathcal{R}(D^*)$ across the measurements.

We further investigate the dependence of the world average on the $B \to D^{**}\ell\bar{\nu}_\ell$ correlation structure across the $\mathcal{R}(D)$ and $\mathcal{R}(D^*)$ measurements by parametrizing them with a single factor $\rho_{D^{**}}$. In Fig. 26 (left panel) we show the world average assuming such correlation effects are negligible (labeled as $\rho_{D^{**}} = 0$) and we reproduce a world average very similar to HFLAV (Amhis *et al.*, 2019). The numerical values, normalized to the arithmetic average of the SM predictions (cf. Table I in Sec. II.D.1), are

$$\mathcal{R}(D)/\mathcal{R}(D)_{\mathrm{SM}} = 1.12 \pm 0.10, \tag{72}$$

$$\mathcal{R}(D^*)/\mathcal{R}(D^*)_{\mathrm{SM}} = 1.15 \pm 0.06, \tag{73}$$

with an overall correlation of $\rho = -0.33$. In addition to the $B \to D^{**}\ell\bar{\nu}_\ell$ uncertainties, the uncertainties in the leptonic $\tau$ branching fractions and the $B \to D^{(*)} l\nu$ FFs are fully correlated across measurements. The compatibility with the SM expectation is within 3.2 standard deviations [close to the value quoted by Amhis *et al.* (2019)] of $3.1\sigma$). Figure 26 (left panel) also shows the impact of setting this unknown correlation to either $\rho_{D^{**}} = 1$ or $-1$, resulting in compatibilities with the SM predictions of 2.9 and 3.7 standard deviations, respectively.

A possible way to deal with an unknown parameter such as $\rho_{D^{**}}$ in this type of problem was outlined by Cowan (2019). Instead of neglecting the value, we can incorporate it as a free parameter of the problem and constrain it within its probable range. A possible choice that limits this missing correlation to fall between $[-1, 1]$ is to assign it a double Fermi-Dirac distribution[11] with a large shape parameter such as $w = 50$. Carrying out our average with such a set up results in

$$\mathcal{R}(D)/\mathcal{R}(D)_{\mathrm{SM}} = 1.13 \pm 0.10, \tag{74}$$

$$\mathcal{R}(D^*)/\mathcal{R}(D^*)_{\mathrm{SM}} = 1.15 \pm 0.06, \tag{75}$$

with $\hat{\rho}_{D^{**}} = -0.88$ and an overall correlation of $\rho = -0.40$. This results in an increased tension of about $3.6\sigma$ with respect to the SM.

Although neither of these world averages are based on completely correct assumptions, they illustrate the need for future $\mathcal{R}(D^{(*)})$ measurements to provide more detailed breakdowns of their uncertainties. It is intriguing that introducing an additional correlation structure of a systematic uncertainty can shift the agreement with the SM expectation over a range of 0.8 standard deviations. Table XVII lists the numerical values of this average [denoted as "average ($\hat{\rho}_{D^{**}}$)"] and the HFLAV average (Amhis *et al.*, 2019); see also Table XVIII. We show this world average for $\mathcal{R}(D^{(*)})$ compared to the various measurements in Fig. 26 (right panel).

### C. Exclusive saturation of the inclusive rate

The SM prediction for the semitauonic inclusive branching ratio is

$$\mathcal{B}(B \to X_c \tau\nu) = 2.37(6) \times 10^{-2}, \tag{76}$$

which is obtained by combining the SM prediction in Eq. (38) with the data for the flavor-averaged light-lepton branching ratio $\mathcal{B}(B \to X_c \ell\nu)$ (Zyla *et al.*, 2020). This value of the inclusive branching fraction should correspond to the sum of branching fractions of all possible exclusive final states; i.e., the sum of decay rates of exclusive states should saturate the inclusive rate. The degree of this saturation can be explored by comparing the inclusive branching ratio to that for the sum of $D^{(*)}$ and $D^{**}$. For simplicity, in the following we treat the uncertainties for each mode as independent. Using the HFLAV-averaged SM prediction for $\mathcal{R}(D^{(*)})$ (Table I) together with the average branching ratio for $\mathcal{B}(B^0 \to D^{(*)}\ell\nu)$ and $\mathcal{B}(B^- \to D^{(*)}\ell\nu)$, one finds that

$$\mathcal{B}(B \to D\tau\nu) = 0.72(4) \times 10^{-2}, \tag{77a}$$

$$\mathcal{B}(B \to D^*\tau\nu) = 1.28(4) \times 10^{-2}, \tag{77b}$$

[10] Both measurements provide the systematic uncertainties associated with $D^{**}$ in a different granularity. The quoted correlations are obtained by summing for (Lees *et al.*, 2012, 2013) the resulting covariance matrices for the $D^{**}$ form factor and the various branching fraction uncertainties. For Huschle *et al.* (2015), the covariance matrices for the $B \to D^{**}\ell\bar{\nu}_\ell$ shape and the $D^{**}$ are summed.

[11] $f(x, w) = 1/(2\{1 + \exp[w(x-1)]\}\{1 + \exp[-w(x-1)]\})$.

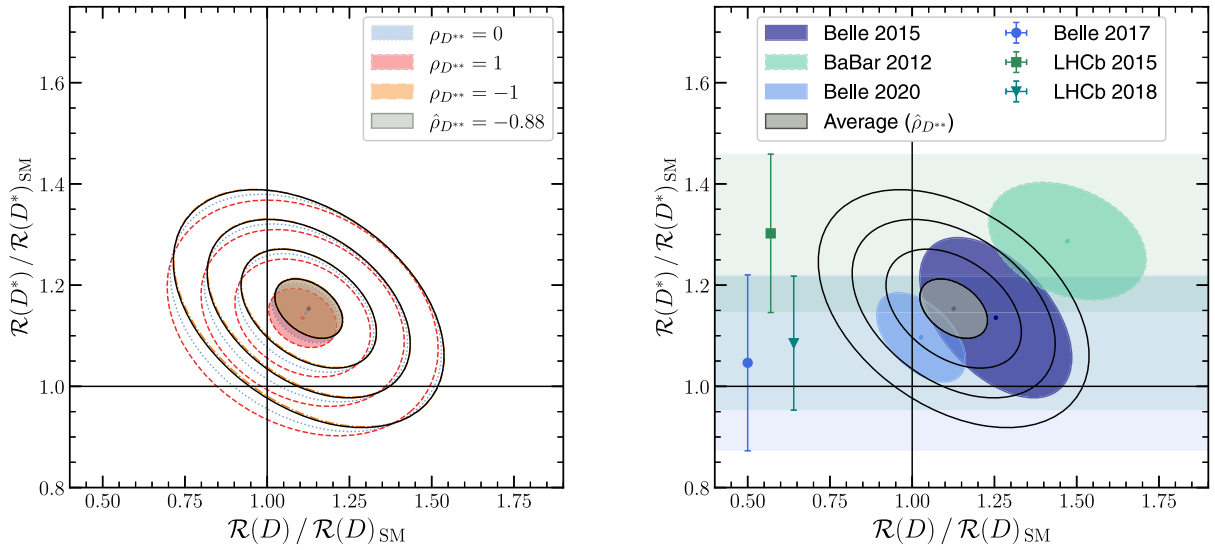


FIG. 26. Left panel: $\mathcal{R}(D^{(*)})$ world averages with different assumptions for the unknown correlation $\rho_{D^{**}}$. The average with $\rho_{D^{**}} = 0$ (light blue or light gray dotted curves) is based on assumptions similar to those made by Amhis *et al.* (2019) and shows a compatibility with the SM expectation of 3.2 standard deviations while taking into account the small uncertainties of the theoretical predictions; the scenarios $\rho_{D^{**}} = 1$ (red or medium gray dashed curves) and $\rho_{D^{**}} = -1$ (orange or light gray dash-dotted curves) agree with the SM expectation within 2.9 and 3.7 standard deviations, respectively. In our quoted average we profile the unknown correlation and obtain $\hat{\rho}_{D^{**}} = -0.88$ (heather gray solid curves) with a compatibility with the SM of 3.6 standard deviations. Right panel: our world average of $\mathcal{R}(D)$ and $\mathcal{R}(D^*)$ (black solid curves) compared to the various measurements of $\mathcal{R}(D^{(*)})$. The unknown correlation $\rho_{D^{**}}$ is treated as a free but constrained parameter of the average (see the main text for more details).

and similarly one may use the combined $D^{**}$ SM prediction in Eq. (30) with world averages for $\mathcal{B}(B^- \to D^{**}\ell\nu)$ (Bernlochner and Ligeti, 2017), which yields

$$\sum_{X_c \in D^{**}} \mathcal{B}(B \to X_c \tau\nu) = 0.14(2) \times 10^{-2}. \tag{78}$$

Adding these contributions, one obtains the SM prediction $\sum_{X_c \in D^{(*,**)}} \mathcal{B}(B \to X_c \tau\nu) = 2.14(6) \times 10^{-2}$, which is compatible with, and does not saturate, the inclusive SM prediction in Eq. (76), as shown in Fig. 27.

One can characterize the degree of LFUV in the semitauonic system by comparing the inclusive SM prediction with the sum of measured branching ratios for $\mathcal{B}(B \to D^{(*)}\tau\nu)$. In this case the SM prediction in Eq. (76) arises from theoretical inputs, and features theoretical uncertainties, that are independent of the inputs used for predictions of $\mathcal{R}(D^{(*)})$; see Sec. II.G. Figure 27 compares the inclusive SM prediction to the sum of the $B \to D^{(*)}\tau\nu$ branching fractions arising from the $\mathcal{R}(D^{(*)})$ world averages, as well as to the measured inclusive $b \to X\tau\nu$ branching fraction from LEP (Zyla *et al.*, 2020) and the result for $B \to X\tau\nu$ from the Ph.D. thesis of Hasenbusch (2018) using Belle data. One sees that the $\mathcal{R}(D^{(*)})$ world averages already imply near saturation of the inclusive SM prediction, while the unpublished result from the Belle data is more than $3\sigma$ in tension with it.

### D. New physics interpretations

#### 1. Parametrization of SM tensions

The measured lepton universality ratios $\mathcal{R}(D^{(*)})$ naively express tensions with respect to SM predictions in terms of the overall decay rates or branching ratios. As such, typically many phenomenological interpretations of these results simply require that any NP accounts for the measured ratios (or other observables such as polarization fractions) within quoted

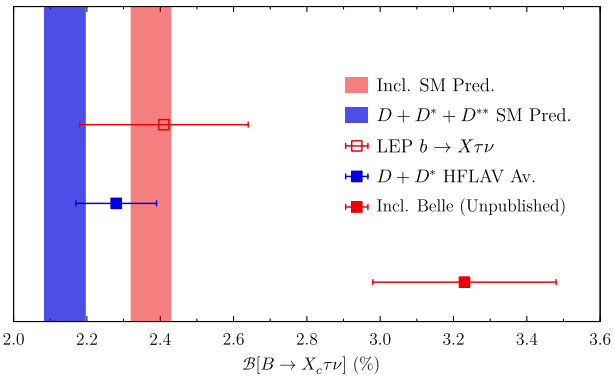


FIG. 27. Saturation of the inclusive SM prediction (red or medium gray band) for $\mathcal{B}(B \to X_c\tau\nu)$ by the sum of the measured exclusive branching fractions that are implied by the $\mathcal{R}(D)$ and $\mathcal{R}(D^{(*)})$ world averages (blue or dark gray square). By comparison, the SM prediction for the sum of the $B \to D^{(*,**)}\tau\nu$ exclusive branching fractions (blue or dark gray band), is compatible with, and does not saturate, the inclusive prediction. Also shown are (i) the measured inclusive branching fraction measurements for $b \to X\tau\nu$ from LEP (Zyla *et al.*, 2020) (open square), which is normalized against the total number of tagged $b\bar{b}$ events. Assuming that the hadronization effects cancel, this can be interpreted as $\mathcal{B}(B \to X\tau\nu)$, and (ii) the unpublished inclusive measurement taken by Hasenbusch (2018) using Belle data (red or medium gray filled square), which shows a large excess.

uncertainties. However, this naive approach may lead to biases in NP interpretations.

The reason for this is that in practice, as discussed in Sec. IV, the $\mathcal{R}(D^{(*)})$ ratios are recovered from fits in multiple reconstructed observables. In these fits, the signal $B \to D^{(*)}\tau\nu$ decay distributions (as well as backgrounds) are assumed to have SM shapes (their reconstructed observables are assumed to have a SM template), while their normalization is allowed to float independently. In the SM, the ratio of $\mathcal{R}(D)$ to $\mathcal{R}(D^*)$ is itself tightly predicted up to small form factor uncertainties. Thus, the current experimental approach can be thought of introducing a *NP fit template* that is parametrized by variation in the double ratio $\mathcal{R}(D)/\mathcal{R}(D^*)$ as well as, say, the overall size of $\mathcal{R}(D^*)$.

Variation of $\mathcal{R}(D^*)$ while keeping $\mathcal{R}(D)/\mathcal{R}(D^*)$ fixed to its SM prediction is consistent with NP contributions from the $c_{VL}$ Wilson coefficient. This Wilson coefficient by definition still generates SM-like distributions, so incorporating $c_{VL}$ contributions is self-consistent with the fit template assumptions from which the measured $\mathcal{R}(D^{(*)})$ values were recovered.

However, to explain the variation in $\mathcal{R}(D)/\mathcal{R}(D^*)$ from the SM prediction requires further NP contributions that generically also alter the $B \to D^{(*)}\tau\nu$ signal (and some background) decay distributions and acceptances. [It is possible that there are NP contributions that modify only the neutrino distributions. Because the experiments marginalize over missing energy, this NP could permit $\mathcal{R}(D)/\mathcal{R}(D^*)$ to simultaneously float from the SM prediction while preserving the SM template for reconstructed observables.] These NP contributions are thus generically inconsistent with the assumed SM template in the current measurement and fit and may affect the recovered values of $\mathcal{R}(D^{(*)})$ themselves. As a result, while the current world average for $\mathcal{R}(D)$–$\mathcal{R}(D^*)$ unambiguously indicates a tension with the SM, it does not *a priori* allow for a self-consistent NP interpretation or explanation. A self-consistent BSM measurement of any recovered observable instead requires dedicated fit templates for each BSM point of interest, which we discuss further in the review.

A similar tension with the SM can be established when additional observables such as asymmetries, longitudinal fractions, and polarization fractions are compared to SM predictions (see Sec. II.D.2), and there is much literature studying their in-principle NP discrimination power. However, the same caveat with regard to NP interpretations applies: NP contributions may alter the recovered values of these parameters.

### 2. Sensitivity and biases in recovered observables

To gain a sense of the size of these effects, we consider an approximate mock-up of an $e^+e^-$ experimental environment and examine the variation in acceptances $\varepsilon$ for $B \to D\tau\nu$ and $B \to (D^* \to D\pi)\tau\nu$, with $\tau \to e\nu\nu$ in the presence of NP. In this mock-up, the beam energies are fixed to 7 and 4 GeV, and we require visible final state particles to fall within an angular acceptance of 20° to 150°. We impose a minimum electron energy threshold of $E_e > 300$ MeV, and an approximate turn-on efficiency is included to account for the slow pion reconstruction efficiencies in $D^* \to D\pi$ decays. We further include a Gaussian smearing added to the truth level $q^2$ with a width of 1.2 GeV$^2$, in order to account for detector resolution and tag-$B$ reconstruction, and require the reconstructed $q^2 > 4$ GeV$^2$.

For this mock-up, we show in Fig. 28 the ratio of the NP experimental acceptance relative to the SM, $\varepsilon/\varepsilon_{\rm SM}$ for several different simplified models; cf. Lees *et al.* (2013), who studied

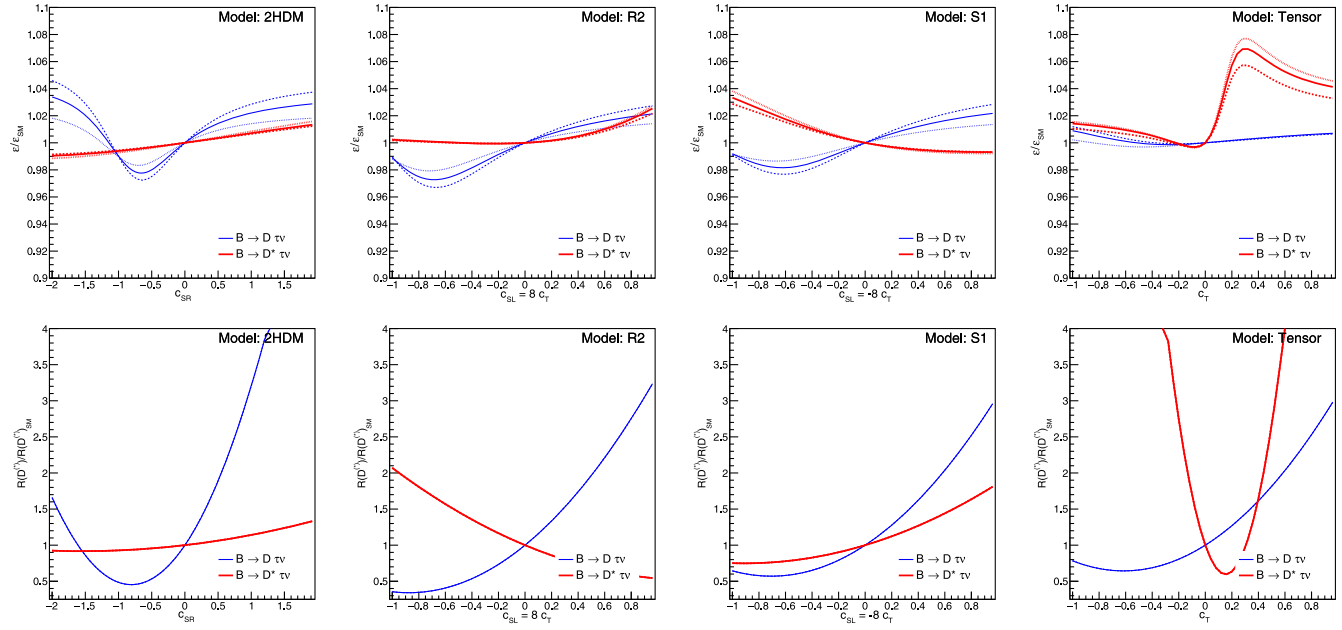


FIG. 28. Top row: typical variation of experimental acceptances for the 2HDM, the leptoquark models $R_2$ and $S_1$, and a pure tensor current, normalized with respect to the SM acceptance $\varepsilon_{\rm SM}$, for $B \to D\tau\nu$ (thin blue lines) and $B \to (D^* \to D\pi)\tau\nu$ (thick red lines), with $\tau \to e\nu\nu$. The dotted, solid, and dashed lines show the resulting acceptances for the $q^2$ resolutions (see text) of 0.8, 1.2, and 1.6 GeV$^2$, respectively. Bottom row: variation in $\mathcal{R}(D^{(*)})/\mathcal{R}(D^{(*)})_{\rm SM}$ for the same models.

this effect for the type-II 2HDM. To characterize the sensitivity to the $q^2$ cut and smearing, we also show acceptances for better and poorer $q^2$ resolutions, with widths of 0.8 and 1.6 GeV$^2$ for the Gaussian smearing, respectively. To provide further insight into the NP variability of the differential distributions, in Fig. 29 we show the percent variation per bin in the reconstructed $m^2_{\rm miss}$ normalized distribution for $\bar{B} \to D\tau\nu$ for the same set of simplified models over the identical range of NP couplings, as well as examples of $\bar{B} \to D^{(*)}\tau\nu$ distributions in the reconstructed $m^2_{\rm miss}$ for particular NP coupling values.

One typically sees a few percent variation in the acceptances as well as in the differential $m^2_{\rm miss}$ distribution, with up to 5% or so variations in some cases. Although this might seem small in comparison to the typical 15%–20% size of currently measured LFUV in $\mathcal{R}(D^{(*)})$, such variations are already comparable to the typical size of systematic uncertainties in current analyses, such as those shown in Table X. It is not surprising then that mismatches between the SM and NP signal templates can introduce significant biases into the analyses. This was observed in the *BABAR* analysis (Lees *et al.*, 2013). A similar but more detailed mock-up analysis in an $e^+e^-$ collider environment suggests biases at greater than the $4\sigma$ level may be expected to typically arise with 5 ab$^{-1}$ of data (Bernlochner *et al.*, 2020a). This effect may also be important in the extraction of the CKM parameter $|V_{cb}|$, which is sensitive to the assumed form factor parametrization used to generate the fit templates.

Future semileptonic analyses may address these biases through a variety of approaches. We discuss these approaches in Sec. VII.B.

### E. Connection to FCNCs

Measurements of the $b \to s\ell\ell$ ratios $R_{K^{(*)}}$ [Eq. (43)] in various ranges of the dilepton invariant mass have produced an indication of lepton flavor universality violation. For instance, the most precise measurements of these ratios in the range $q^2 = m^2(\ell\ell) \in [1.1, 6.0]$ GeV$^2$ currently are (Aaij *et al.*, 2017c, 2021)

$$\mathcal{R}_{K^+} = 0.846^{+0.044}_{-0.041}, \qquad \mathcal{R}_{K^{*0}} = 0.69^{+0.12}_{-0.09} \tag{79}$$

but are expected to be unity to the subpercent level. Angular analyses of $B \to K^*\mu\mu$ decays exhibit components that are in similar tension with theoretical predictions but subject to potentially large theory uncertainties. However, various other less precise measurements of $\mathcal{R}_{K^{(*)}}$ from Belle and *BABAR* are consistent with unity (Amhis *et al.*, 2019); see also the recent $\Lambda_b \to pK\ell\ell$ analysis by LHCb (Aaij *et al.*, 2020c). As discussed in Sec. II.I, because the neutrino belongs to an electroweak doublet, nontrivial model-dependent connections may arise between $b \to c\ell\nu$ and $b \to s\ell\ell$ or $b \to s\nu\nu$ operators. Studies of possible connections between the $\mathcal{R}(D^{(*)})$ and $\mathcal{R}_{K^{(*)}}$ anomalies thus explore common origins of NP in $b \to c\tau\nu$ vs $b \to s\ell\ell$, such as various leptoquark mediators and flavor models, that are not also excluded by other precision measurements; see Sec. II.I. See Calibbi, Crivellin, and Ota (2015), Bhattacharya *et al.* (2015), Buttazzo *et al.* (2017), and Kumar, London, and Watanabe (2019) for some representative works in an extensive literature.

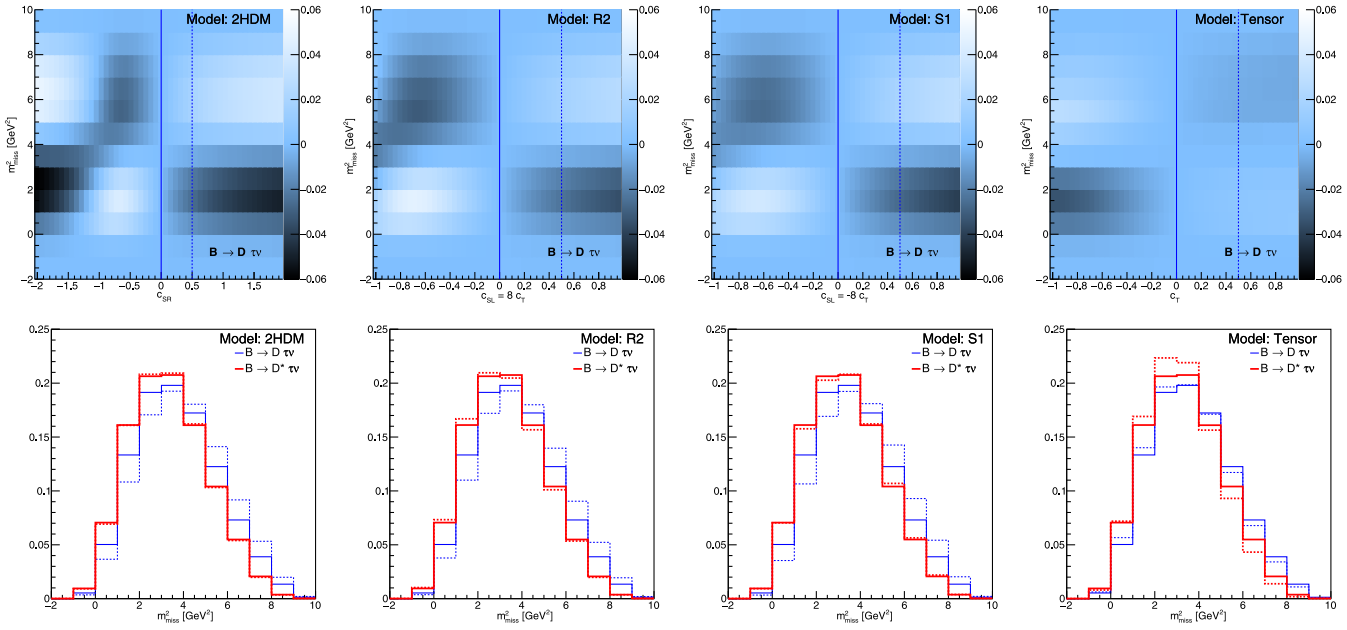


FIG. 29. Top row: color map of the percent variation per bin in the reconstructed $m^2_{\rm miss}$ normalized distribution for $\bar{B} \to D\tau\nu$ comparing the SM to a range of couplings for the 2HDM, the leptoquark models $R_2$ and $S_1$, and a pure tensor current. The variations for $B \to D^*\tau\nu$ are similar but somewhat smaller, ranging up to the 1% to 2% level. Bottom row: examples of normalized $m^2_{\rm miss}$ distributions for the SM (solid lines) vs NP (dashed lines) for $\bar{B} \to D\tau\nu$ (thin blue lines) and $\bar{B} \to D^*\tau\nu$ (thick red lines). The chosen NP coupling for each model is shown as a dashed line in the corresponding top row panel.

In light of these results, it is interesting to consider how much LFUV can be tolerated in the electron versus muon couplings from $b \to c l \nu$ measurements alone. As mentioned earlier, the Belle direct measurement [Eq. (71)] constrains LFUV to no more than percent-level deviations between the electron and muon semileptonic modes.

An additional constraint arises from exclusive measurements of $|V_{cb}|$ and associated $q^2$ distributions from $B \to D^{(*)}\ell\nu$ decays. Although they are not a focus of this review, these measurements are presently quite sensitive to the $B \to D^{(*)}$ form factor parametrization: Precision fits leave little room for the presence of additional form factors beyond those of the $V-A$ interactions because introducing such form factors would significantly distort the well-measured $q^2$ distributions for these decays. Moreover, shape fits to the electron and muon modes separately are in good agreement; see Aubert *et al.* (2009), Glattauer *et al.* (2016), and Waheed *et al.* (2019). These results suggest that in the $b \to ce\nu$ and $b \to c\mu\nu$ systems, one can plausibly introduce NP only via $V-A$ NP currents, and one can plausibly produce electron-muon LFUV at most at the percent level. Based on this qualitative discussion we eagerly anticipate further quantitative studies of bounds on LFUV in $B \to D^{(*)}\ell\nu$.

## VII. PROSPECTS AND OUTLOOK

As detailed in Sec. VI, the world averages for $\mathcal{R}(D)$ and $\mathcal{R}(D^*)$ currently exceed their SM predictions by about 14% each. While the theory uncertainties on the $\mathcal{R}(D^{(*)})$ SM predictions are already 1% to 2% (see Table I), the uncertainties on the corresponding measurements are 5–10 times larger. If key challenges in computation, the modeling of *b*-hadron semileptonic decays, and background estimation are met in the years to come, as discussed in Sec. V, the large amount of data that LHCb and Belle II will collect over the next two decades will bring down the experimental uncertainties to the 1% level. At the present level of discrepancy with the SM, this degree of precision would nominally be sufficient to either establish an observation of LFUV or resolve the present anomalies.

However, highly significant but isolated results will arguably not be sufficient to fully establish the presence of NP in this manner given the vast number of experimental and theoretical effects that can influence the interpretation of these indirect searches for BSM physics. Spurred on by the $\mathcal{R}(D^{(*)})$ anomalies, a wide program of LFUV measurements and calculations that encompasses several experimental and theoretical communities across particle physics will likely be the key to disentangling potential BSM signals from sources of uncertainty that may not be fully understood.

To this end, we discuss here various aspects of this program, including efforts under way to measure other important ratios such as $\mathcal{R}(J/\psi)$, $\mathcal{R}(\pi)$, $\mathcal{R}(D_{(s)}^{(*)})$, and $\mathcal{R}(\Lambda_c)$ (Sec. VII.A); analyses that exploit the fully differential information measured in semitauonic *b*-hadron decays to complement and enhance the sensitivity to NP (Sec. VII.B); and, should these indirect searches end up establishing the presence of NP, the role of proposed future colliders that may be able to either directly observe NP mediators or further characterize established anomalies with related measurements (Sec. VII.C).

### A. Measurement of the ratios $\mathcal{R}(H_{c,u})$

As described throughout this review, the ratios $\mathcal{R}(H_{c,u})$ defined in Eq. (21) are powerful probes of LFUV and NP, in part because of the significant cancellation of theoretical and experimental uncertainties in the ratios. The SM predictions for $\mathcal{R}(D_{(s)}^{(*)})$, $\mathcal{R}(J/\psi)$, and $\mathcal{R}(\Lambda_c)$ now have uncertainties in the 1%–3% range (see Sec. II), and improvements in lattice QCD together with new experimental measurements are expected to bring these down further. Over the next two decades, LHCb and Belle II will collect enough data to reduce the statistical uncertainty on the $\mathcal{R}(H_{c,u})$ measurements down to a few percent or less. However, the systematic uncertainties on the best known ratios $\mathcal{R}(D^{(*)})$ are currently significantly higher than that, as shown in Table XV. Thus, quantifying the achievable precision on $\mathcal{R}(H_{c,u})$ as a probe of NP after LHCb and Belle II complete their data taking rests primarily on estimating the extent to which the associated experimental systematic uncertainties can be reduced.

As detailed in Sec. V, if already ongoing theoretical and experimental efforts are sustained in the following years, the majority of the systematic uncertainty on $\mathcal{R}(H_{c,u})$ is expected to decrease commensurately with the increasing size of the data samples collected. For instance, the uncertainty from the background contributions will decrease as the data control samples grow, and the size of the simulated data samples will continue increasing proportionately if the power of GPUs and fast simulation algorithms is appropriately harnessed. These improvements are likely to have their own limitations, and a certain level of irreducible systematic uncertainty will be reached. Based on the considerations described in Sec. V, one may estimate that floors of ∼1% to 2% uncertainty in $\mathcal{R}(D^{(*)})$ are achievable, while a floor of ∼3% to 4% is plausible for other $\mathcal{R}(H_{c,u})$ ratios, in which the form factor parametrization cannot be measured as precisely. To illustrate the variability of these estimations, we present extrapolations for the anticipated $\mathcal{R}(H_{c,u})$ precision that LHCb and Belle II are likely to reach under two scenarios: (i) a pessimistic scenario, with irreducible systematic uncertainties of 2% for $\mathcal{R}(D^{(*)})$ and 5% for the other $\mathcal{R}(H_{c,u})$ ratios, and (ii) an optimistic scenario, with uncertainty floors of 0.5% for $\mathcal{R}(D^{(*)})$ and 3% for the other $\mathcal{R}(H_{c,u})$ ratios. Further assumptions included in these extrapolations are detailed next.

#### 1. Prospects for $\mathcal{R}(H_{c,u})$ at LHCb

As described in Sec. III, the high center-of-mass energy at the LHC gives LHCb access to large samples of many *b*-hadron species. Thus far, LHCb has published results on $\mathcal{R}(D^*)$ and $\mathcal{R}(J/\psi)$ (see Sec. III.A), and measurements of $\mathcal{R}(D)$, $\mathcal{R}(D^{**})$, $\mathcal{R}(D_s)$, $\mathcal{R}(D_s^*)$, $\mathcal{R}(\Lambda_c)$, and $\mathcal{R}(\Lambda_c^*)$ as well as the nonsemitauonic ratios $\mathcal{R}(D^{(*)})_{\text{light}}$ are under way. We can project the sensitivity to some of these ratios based on the *b*-hadron samples that are expected in the next two decades (Table III), the reduction of the previously

described systematic uncertainty, and the following broad assumptions.[12]

(i) $\mathcal{R}(D^*)$.—The current Run 1 results for $\mathcal{R}(D^{*+})$ have a total uncertainty of 12%, but this value should be reduced by about $\sqrt{2}$ when $\mathcal{R}(D^{*0})$ is also included in the measurement. This can be done by inclusively reconstructing $B^- \to D^{*0}\tau^-\bar{\nu}_\tau$ decays via their feed-down to $D^0\mu^-$ samples in combined $\mathcal{R}(D)$–$\mathcal{R}(D^*)$ measurements. Starting in Run 2, a dedicated trigger achieved 50% higher efficiency and the $b\bar{b}$ cross section increased by a factor of around 2. Another factor of 2 will be gained when the hardware trigger is replaced by a software-only trigger (LHCb Collaboration, 2014) starting in the next data taking period (Run 3).

(ii) $\mathcal{R}(D)$.—The same assumptions apply as for the measurement of $\mathcal{R}(D^*)$ in terms of triggers and the combination of $D^0$ and $D^+$, but data samples are expected to be about 50% smaller due to the difference in branching fractions and $\mathcal{R}(D)$.

(iii) $\mathcal{R}(D^{**})$.—The projections are specifically for $\mathcal{R}(D_1^0)$, which provides the most accessible final state. The projections are based on the expected uncertainty of about 15% for a combined analysis of Run 1 and 2 data and include a factor of 2 efficiency increase starting in Run 3 thanks to the software-only trigger.

(iv) $\mathcal{R}(D_s^{(*)})$: At LHCb, the reconstruction of neutral particles is challenging; see Sec. III.B.2. As a result, the reconstructed number of signal events for $\mathcal{R}(D_s^*)$ is expected to be about 40 times smaller than it is for $\mathcal{R}(D^*)$ due to both the smaller $B_s$ production fraction and the requirement to reconstruct a photon in the $D_s^{*+} \to D_s^+\gamma$ decay (resulting in about a factor of 10 lower efficiency), although these are partially compensated for by the larger reconstructed branching fractions of the $D_s^{*+}$ decay chain. Given the limitations associated with the reconstruction of neutral particles, another possibility is the measurement of $\mathcal{R}(D_s^{[*]}) = [\mathcal{B}(B_s \to D_s\tau\nu) + \mathcal{B}(B_s \to D_s^*\tau\nu)]/[\mathcal{B}(B_s \to D_s\mu\nu) + \mathcal{B}(B_s \to D_s^*\mu\nu)]$, which avoids the explicit reconstruction of the photon. The data samples for this measurement are expected to be about 3 times smaller than those for $\mathcal{R}(D^*)$.

(v) $\mathcal{R}(\Lambda_c)$.—Data samples are expected to be 6 times smaller than for $\mathcal{R}(D^*)$, according to the smaller $\Lambda_b$ production fraction, as well as the requirement to reconstruct an additional track in the $\Lambda_c^+ \to pK^-\pi^+$ decay (which results in a factor of 2 lower efficiency due primarily to the limited LHCb acceptance as well as the PID and tracking efficiencies).

(vi) $\mathcal{R}(\Lambda_c^*)$.—A preliminary study by LHCb (Lupato, 2017) using the muonic decays of the $\tau$ finds a factor of 45 smaller data samples for $\mathcal{R}(\Lambda_c^*(2625))$ than those expected for $\mathcal{R}(D^*)$. This study, however, is not able to constrain the unmeasured $\Lambda_b \to \Lambda_c^* D_s^{(*)}$ background. Instead, we project $\mathcal{R}(\Lambda_c^*(2625))$ based on the same assumptions as for $\mathcal{R}(\Lambda_c)$ but with 33 times smaller data samples due to the smaller $\Lambda_b \to \Lambda_c^* l\nu$ branching fraction and the efficiency of the $\Lambda_c^* \to \Lambda_c\pi\pi$ reconstruction. This is estimated in a preliminary LHCb study of $\Lambda_b \to \Lambda_c^{(*)}\pi\pi\pi$ events under the assumption that the ratio of the $\Lambda_b \to \Lambda_c^{(*)}\pi\pi\pi$ branching fractions is the same as that for $\Lambda_b \to \Lambda_c^{(*)}\tau\nu$. The projections for $\mathcal{R}(\Lambda_c^*(2595))$ would be similar, but with data samples a factor of 2 smaller than those for $\mathcal{R}(\Lambda_c^*(2625))$.

(vii) $\mathcal{R}(J/\psi)$.—We scale the 2018 result based on the expected data samples.

Figure 30 shows the results of these projections. The years on the horizontal axis refer to the dates at which data samples became or will become available, which will eventually result in the plotted total uncertainties once analyses are completed. For instance, the 8.5% uncertainty on $\mathcal{R}(D^*)$ shown at the beginning of 2015 corresponds to the eventual precision achievable for the combined measurement of $\mathcal{R}(D^{*+})$ and $\mathcal{R}(D^{*0})$ with the Run 1 data sample, but the analysis is not expected to be completed until 2021. These projections illustrate the enormous benefit that the data samples collected after the ongoing LHCb Upgrade I will have on the measurement of $\mathcal{R}(H_c)$. The proposed LHCb Upgrade II, which would take place in 2031, would allow LHCb to further improve the precision on these ratios down to the 0.5%–2% level if the irreducible systematic uncertainties can be reduced accordingly.

Finally, $b \to u\tau\nu$ transitions are especially interesting because their potential NP couplings could be quite different from those potentially involved in $b \to c\tau\nu$ transitions. The most direct way to access these transitions at LHCb could be through $B \to p\bar{p}\tau\nu$ decays, for which the normalization $B \to p\bar{p}\ell\nu$ channel was recently observed (Aaij *et al.*, 2020b; Tien *et al.*, 2014) and is quite clean. A measurement of $\mathcal{R}(p\bar{p})$ is currently under way. Additionally, LHCb also has plans to measure $\Lambda_b \to p\tau\nu$, although this process is more challenging due to the lack of a $\Lambda_b$ decay vertex and sizable feed-down backgrounds from $\Lambda_b \to \Lambda_c$ processes.

### 2. Prospects for $\mathcal{R}(H_{c,u})$ at Belle II

Belle II will profit from the much cleaner environment of $B$ meson pair production in electron-positron annihilations; i.e., even with its smaller data samples with respect to LHCb, highly competitive results will emerge. One of the major challenges will be to retain this clean environment at high luminosities and reduce the impact of beam and other backgrounds as much as possible. In addition, several orthogonal datasets can be obtained by leveraging different analysis or tagging approaches; see Sec. III.C.1. The most important results will be as follows:

[12]These projections are for the measurements that employ the muonic decays of the $\tau$ lepton. The projections for the hadronic measurements would be similar except that the irreducible systematic uncertainty would be asymptotically higher because of the external branching fractions used to normalize the result.

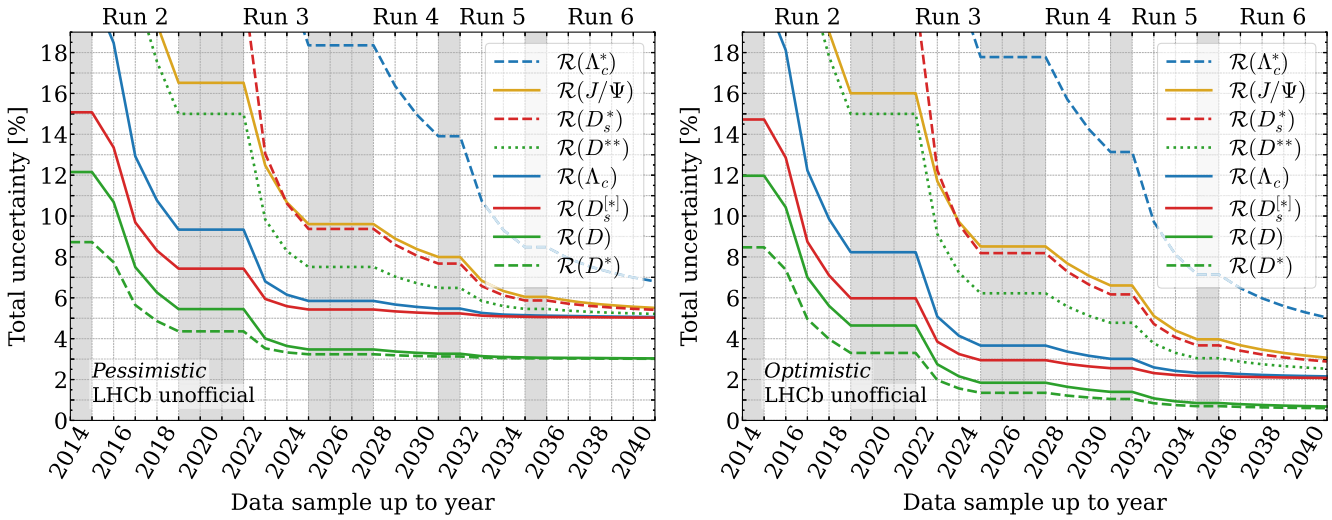


FIG. 30. Projections for the expected precision on the measurement of selected $\mathcal{R}(H_c)$ ratios at LHCb as a function of the year in which the corresponding data sample becomes available. The order of the curves in the legend corresponds to the order of the curves on the plot for the year 2026. Left panel: pessimistic scenario for an irreducible systematic uncertainty of 3% on $\mathcal{R}(D^{(*)})$ and 5% on the other ratios. Right panel: optimistic scenario for an irreducible systematic uncertainty of 0.5% on $\mathcal{R}(D^{(*)})$ and 2% on the other ratios. These extrapolations are based on the current muonic-$\tau$ measurements of $\mathcal{R}(D^{(*)})$ and $\mathcal{R}(J/\psi)$, as well as the forthcoming hadronic-$\tau$ measurement of $\mathcal{R}(D_1^0)$ for the $\mathcal{R}(D^{**})$ curve. The symbol $\mathcal{R}(D_s^{[*]})$ refers to the sum of the $D_s$ and $D_s^*$ yields, as described in the text. The $\mathcal{R}(\Lambda_c^*)$ entry in the legend refers to $\mathcal{R}(\Lambda_c^*(2625))$. The shaded regions correspond to the long shutdowns during which there is no data taking at the LHC and have been updated including the latest estimates (Béjar Alonso *et al.*, 2020).

(i) $\mathcal{R}(D^{(*)})$ *with exclusive tagging*.—In principle, four statistically independent measurements can be carried out this way, namely, either with hadronic or semileptonic tagging and with the focus on either leptonic or hadronic $\tau$ lepton decays. The results with the best control of the systematic uncertainty will be obtained from the combination of hadronic tagging and leptonic or hadronic $\tau$ decays. For these, the $B$ rest frame will be accessible and, in the case of hadronic single-prong $\tau$ decays, the $\tau$ polarization will also be accessible. These results will suffer, however, from the low overall efficiency of hadronic tagging caused by the small branching fractions of such processes.

Semileptonically tagged events will retain much higher numbers of semitauonic decays, but these will in principle suffer from higher systematic uncertainties. Nonetheless, all reconstructed particles in such signatures can still be assigned to either the signal or the tag side, which will allow for reliable measurements. Note that additional energy depositions from beam-background processes will lead to more challenging conditions and backgrounds than those for the present-day results. Further, only measurements with leptonic $\tau$ decays have been realized to date, so it will be an exciting challenge for Belle II to establish measurements with hadronic $\tau$ decays using this technique.

(ii) $\mathcal{R}(D^{(*)})$ *with inclusive or semi-inclusive tagging*.—Compared to hadronic or semileptonic tagging, inclusive tagging offers much higher reconstruction efficiency at the cost of higher backgrounds and lower precision in the reconstruction of $B$-frame kinematic variables. Nonetheless, such measurements will offer additional orthogonal datasets that can be analyzed. A particularly interesting option might involve the use of semi-inclusive tagging via a charmed seed meson ($D$, $D^*$, $J/\psi$, $D_s$, or $D_s^*$). Such an approach could offer more experimental control than purely inclusive tagging while still retaining a high reconstruction efficiency. It is unclear at present how precise such measurements will be, as no detailed studies have been carried out, and we therefore do not include these in our projections.

(iii) $\mathcal{R}(\pi/\rho/\omega)$.—Belle II will have a unique opportunity to further investigate semitauonic processes involving $b \to u$ transitions. The existing search (detailed in Sec. IV.A.2) focused on charged pion final states. Interesting additional channels with higher branching fractions are decays to $\rho$ and $\omega$ mesons, although the large width of the $\rho$ meson is a challenge. Nonetheless, Belle II will improve on the existing limits and, with a substantial dataset of 10–15 $\text{ab}^{-1}$, the discovery of these decays, assuming that their branching fraction is of the size of the SM expectation, is feasible.

(iv) $\mathcal{R}(D_s^{(*)})$.—Belle II anticipates collecting a clean sample of $e^+e^- \to \Upsilon(5S) \to B_s^{(*)}\bar{B}_s^{(*)}$ events. The experimental methodology applied to the study of semitauonic $B$ meson decays can also be applied to these datasets. For instance, future measurements of $\mathcal{R}(D_s^{(*)})$ based on hadronic or semileptonic tagging can be done in a fashion similar to the $\mathcal{R}(D^{(*)})$

measurements. It is unclear, however, whether a precision can be reached that would rival LHCb, because of the much smaller number of produced $B_s$ mesons.

(v) $\mathcal{R}(X_{(c)})$ *with hadronic tagging*.—Belle II will further be able to produce measurements of fully inclusive or semi-inclusive semitauonic final states. These will allow measurements of $\mathcal{R}(X_{(c)})$. We use the preliminary measurement of Hasenbusch (2018) to estimate the sensitivity for $\mathcal{R}(X)$ but caution the reader that Belle II will need to demonstrate the feasibility of such measurements.

Figure 31 displays the expected sensitivity as a function over time. The left panel displays our pessimistic scenario based on the statistical and systematic uncertainties of existing measurements and an irreducible systematic uncertainty of 3%, as previously described. The right panel shows the same progression for the optimistic scenario, which includes an irreducible systematic uncertainty of 0.5% and an increase in the efficiency of the exclusive tagging algorithms of 50%. Such an improvement is not completely unexpected since novel ideas, such as the use of deep learning concepts and attention maps, have already shown promising efficiency gains in simulated events (Tsaklidis, 2020). However, it remains to be seen whether such efficiency gains are also retained in the analysis of actual collision events, and also whether the identified events are clean enough to provide an actual gain in sensitivity. In both scenarios the uncertainties are expected to decrease with luminosity until the systematic uncertainty floor is reached.

The gray bands in Fig. 31 indicate years in which significant downtime is expected due to upgrades of the detector and/or the accelerator. In 2022, the Belle II pixel detector will be replaced with its final version, and more radiation-hard photomultipliers for the time-of-propagation detector will be integrated as well. In 2026, the Belle II interaction region will be upgraded to allow for the increase of the instantaneous luminosity to its design value: The superconducting magnets that perform the final focusing will be placed farther away from the beam crossing point to reduce the chance of quenches. Measurements of $\mathcal{R}(D^*)$ will be somewhat more precise because of their cleaner signature and lack of feed-down contributions compared to $\mathcal{R}(D)$ measurements, but in both cases a precision of 4% to 5% and about 3% will be reached by 2026 in the pessimistic and optimistic scenarios, respectively. Inclusive $\mathcal{R}(D^{(*)})$ measurements and measurements of $\mathcal{R}(D^*)$ with hadronic $\tau$ final states will reach 3.5% precision in the pessimistic scenario and below 2% in the optimistic case. All measurements, except for the ones explicitly probing $b \to u$ transitions, will reach precisions close to their irreducible systematic uncertainties by 2031.

### B. Exploiting full differential information

#### 1. Angular analyses and recovered observables

A 2% to 3% systematic floor for LFUV ratio measurements might be reached quickly given the high statistical power provided by the LHCb and Belle II experiments together. Combined with the fact that the ratios $\mathcal{R}(H_{c,u})$ are recovered observables from template fits to differential distributions, this suggests that attention might increasingly turn toward other measurable properties. These include angular correlations, longitudinal and polarization fractions of the $D^*$ and $\tau$ (see Sec. II.D.2), and asymmetries, etc.

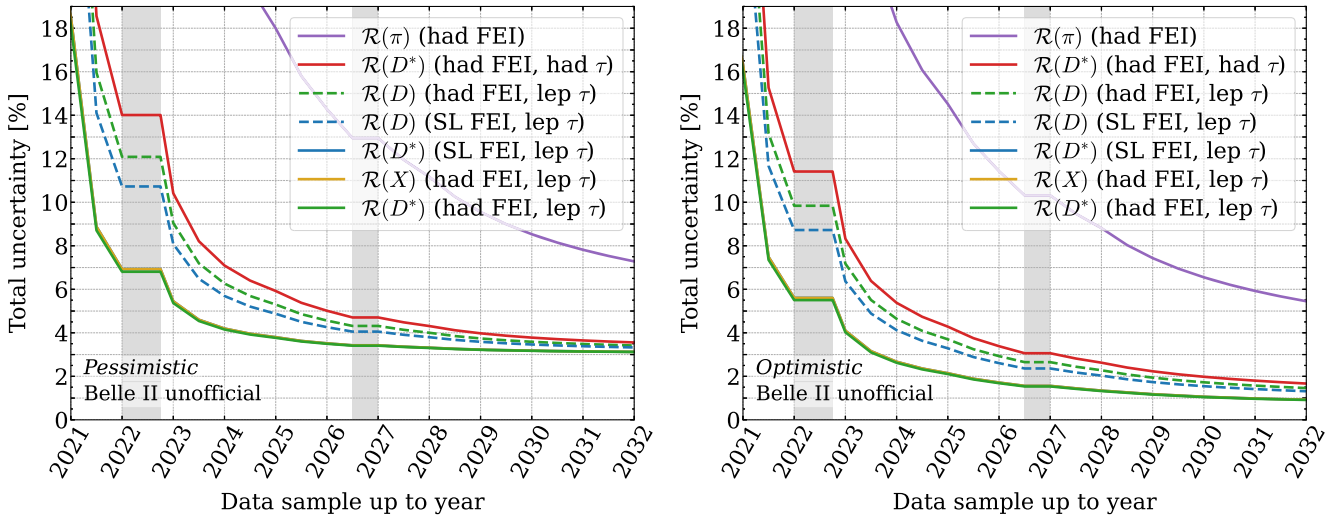


FIG. 31. Projections for the expected precision on the measurements of $\mathcal{R}(D^{(*)})$, $\mathcal{R}(X)$, and $\mathcal{R}(\pi)$ at Belle II as a function of the year in which the corresponding data sample will become available. The order of the curves in the legend corresponds to the order of the curves on the plot for the year 2022. The "$\mathcal{R}(D^{(*)})$ (SL FEI, lep $\tau$)" curve sits under the "$\mathcal{R}(X)$ (had FEI, lep $\tau$)" curve because their projected uncertainties are extremely similar. An irreducible systematic uncertainty of (left panel) 3% for the pessimistic scenario and (right panel) 0.5% for the optimistic one is assumed. The optimistic scenario also assumes a 50% increase in the reconstruction efficiency of the exclusive tagging algorithms. The shaded regions indicate years in which significant downtime is expected due to upgrades of the detector and/or the accelerator.

Many such observables using angular correlations have been put forward in a wide range of phenomenological studies, in particular, as a means to distinguish SM from NP interactions in $b \to c\tau\nu$ transitions. On the experimental side, the most accessible of these is the $D^*$ longitudinal fraction $F_{L,\tau}(D^*)$, which can easily be reconstructed. As discussed in Sec. IV.D.2, Belle has already provided a preliminary measurement for this variable based on $B \to D^*\tau\nu$ decays. This result is compatible with the SM expectations within $2\sigma$. LHCb is expected to soon publish a similar analysis with slightly improved sensitivity.

The $\tau$ polarization (Sec. IV.D.1) was also measured for the first time by Belle, which used the $\tau \to \pi\nu$ single-prong decay channel, although with limited precision. Preliminary studies in LHCb have demonstrated that the measurement of the $\tau$ polarization is possible using the $\tau \to \pi^-\pi^+\pi^-\nu$ decay mode, recycling techniques developed at LEP involving optimized variables (Davier *et al.*, 1993). This analysis is much more complex than the single-prong mode, in which the pion momentum in the $\tau$ rest frame acts as an in-principle perfect polarizer because the analyzing power of the $\pi\pi\pi$ final state is comparatively small [see Eq. (28)]: The analyzing power of the dominant $a_1$ resonance in $\tau \to \pi^-\pi^+\pi^-\nu$ features a numerical cancellation on shell, $\alpha_{a_1} = (1 - 2m_{a_1}^2/m_\tau^2)/(1 + 2m_{a_1}^2/m_\tau^2) \simeq 0.02$. The expected LHCb sensitivity to $P_\tau(D^{(*)})$ in the three-prong mode is not yet known.

A recent study (Hill *et al.*, 2019) showed that LHCb may be able to reliably recover the angular coefficients describing the $B \to (D^* \to D\pi)(\tau \to h\nu)\nu$ decay, assuming a sample size of around $10^5$ signal events. A dataset of this size is expected to be available at the end of Run 3 of the LHC; first attempts along these lines may be performed using the full Run 2 dataset.

### 2. Future strategies

However, as discussed in Sec. VI.D.2, mismatches between SM and NP signal templates can introduce significant biases into analyses that consider recovered observables, such that one cannot consistently determine the compatibility of the data with any particular NP model. Future semileptonic analyses may address these biases through a variety of approaches: One possibility is to attempt to carefully control the size of these biases when experiments quote their results. A different, more robust, approach is for experiments to adapt their analyses such that, instead of reporting recovered observables, they perform fits directly in the multidimensional space of the NP couplings, the Wilson coefficients, themselves. This approach has the additional advantage of making it more straightforward to combine results from different experiments.

The latter approach is sometimes referred to as forward folding. A key obstacle is that generating sufficient simulated data for the SM analysis alone is challenging (see Sec. V.A); generating enough data to study a space of NP models is naively computationally prohibitive. This difficulty can be resolved, however, with matrix element reweighting, which allows for large MC samples to be converted from the SM to any desired NP template, or to any description of the hadronic matrix elements, without regenerating the underlying MC data. In recent years, new software tools such as the HAMMER library (Bernlochner *et al.*, 2020b) have been developed by experimental-theory collaborations to permit fast and efficient MC reweighting of this type.

As an example, consider the mock-up reweighting analysis of Bernlochner *et al.* (2020a), which uses the differential information in the missing invariant mass $m_{\text{miss}}^2$ and lepton momentum $|\boldsymbol{p}_\ell|$, including an approximation of the effects of various backgrounds and reconstruction effects. In Fig. 32 we show the potential recovered C.L.'s from this analysis for the complex NP Wilson coefficients of the $R_2$ simplified model, defined by $c_{SL} \simeq 8c_T$, compared to the "truth" value $c_{SL}(= 8c_T) = 0.25(1 + i)$. This mock-up forecasts that, with $5\,\text{ab}^{-1}$ of future data, one would be able to not only exclude the SM but also recover the "true" NP Wilson coefficient up to a mild twofold degeneracy in its imaginary part. Because the forward-folding approach can use all differential information by construction, it may supersede approaches based on measuring recovered observables.

## C. Outlook for future colliders

If NP were to be discovered through indirect LFUV searches, future colliders could be instrumental in further characterizing the nature of the new interactions. In some scenarios, NP mediators can escape the discovery reach of the HL-LHC while still giving rise to the observation of LFUV in semitauonic *b*-hadron decays. Future hadron machines such as the FCC-*hh* collider (Abada *et al.*, 2019b), which is presently under study at CERN, would extend the reach for direct observation of NP mediators into the multi-TeV range covering most of these scenarios. An indirect NP observation could also be possible at FCC-*hh* by detecting deviations from the predicted inclusive $\tau\tau$ production rate in the SM (Abada *et al.*, 2019b).

High-luminosity $e^+e^-$ colliders may also play a crucial role because the characteristics of *b*-hadron production on the $Z$ pole combine several of the advantages enjoyed by *B*-factory experiments with those of hadron colliders. In particular, the advantages of the former include a very favorable ratio of $B$ production divided by total cross section

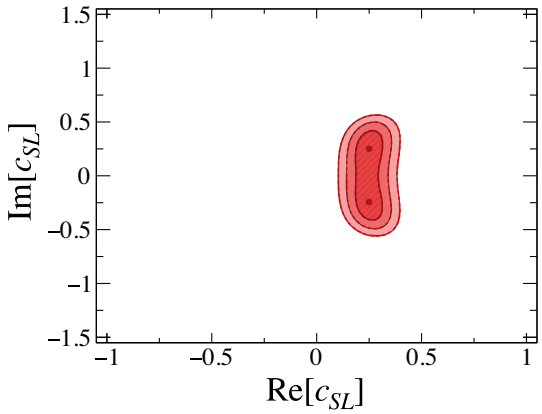


FIG. 32. The 68%, 95%, and 99% C.L. allowed regions for the $R_2$ simplified model coupling $c_{SL} = 8c_T$ fitting to an Asimov dataset with $c_{SL} = 8c_T = 0.25(1 + i)$. The best fit recovered points are shown as gray dots.

(22%), a low-multiplicity environment (perfect separation of the two $B$ mesons), and good knowledge of the $B$ center-of-mass frame achieved by exploiting jet direction measurements and the peaked fragmentation function. The advantages of the latter include the large production of all $b$-hadron species and the large boost of the hadrons themselves, which allows one to more easily separate their decay products from primary fragments, and to fully reconstruct secondary and tertiary vertices.

The "TeraZ" class of proposed $e^+e^-$ colliders, either FCC-$ee$ (Abada *et al.*, 2019a) or CEPC (Dong *et al.*, 2018a, 2018b), could provide enough $B$ mesons produced in this very favorable $Z$-pole environment to measure very complex decays such as $B^+ \to K^+\tau^+\tau^-$ that are very difficult to probe otherwise (Kamenik *et al.*, 2017). A precise measurement of this branching ratio and its angular distributions would provide a critical test of LFUV in the neutral-current decays involving the $\tau$ lepton. This might in turn provide evidence of a link between the LFUV hints from $\mathcal{R}(H_{c,u})$, which involves charged-current decays to $\tau$ leptons, and those of $\mathcal{R}_{K^{(*)}}$, which involve neutral-current decays to the first two lepton families only; see Sec. II.I. In a similar vein, rare $B_c$ decays such as $B_c \to \tau\nu$ could also be studied at a TeraZ factory (Zheng *et al.*, 2020). A precision of 1% of this branching fraction could be reached, thereby providing strong constraints on many NP models.

### D. Parting thoughts

In this review we provided an in-depth look into the theoretical and experimental foundations for semitauonic LFUV measurements. This comprised a detailed overview of the theoretical state of the art and an extensive survey of the experimental environments and measurement methodologies at the $B$ factories and LHCb. We further reexamined the current combinations and NP interpretations of the data as well as their limitations, and the future prospects to control systematic uncertainties, all of which will be crucial not only for establishing a tension with the SM, should one exist, but also for understanding the nature of the new physics responsible for it.

Driven by the intriguing and persistent anomalies in $\mathcal{R}(D^{(*)})$, the host of planned and ongoing measurements of lepton flavor universality violation in semitauonic $b$-hadron decays will provide new data-driven insights into, if not resolutions for, these current LFUV puzzles. A golden era in flavor physics is just ahead of us.

## ACKNOWLEDGMENTS

We thank Hassan Jawahery and Zoltan Ligeti for their comments on the manuscript. We also are grateful to Maria Różańska for her input on the Belle measurements of $R(D^{(*)})$ and to Marcello Rotondo for his expertise on the LHCb projections for $\mathcal{R}(H_u)$, the $B_s \to D_s^{**}$ contributions, and other matters. We thank Ana Ovcharova for her help with the formatting of several plots. We thank Patrick Owen for sharing his work on the LHCb projections for $\mathcal{R}(H_c)$ and subsequent discussions. We thank CERN for its hospitality during the initial preparation of this work. F. U. B. is supported by DFG Emmy Noether Grant No. BE 6075/1-1 and BMBF Grant No. 05H19PDKB1. M. F. S. is supported by the National Science Foundation under Contract No. PHY-2012793. D. J. R. is supported in part by the Office of High Energy Physics of the U.S. Department of Energy under Contract No. DE-AC02-05CH11231.

## REFERENCES

Aad, Georges, *et al.* (ATLAS), 2020, "Test of the universality of $\tau$ and $\mu$ lepton couplings in $W$-boson decays from $t\bar{t}$ events with the ATLAS detector," arXiv:2007.14040.

Aaij, Roel, *et al.* (LHCb Collaboration), 2011, "Measurements of the branching fractions for $B_{(s)} \to D_{(s)}\pi\pi\pi$ and $\Lambda_b^0 \to \Lambda_c^+\pi\pi\pi$," Phys. Rev. D **84**, 092001; **85**, 039904(E) (2012).

Aaij, Roel, *et al.* (LHCb Collaboration), 2015a, "LHCb detector performance," Int. J. Mod. Phys. A **30**, 1530022.

Aaij, Roel, *et al.* (LHCb Collaboration), 2015b, "Measurement of $b_c^+$ Production in Proton-Proton Collisions at $\sqrt{s} = 8$ TeV," Phys. Rev. Lett. **114**, 132001.

Aaij, Roel, *et al.* (LHCb Collaboration), 2015c, "Measurement of the Ratio of Branching Fractions $\mathcal{B}(\bar{B}^0 \to D^{*+}\tau^-\bar{\nu}_\tau)/\mathcal{B}(\bar{B}^0 \to D^{*+}\mu^-\bar{\nu}_\mu)$," Phys. Rev. Lett. **115**, 111803; **115**, 159901(E) (2015).

Aaij, Roel, *et al.* (LHCb Collaboration), 2017a, "Measurement of the $b$-Quark Production Cross Section in 7 and 13 TeV $pp$ Collisions," Phys. Rev. Lett. **118**, 052002.

Aaij, Roel, *et al.* (LHCb Collaboration), 2017b, "Expression of interest for a phase-II LHCb upgrade: Opportunities in flavour physics, and beyond, in the HL-LHC era," CERN Technical Report No. CERN-LHCC-2017-003.

Aaij, Roel, *et al.* (LHCb Collaboration), **2017**c, "Test of lepton universality with $B^0 \to K^{*0}\ell^+\ell^-$ decays," J. High Energy Phys. 08, 055.

Aaij, Roel, *et al.* (LHCb Collaboration), 2018a, "Measurement of the Ratio of Branching Fractions $\mathcal{B}(B_c^+ \to J/\psi\tau^+\nu_\tau)/\mathcal{B}(B_c^+ \to J/\psi\mu^+\nu_\mu)$," Phys. Rev. Lett. **120**, 121801.

Aaij, Roel, *et al.* (LHCb Collaboration), 2018b, "Test of lepton flavor universality by the measurement of the $B^0 \to D^{*-}\tau^+\nu_\tau$ branching fraction using three-prong $\tau$ decays," Phys. Rev. D **97**, 072013.

Aaij, Roel, *et al.* (LHCb Collaboration), 2019a, "Measurement of $b$ hadron fractions in 13 TeV $pp$ collisions," Phys. Rev. D **100**, 031102(R).

Aaij, Roel, *et al.* (LHCb Collaboration), 2019b, "Measurement of the relative $B^- \to D^0/D^{*0}/D^{**0}\mu^-\bar{\nu}_\mu$ branching fractions using $B^-$ mesons from $\bar{B}_{s2}^{*0}$ decays," Phys. Rev. D **99**, 092009.

Aaij, Roel, *et al.* (LHCb Collaboration), 2019c, "Search for Lepton-Universality Violation in $B^+ \to K^+\ell^+\ell^-$ Decays," Phys. Rev. Lett. **122**, 191801.

Aaij, Roel, *et al.* (LHCb Collaboration), 2020a, "Determination of quantum numbers for several excited charmed mesons observed in $B^- \to D^{*+}\pi^-\pi^-$ decays," Phys. Rev. D **101**, 032005.

Aaij, Roel, *et al.* (LHCb Collaboration), **2020**b, "Observation of the semileptonic decay $B^+ \to p\bar{p}\mu^+\nu_\mu$," J. High Energy Phys. 03, 146.

Aaij, Roel, *et al.* (LHCb Collaboration), 2020c, "Test of lepton universality with $\Lambda_b^0 \to pK^-\ell^+\ell^-$ decays," J. High Energy Phys. 05, 040.

Aaij, Roel, *et al.* (LHCb Collaboration), 2021, "Test of lepton universality in beauty-quark decays," arXiv:2103.11769.

Abada, A., *et al.*, 2019a, "FCC-ee: The lepton collider," Eur. Phys. J. Special Topics **228**, 261–623.

Abada, A., *et al.* (FCC Collaboration), 2019b, "FCC physics opportunities: Future Circular Collider Conceptual Design Report Volume 1," Eur. Phys. J. C **79**, 474.

Abashian, A., *et al.*, 2002, "The Belle detector," Nucl. Instrum. Methods Phys. Res., Sect. A **479**, 117–232.

Abbiendi, G., *et al.* (OPAL Collaboration), 2001, "Measurement of the branching ratio for the process $b \to \tau^- \bar{\nu}_\tau X$," Phys. Lett. B **520**, 1–10.

Abdesselam, A., *et al.* (Belle Collaboration), 2017, "Precise determination of the CKM matrix element $|V_{cb}|$ with $\bar{B}^0 \to D^{*+} \ell^- \bar{\nu}_\ell$ decays with hadronic tagging at Belle," arXiv:1702.01521.

Abdesselam, A., *et al.* (Belle Collaboration), 2019, "Measurement of the $D^{*-}$ polarization in the decay $B^0 \to D^{*-} \tau^+ \nu_\tau$," arXiv:1903.03102.

Abe, T., *et al.* (Belle II Collaboration), 2010, "Belle II technical design report," arXiv:1011.0352.

Ablikim, M., *et al.* (BESIII Collaboration), 2010, "Design and construction of the BESIII detector," Nucl. Instrum. Methods Phys. Res., Sect. A **614**, 345–399.

Abreu, P., *et al.* (DELPHI Collaboration), 2000, "Upper limit for the decay $B^- \to \tau^- \bar{\nu}_\tau$ and measurement of the $b \to \tau \bar{\nu}_\tau X$ branching ratio," Phys. Lett. B **496**, 43–58.

Abudinén, F., *et al.* (Belle II Collaboration), 2020, "A calibration of the Belle II hadronic tag-side reconstruction algorithm with $B \to X \ell \nu$ decays," arXiv:2008.06096.

Acciarri, M., *et al.* (L3 Collaboration), 1994, "Measurement of the inclusive $b \to \tau \nu X$ branching ratio," Phys. Lett. B **332**, 201–208.

Acciarri, M., *et al.* (L3 Collaboration), 1996, "Measurement of the branching ratios $b \to e\nu X, \mu\nu X, \tau_\nu X$ and $\nu X$," Z. Phys. C **71**, 379–390.

Adachi, I., *et al.* (Belle Collaboration), 2009, "Measurement of $B \to D^{(*)} \tau \nu$ using full reconstruction tags," arXiv:0910.4301.

Akai, Kazunori, Kazuro Furukawa, and Haruyo Koiso (SuperKEKB Collaboration), 2018, "SuperKEKB collider," Nucl. Instrum. Methods Phys. Res., Sect. A **907**, 188–199.

Akeroyd, A. G., and Chuan-Hung Chen, 2017, "Constraint on the branching ratio of $B_c \to \tau \bar{\nu}$ from LEP1 and consequences for $R(D^{(*)})$ anomaly," Phys. Rev. D **96**, 075011.

Albrecht, Johannes, *et al.*, 2019, "Luminosity scenarios for LHCb Upgrade II, CERN Technical Reports No. LHCb-PUB-2019-001 and No. CERN-LHCb-PUB-2019-001.

Alok, Ashutosh Kumar, Dinesh Kumar, Suman Kumbhakar, and S. Uma Sankar, 2017, "$D^*$ polarization as a probe to discriminate new physics in $\bar{B} \to D^* \tau \bar{\nu}$," Phys. Rev. D **95**, 115038.

Alonso, Rodrigo, Benjamín Grinstein, and Jorge Martin Camalich, 2017, "Lifetime of $B_c^-$ Constrains Explanations for Anomalies in $B \to D^{(*)} \tau \nu$," Phys. Rev. Lett. **118**, 081802.

Altmannshofer, W., *et al.* (Belle II Collaboration), 2019, "The Belle II physics book," Prog. Theor. Exp. Phys. **2019**, 123C01; **2020**, 029201(E) (2020).

Altmannshofer, Wolfgang, P. S. Bhupal Dev, and Amarjit Soni, 2017, "$R_{D^{(*)}}$ anomaly: A possible hint for natural supersymmetry with $R$-parity violation," Phys. Rev. D **96**, 095010.

Amhis, Yasmine Sara, *et al.* (HFLAV Collaboration), 2019, "Averages of $b$-hadron, $c$-hadron, and $\tau$-lepton properties as of 2018," updated results and plots available at https://hflav.web.cern.ch/.

Aoki, S., *et al.* (Flavour Lattice Averaging Group), 2020, "FLAG review 2019," Eur. Phys. J. C **80**, 113.

Aubert, B., *et al.* (*BABAR* Collaboration), 2008, "Observation of the Semileptonic Decays $B \to D^* \tau^- \bar{\nu}_\tau$ and Evidence for $B \to D \tau^- \bar{\nu}_\tau$," Phys. Rev. Lett. **100**, 021801.

Aubert, B., *et al.* (*BABAR* Collaboration), 2013, "The *BABAR* detector: Upgrades, operation and performance," Nucl. Instrum. Methods Phys. Res., Sect. A **729**, 615–701.

Aubert, Bernard, *et al.* (*BABAR* Collaboration), 2009, "Measurements of the semileptonic decays $\bar{B} \to D \ell \bar{\nu}_\ell$ and $\bar{B} \to D^* \ell \bar{\nu}_\ell$ using a global fit to $DX\ell\bar{\nu}_\ell$ final states," Phys. Rev. D **79**, 012002.

Augusto Alves, Jr., A., *et al.* (LHCb Collaboration), 2008, "The LHCb detector at the LHC," J. Instrum. **3**, S08005.

Bailas, G., S. Hashimoto, T. Kaneko, and J. Koponen (JLQCD Collaboration), **2020**, "Study of intermediate states in the inclusive semi-leptonic $B \to X_c \ell \nu$ decay structure functions," Proc. Sci. LATTICE2019, 148 [arXiv:2001.11678].

Bailey, Jon A., *et al.* (Fermilab Lattice and MILC Collaborations), 2015a, "$B \to \pi \ell \ell$ Form Factors for New-Physics Searches from Lattice QCD," Phys. Rev. Lett. **115**, 152002.

Bailey, Jon A., *et al.* (Fermilab Lattice and MILC Collaborations), 2015b, "$|V_{ub}|$ from $B \to \pi \ell \nu$ decays and $(2+1)$-flavor lattice QCD," Phys. Rev. D **92**, 014024.

Balk, S., J. G. Korner, and D. Pirjol, 1998, "Inclusive semileptonic decays of polarized $\Lambda_b$ baryons into polarized $\tau$-leptons," Eur. Phys. J. C **1**, 221–233.

Barate, R., *et al.* (ALEPH Collaboration), 2001, "Measurements of $\mathcal{B}(b \to \tau \bar{\nu}_\tau X)$ and $\mathcal{B}(b \to \tau \bar{\nu}_\tau D^{*+} X)$ and upper limits on $\mathcal{B}(b \to \tau \bar{\nu}_\tau)$ and $\mathcal{B}(b \to s\nu\bar{\nu})$," Eur. Phys. J. C **19**, 213–227.

Barberio, Elisabetta, and Zbigniew Was, 1994, "PHOTOS—A universal Monte Carlo for QED radiative corrections: Version 2.0," Comput. Phys. Commun. **79**, 291–308.

Bardhan, Debjyoti, and Diptimoy Ghosh, 2019, "$B$ -meson charged current anomalies: The post-Moriond 2019 status," Phys. Rev. D **100**, 011701.

Bazavov, A., *et al.* (Fermilab Lattice and MILC Collaborations), 2021, "Semileptonic form factors for $B \to D^* \ell \nu$ at nonzero recoil from $2+1$–flavor lattice QCD," arXiv:2105.14019.

Bediaga, I., *et al.* (LHCb Collaboration), 2012, "Framework TDR for the LHCb upgrade: Technical design report," Reports No. CERN-LHCC-2012-007 and No. LHCb-TDR-12.

Béjar Alonso, I., O. Brüning, P. Fessia, M. Lamont, L. Rossi, L. Tavian, and M. Zerlauth, 2020, Eds., *High-Luminosity Large Hadron Collider (HL-LHC): Technical Design Report*, CERN Yellow Reports: Monographs Vol. 10 (CERN, Geneva).

Bernlochner, Florian U., Zoltan Ligeti, Dean J. Robinson, and William L. Sutcliffe, 2018, "New Predictions for $\Lambda_b \to \Lambda_c$ Semileptonic Decays and Tests of Heavy Quark Symmetry," Phys. Rev. Lett. **121**, 202001.

Bernlochner, Florian U., 2015, "$B \to \pi \tau \bar{\nu}_\tau$ decay in the context of type II 2HDM," Phys. Rev. D **92**, 115019.

Bernlochner, Florian U., Stephan Duell, Zoltan Ligeti, Michele Papucci, and Dean J. Robinson, 2020a, "Das ist der HAMMER: Consistent new physics interpretations of semileptonic decays," arXiv:2002.00020.

Bernlochner, Florian U., Stephan Duell, Zoltan Ligeti, Michele Papucci, and Dean J. Robinson, 2020b, computer code HAMMER—Helicity Amplitude Module for Matrix Element Reweighting, https://zenodo.org/record/3993770#.YTkUX1VKiUk.

Bernlochner, Florian U., and Zoltan Ligeti, 2017, "Semileptonic $B_{(s)}$ decays to excited charmed mesons with $e$, $\mu$, $\tau$ and searching for new physics with $R(D^{**})$," Phys. Rev. D **95**, 014022.

Bernlochner, Florian U., Zoltan Ligeti, Michele Papucci, and Dean J. Robinson, 2017, "Combined analysis of semileptonic $B$ decays to $D$ and $D^*$: $R(D^{(*)})$, $|V_{cb}|$, and new physics," Phys. Rev. D **95**, 115008; **97**, 059902(E) (2018).

Bernlochner, Florian U., Zoltan Ligeti, and Dean J. Robinson, 2018, "Model-independent analysis of semileptonic $B$ decays to $D^{**}$ for arbitrary new physics," Phys. Rev. D **97**, 075011.

Bernlochner, Florian U., Markus T. Prim, and Dean J. Robinson, 2021, "$B \to \rho l \bar{\nu}$ and $\omega l \bar{\nu}$ in and beyond the standard model: Improved predictions and $|V_{ub}|$," arXiv:2104.05739.

Bevan, A. J., *et al.*, 2014, "The physics of the $b$ factories," Eur. Phys. J. C **74**, 3026.

Bharucha, Aoife, David M. Straub, and Roman Zwicky, **2016**, "$B \to V \ell^+ \ell^-$ in the standard model from light-cone sum rules," J. High Energy Phys. 08, 098.

Bhattacharya, Bhubanjyoti, Alakabha Datta, David London, and Shanmuka Shivashankara, 2015, "Simultaneous explanation of the $R_K$ and $R(D^{(*)})$ puzzles," Phys. Lett. B **742**, 370–374.

Biancofiore, Pietro, Pietro Colangelo, and Fulvia De Fazio, 2013, "On the anomalous enhancement observed in $B \to D^{(*)} \tau \bar{\nu}_\tau$ decays," Phys. Rev. D **87**, 074010.

Bifani, Simone, Sébastien Descotes-Genon, Antonio Romero Vidal, and Marie-Hélène Schune, 2019, "Review of lepton universality tests in $B$ decays," J. Phys. G **46**, 023001.

Bigi, Dante, and Paolo Gambino, 2016, "Revisiting $B \to D \ell \nu$," Phys. Rev. D **94**, 094008.

Bigi, Dante, Paolo Gambino, and Stefan Schacht, **2017**, "$R(D^*)$, $|V_{cb}|$, and the heavy quark symmetry relations between form factors," J. High Energy Phys. 11, 061.

Biswas, Sandip, and Kirill Melnikov, 2010, "Second order QCD corrections to inclusive semileptonic $B \to X_c \ell \bar{\nu}_\ell$ decays with massless and massive lepton," J. High Energy Phys. 02, 089.

Boeckh, Tobias, 2020, "$B$-tagging with deep neural networks," master's thesis (Karlsruhe Institute of Technology).

Böer, Philipp, Marzia Bordone, Elena Graverini, Patrick Owen, Marcello Rotondo, and Danny Van Dyk, 2018, "Testing lepton flavour universality in semileptonic $\Lambda_b \to \Lambda_c^*$ decays," J. High Energy Phys. 06, 155.

Bordone, Marzia, Nico Gubernari, Martin Jung, and Danny van Dyk, 2020, "Heavy-quark expansion for $\bar{B}_s \to D_s^{(*)}$ form factors and unitarity bounds beyond the $SU(3)_F$ limit," Eur. Phys. J. C **80**, 347.

Bordone, Marzia, Martin Jung, and Danny van Dyk, 2020, "Theory determination of $\bar{B} \to D^{(*)} \ell^- \bar{\nu}$ form factors at $\mathcal{O}(1/m_c^2)$," Eur. Phys. J. C **80**, 74.

Bourrely, Claude, Irinel Caprini, and Laurent Lellouch, 2009, "Model-independent description of $B \to \pi \ell \bar{\nu}_\ell$ decays and a determination of $|V_{ub}|$," Phys. Rev. D **79**, 013008.

Boyd, C. Glenn, Benjamin Grinstein, and Richard F. Lebed, 1996, "Model independent determinations of $\bar{B} \to D^* \ell \bar{\nu}_\ell$ form factors," Nucl. Phys. **B461**, 493–511.

Boyd, C. Glenn, Benjamin Grinstein, and Richard F. Lebed, 1997, "Precision corrections to dispersive bounds on form factors," Phys. Rev. D **56**, 6895–6911.

Bozek, A., *et al.* (Belle Collaboration), 2010, "Observation of $B^+ \to \bar{D}^{*0} \tau^+ \nu_\tau$ and evidence for $B^+ \to \bar{D}^0 \tau^+ \nu_\tau$ at Belle," Phys. Rev. D **82**, 072005.

Buttazzo, Dario, Admir Greljo, Gino Isidori, and David Marzocca, **2017**, "$B$-physics anomalies: A guide to combined explanations," J. High Energy Phys. 11, 044.

Calí, Stefano, Suzanne Klaver, Marcello Rotondo, and Barbara Sciascia, 2019, "Impacts of radiative corrections on measurements of lepton flavour universality in $B \to D \ell \nu_\ell$ decays," Eur. Phys. J. C **79**, 744.

Calibbi, Lorenzo, Andreas Crivellin, and Toshihiko Ota, 2015, "Effective Field Theory Approach to $b \to s \ell \ell^{(\prime)}$, $B \to K^{(*)} \nu \bar{\nu}$ and $B \to D^{(*)} \tau \nu$ with Third Generation Couplings," Phys. Rev. Lett. **115**, 181801.

Caprini, Irinel, Laurent Lellouch, and Matthias Neubert, 1998, "Dispersive bounds on the shape of $\bar{B} \to D^{(*)} \ell \bar{\nu}$ form factors," Nucl. Phys. **B530**, 153–181.

Caria, G., *et al.* (Belle Collaboration), 2020, "Measurement of $\mathcal{R}(D)$ and $\mathcal{R}(D^*)$ with a Semileptonic Tagging Method," Phys. Rev. Lett. **124**, 161803.

Caria, Giacomo, 2019, "Measurement of $R(D)$ and $R(D^*)$ with a semileptonic tag at the Belle experiment," Ph.D. thesis (University of Melbourne).

Cerri, A., *et al.*, 2019, "Report from Working Group 4: Opportunities in Flavour Physics at the HL-LHC and HE-LHC," CERN Report No. CERN-LPCC-2018-06.

Choudhury, S., *et al.* (BELLE Collaboration), **2021**, "Test of lepton flavor universality and search for lepton flavor violation in $B \to K \ell \ell$ decays," J. High Energy Phys. 03, 105.

Ciezarek, Gregory, Manuel Franco Sevilla, Brian Hamilton, Robert Kowalewski, Thomas Kuhr, Vera Lüth, and Yutaro Sato, 2017, "A challenge to lepton universality in $B$ meson decays," Nature (London) **546**, 227–233.

Cohen, Thomas D., Henry Lamm, and Richard F. Lebed, 2019, "Precision model-independent bounds from global analysis of $b \to c \ell \nu$ form factors," Phys. Rev. D **100**, 094503.

Colangelo, Pietro, Fulvia De Fazio, and Francesco Loparco, **2020**, "Inclusive semileptonic $\Lambda_b$ decays in the standard model and beyond," J. High Energy Phys. 11, 032.

Colquhoun, B., C. T. H. Davies, R. J. Dowdall, J. Kettle, J. Koponen, G. P. Lepage, and A. T. Lytle (HPQCD Collaboration), 2015, "$B$-meson decay constants: A more complete picture from full lattice QCD," Phys. Rev. D **91**, 114509.

Colquhoun, Brian, Christine Davies, Jonna Koponen, Andrew Lytle, and Craig McNeile (HPQCD Collaboration), **2016**, "$B_c$ decays from highly improved staggered quarks and NRQCD," Proc. Sci. LATTICE2016, 281 [arXiv:1611.01987].

Cowan, Glen, 2019, "Statistical models with uncertain error parameters," Eur. Phys. J. C **79**, 133.

Davier, M., L. Duflot, F. Le Diberder, and A. Rouge, 1993, "The optimal method for the measurement of tau polarization," Phys. Lett. B **306**, 411–417.

de Boer, Stefan, Teppei Kitahara, and Ivan Nisandzic, 2018, "Soft-Photon Corrections to $\bar{B} \to D \tau^- \bar{\nu}_\tau$ Relative to $\bar{B} \to D \mu^- \bar{\nu}_\mu$," Phys. Rev. Lett. **120**, 261804.

de Favereau, J., C. Delaere, P. Demin, A. Giammanco, V. Lemaître, A. Mertens, and M. Selvaggi (DELPHES 3 Collaboration), **2014**, "DELPHES 3: A modular framework for fast simulation of a generic collider experiment," J. High Energy Phys. 02, 057.

Detmold, William, Christoph Lehner, and Stefan Meinel, 2015, "$\Lambda_b \to p \ell^- \bar{\nu}_\ell$ and $\Lambda_b \to \Lambda_c \ell^- \bar{\nu}_\ell$ form factors from lattice QCD with relativistic heavy quarks," Phys. Rev. D **92**, 034503.

Dong, Mingyi, *et al.* (CEPC Study Group), 2018a, "CEPC Conceptual Design Report: Volume 1—Accelerator," arXiv:1809.00285.

Dong, Mingyi, *et al.* (CEPC Study Group), 2018b, "CEPC Conceptual Design Report: Volume 2—Physics & detector," arXiv:1811.10545.

Ecker, G., J. Gasser, H. Leutwyler, A. Pich, and E. de Rafael, 1989, "Chiral Lagrangians for massive spin 1 fields," Phys. Lett. B **223**, 425–432.

Ecker, G., J. Gasser, A. Pich, and E. de Rafael, 1989, "The role of resonances in chiral perturbation theory," Nucl. Phys. **B321**, 311–342.

Eichten, Estia, and Brian Russell Hill, 1990, "An effective field theory for the calculation of matrix elements involving heavy quarks," Phys. Lett. B **234**, 511–516.

Erdmann, Martin, Jonas Glombitza, and Thorben Quast, 2019, "Precise simulation of electromagnetic calorimeter showers using

a Wasserstein generative adversarial network," Comput. Software Big Sci. **3**, 4.

Fajfer, S., J. F. Kamenik, and I. Nisandzic, 2012, "On the $B \to D^* \tau \bar{\nu}_\tau$ sensitivity to new physics," Phys. Rev. D **85**, 094025.

Feindt, M., F. Keller, M. Kreps, T. Kuhr, S. Neubauer, D. Zander, and A. Zupanc, 2011, "A hierarchical NeuroBayes-based algorithm for full reconstruction of $B$ mesons at $B$ factories," Nucl. Instrum. Methods Phys. Res., Sect. A **654**, 432–440.

Franco Sevilla, Manuel, 2012, "Evidence for an excess of $B \to D^{(*)} \tau \nu$ decays," Ph.D. thesis (Stanford University).

Freytsis, M., Z. Ligeti, and J. T. Ruderman, 2015, "Flavor models for $\bar{B} \to D^{(*)} \tau \bar{\nu}$," Phys. Rev. D **92**, 054018.

Gambino, Paolo, Martin Jung, and Stefan Schacht, 2019, "The $V_{cb}$ puzzle: An update," Phys. Lett. B **795**, 386–390.

Georgi, Howard, 1990, "An effective field theory for heavy quarks at low energies," Phys. Lett. B **240**, 447–450.

Glattauer, R., *et al.* (Belle Collaboration), 2016, "Measurement of the decay $B \to D \ell \nu_\ell$ in fully reconstructed events and determination of the Cabibbo-Kobayashi-Maskawa matrix element $|V_{cb}|$," Phys. Rev. D **93**, 032006.

González-Alonso, Martín, Jorge Martin Camalich, and Kin Mimouni, 2017, "Renormalization-group evolution of new physics contributions to (semi)leptonic meson decays," Phys. Lett. B **772**, 777–785.

Greljo, Admir, Jorge Martin Camalich, and José David Ruiz-Álvarez, 2019, "Mono-$\tau$ Signatures at the LHC Constrain Explanations of $B$-Decay Anomalies," Phys. Rev. Lett. **122**, 131803.

Greljo, Admir, and David Marzocca, 2017, "High-$p_T$ dilepton tails and flavor physics," Eur. Phys. J. C **77**, 548.

Hamer, P., *et al.* (Belle Collaboration), 2016, "Search for $B^0 \to \pi^- \tau^+ \nu_\tau$ with hadronic tagging at Belle," Phys. Rev. D **93**, 032007.

Harrison, Judd, and Christine T. H. Davies (HPQCD Collaboration), 2021, "$B_s \to D_s^*$ form factors for the full $q^2$ range from lattice QCD," arXiv:2105.11433.

Harrison, Judd, Christine T. H. Davies, and Andrew Lytle, 2020a, "$B_c \to J/\psi$ Form factors for the full $q^2$ range from lattice QCD," arXiv:2007.06957.

Harrison, Judd, Christine T. H. Davies, and Andrew Lytle (HPQCD Collaboration), 2020b, "$R(J/\psi)$ and $B_c^- \to J/\psi \ell^- \bar{\nu}_\ell$ lepton flavor universality violating observables from lattice QCD," arXiv:2007.06956.

Hasenbusch, Jan, 2018, "Analysis of inclusive semileptonic $b$ meson decays with $\tau$ lepton final states at the Belle experiment," Ph.D. thesis (University of Bonn).

Herb, S. W., *et al.*, 1977, "Observation of a Dimuon Resonance at 9.5 GeV in 400-GeV Proton-Nucleus Collisions," Phys. Rev. Lett. **39**, 252–255.

Hill, Donal, Malcolm John, Wenqi Ke, and Anton Poluektov, **2019**, "Model-independent method for measuring the angular coefficients of $B^0 \to D^* \tau \nu$ decays," J. High Energy Phys. 11, 133.

Hirose, S., *et al.* (Belle Collaboration), 2017, "Measurement of the $\tau$ Lepton Polarization and $R(D^*)$ in the Decay $\bar{B} \to D^* \tau^- \bar{\nu}_\tau$," Phys. Rev. Lett. **118**, 211801.

Hirose, S., *et al.* (Belle Collaboration), 2018, "Measurement of the $\tau$ lepton polarization and $R(D^*)$ in the decay $\bar{B} \to D^* \tau^- \bar{\nu}_\tau$ with one-prong hadronic $\tau$ decays at Belle," Phys. Rev. D **97**, 012004.

Huang, Zhuo-Ran, Ying Li, Cai-Dian Lu, M. Ali Paracha, and Chao Wang, 2018, "Footprints of new physics in $b \to c \tau \nu$ transitions," Phys. Rev. D **98**, 095018.

Huschle, M., *et al.* (Belle Collaboration), 2015, "Measurement of the branching ratio of $\bar{B} \to D^{(*)} \tau^- \bar{\nu}_\tau$ relative to $\bar{B} \to D^{(*)} \ell^- \bar{\nu}_\ell$ decays with hadronic tagging at Belle," Phys. Rev. D **92**, 072014.

Huschle, Matthias, 2015, "Measurement of the branching ratio of $B \to D^{(*)} \tau \nu_\tau$ relative to $B \to D^{(*)} \ell \nu_\ell$ decays with hadronic tagging at Belle," Ph.D. thesis (Karlsruhe Institute of Technology).

Isgur, Nathan, Daryl Scora, Benjamin Grinstein, and Mark B. Wise, 1989a, "Semileptonic $b$ and $d$ decays in the quark model," Phys. Rev. D **39**, 799–818.

Isgur, Nathan, Daryl Scora, Benjamin Grinstein, and Mark B. Wise, 1989b, "Semileptonic $B$ and $D$ decays in the quark model," Phys. Rev. D **39**, 799–818.

Isgur, Nathan, and Mark B. Wise, 1989, "Weak decays of heavy mesons in the static quark approximation," Phys. Lett. B **232**, 113–117.

Isgur, Nathan, and Mark B. Wise, 1990, "Weak transition form factors between heavy mesons," Phys. Lett. B **237**, 527–530.

Ivanov, Mikhail A., Jürgen G. Körner, and Pietro Santorelli, 2006, "Exclusive semileptonic and nonleptonic decays of the $B_c$ meson," Phys. Rev. D **73**, 054024.

Jaiswal, Sneha, Soumitra Nandi, and Sunando Kumar Patra, **2017**, "Extraction of $|V_{cb}|$ from $B \to D^{(*)} \ell \nu_\ell$ and the standard model predictions of $R(D^{(*)})$," J. High Energy Phys. 12, 060.

Jaiswal, Sneha, Soumitra Nandi, and Sunando Kumar Patra, 2020, "Updates on SM predictions of $|V_{cb}|$ and $R(D^*)$ in $B \to D^* \ell \nu_\ell$ decays," arXiv:2002.05726.

Jenkins, Elizabeth Ellen, Michael E. Luke, Aneesh V. Manohar, and Martin J. Savage, 1993, "Semileptonic $B_c$ decay and heavy quark spin symmetry," Nucl. Phys. **B390**, 463–473.

Jung, Martin, and David M. Straub, **2019**, "Constraining new physics in $b \to c \ell \nu$ transitions," J. High Energy Phys. 01, 009.

Kahn, James, 2019, "Hadronic tag sensitivity study of $b \to k^{(*)} \nu \bar{\nu}$ and selective background Monte Carlo simulation at Belle II," Ph.D. thesis (Ludwig-Maximilians-Universität München).

Kamenik, J. F., S. Monteil, A. Semkiv, and L. Vale Silva, 2017, "Lepton polarization asymmetries in rare semi-tauonic $b \to s$ exclusive decays at FCC-$ee$," Eur. Phys. J. C **77**, 701.

Keck, T., *et al.*, 2019, "The full event interpretation," Comput. Software Big Sci. **3**, 6.

Keck, Thomas, 2017, "Machine learning algorithms for the Belle II experiment and their validation on Belle data," Ph.D. thesis (Karlsruhe Institute of Technology).

Klaver, Suzanne, 2019, "Impacts of radiative corrections on measurements of lepton flavour universality in $B \to D \ell \nu_\ell$ decays," arXiv:1907.01618.

Kumar, Jacky, David London, and Ryoutaro Watanabe, 2019, "Combined explanations of the $b \to s \mu^+ \mu^-$ and $b \to c \tau^- \bar{\nu}$ anomalies: A general model analysis," Phys. Rev. D **99**, 015007.

Lees, J. P., *et al.* (*BABAR* Collaboration), 2012, "Evidence for an Excess of $\bar{B} \to D^{(*)} \tau^- \bar{\nu}_\tau$ Decays," Phys. Rev. Lett. **109**, 101802.

Lees, J. P., *et al.* (*BABAR* Collaboration), 2013, "Measurement of an excess of $\bar{B} \to D^{(*)} \tau^- \bar{\nu}_\tau$ decays and implications for charged Higgs bosons," Phys. Rev. D **88**, 072012.

Leibovich, Adam K., Zoltan Ligeti, Iain W. Stewart, and Mark B. Wise, 1997, "Predictions for $B \to D_1(2420) \ell \bar{\nu}$ and $B \to D_2^*(2460) \ell \bar{\nu}$ at Order $\Lambda_{\rm QCD}/m_{c,b}$," Phys. Rev. Lett. **78**, 3995–3998.

Leibovich, Adam K., Zoltan Ligeti, Iain W. Stewart, and Mark B. Wise, 1998, "Semileptonic $B$ decays to excited charmed mesons," Phys. Rev. D **57**, 308–330.

Leibovich, Adam K., and Iain W. Stewart, 1998, "Semileptonic $\Lambda_b$ decay to excited $\Lambda_c$ baryons at order $\Lambda_{\rm QCD}/m_Q$," Phys. Rev. D **57**, 5620–5631.

Leljak, Domagoj, and Blazenka Melic, **2020**, "$|V_{ub}|$ determination and testing of lepton flavour universality in semileptonic $B_c \to D^{(*)}$ decays," J. High Energy Phys. 02, 171.

LHCb Collaboration, 2014, "LHCb trigger and online upgrade technical design report," Reports No. CERN-LHCC-2014-016 and No. LHCB-TDR-016.

LHCb Collaboration, 2020, "Amplitude analysis of $B^+ \to D^{*-}\pi^+ D_s^+$" (to be published).

Li, Xin-Qiang, Ya-Dong Yang, and Xin Zhang, 2016, "Revisiting the one leptoquark solution to the R($D^{(*)}$) anomalies and its phenomenological implications," J. High Energy Phys. 08, 054.

Ligeti, Zoltan, Yosef Nir, and Matthias Neubert, 1994, "Subleading Isgur-Wise form factor $\xi(v \cdot v')$ and its implications for the decays $\bar{B} \to D^* \ell \bar{\nu}_\ell$," Phys. Rev. D **49**, 1302–1309.

Ligeti, Zoltan, and Frank J. Tackmann, 2014, "Precise predictions for $B \to X_c \tau \bar{\nu}$ decay distributions," Phys. Rev. D **90**, 034021.

Lupato, Anna, 2017, "Study of semitauonic and semimuonic $\Lambda_b^0 \to \Lambda_c^{*+} l^- \bar{\nu}_l$ decays at LHCb," Ph.D. thesis (Università degli Studi di Padova).

Matyja, A., *et al.* (Belle Collaboration), 2007, "Observation of $B^0 \to D* \tau^+ \nu_\tau$ Decay at Belle," Phys. Rev. Lett. **99**, 191807.

McLean, E., C. T. H. Davies, J. Koponen, and A. T. Lytle, 2020, "$B_s \to D_s \ell \nu$ form factors for the full $q^2$ range from lattice QCD with nonperturbatively normalized currents," Phys. Rev. D **101**, 074513.

McLean, E., C. T. H. Davies, A. T. Lytle, and J. Koponen, 2019, "Lattice QCD form factor for $B_s \to D_s^* l \nu$ at zero recoil with nonperturbative current renormalization," Phys. Rev. D **99**, 114512.

Müller, D., M. Clemencic, G. Corti, and M. Gersabeck, 2018, "ReDecay: A novel approach to speed up the simulation at LHCb," Eur. Phys. J. C **78**, 1009.

Neubert, Matthias, 1994, "Heavy quark symmetry," Phys. Rep. **245**, 259–396.

Neubert, Matthias, Zoltan Ligeti, and Yosef Nir, 1993a, "QCD sum rule analysis of the subleading Isgur-Wise form factor $\chi_2(v \cdot v')$," Phys. Lett. B **301**, 101–107.

Neubert, Matthias, Zoltan Ligeti, and Yosef Nir, 1993b, "Subleading Isgur-Wise form factor $\chi_3(v \cdot v')$ to order $\alpha_s$ in QCD sum rules," Phys. Rev. D **47**, 5060–5066.

Nugent, I. M., T. Przedziński, P. Roig, O. Shekhovtsova, and Z. Waş, 2013, "Resonance chiral Lagrangian currents and experimental data for $\tau^- \to \pi^- \pi^- \pi^+ \nu_\tau$," Phys. Rev. D **88**, 093012.

Penalva, N., E. Hernández, and J. Nieves, 2020, "$\bar{B}_c \to \eta_c$, $\bar{B}_c \to J/\psi$ and $\bar{B} \to D^{(*)}$ semileptonic decays including new physics," arXiv:2007.12590.

Pervin, Muslema, Winston Roberts, and Simon Capstick, 2005, "Semileptonic decays of heavy Λ baryons in a quark model," Phys. Rev. C **72**, 035201.

Sakaki, Y., A. Tanaka, M. Tayduganov, and R. Watanabe, 2013, "Testing leptoquark models in $\bar{B} \to D^{(*)} \tau \bar{\nu}$," Phys. Rev. D **88**, 094012.

Sato, Y., *et al.* (Belle Collaboration), 2016, "Measurement of the branching ratio of $\bar{B}^0 \to D^{*+} \tau^- \bar{\nu}_\tau$ relative to $\bar{B}^0 \to D^{*+} \ell^- \bar{\nu}_\ell$ decays with semileptonic tagging," Phys. Rev. D **94**, 072007.

Scora, Daryl, and Nathan Isgur, 1995, "Semileptonic meson decays in the quark model: An update," Phys. Rev. D **52**, 2783–2812.

Shekhovtsova, O., T. Przedzinski, P. Roig, and Z. Was, 2012, "Resonance chiral Lagrangian currents and $\tau$ decay Monte Carlo," Phys. Rev. D **86**, 113008.

Sirlin, A., 1982, "Large $m_W$, $m_Z$ behaviour of the $O_\alpha$ corrections to semileptonic processes mediated by W," Nucl. Phys. **B196**, 83–92.

Sjöstrand, Torbjörn, Stefan Ask, Jesper R. Christiansen, Richard Corke, Nishita Desai, Philip Ilten, Stephen Mrenna, Stefan Prestel, Christine O. Rasmussen, and Peter Z. Skands, 2015, "An introduction to PYTHIA 8.2," Comput. Phys. Commun. **191**, 159–177.

Tanaka, Minoru, and Ryoutaro Watanabe, 2013, "New physics in the weak interaction of $\bar{B} \to D^{(*)} \tau \bar{\nu}$," Phys. Rev. D **87**, 034028.

Tien, K. J., *et al.* (Belle Collaboration), 2014, "Evidence for semileptonic $B^- \to p \bar{p} l^- \bar{\nu}_l$ decays," Phys. Rev. D **89**, 011101.

Tsaklidis, Ilias, 2020, "Demonstrating learned particle decay reconstruction using graph neural networks at Belle II," master's thesis (Universitè de Strasbourg).

Vallecorsa, S., 2018, "Generative models for fast simulation," J. Phys. Conf. Ser. **1085**, 022005.

Waheed, E., *et al.* (Belle Collaboration), 2019, "Measurement of the CKM matrix element $|V_{cb}|$ from $B^0 \to D^{*-} \ell^+ \nu_\ell$ at Belle," Phys. Rev. D **100**, 052007.

Wirbel, M., B. Stech, and Manfred Bauer, 1985, "Exclusive semileptonic decays of heavy mesons," Z. Phys. C **29**, 637.

Zheng, Taifan, Ji Xu, Lu Cao, Dan Yu, Wei Wang, Soeren Prell, Yeuk-Kwan E. Cheung, and Manqi Ruan, 2020, "Analysis of $B_c \to \tau \nu_\tau$ at CEPC," arXiv:2007.08234.

Zyla, P. A., *et al.* (Particle Data Group), 2020, "Review of particle physics," Prog. Theor. Exp. Phys. **2020**, 083C01.